**Title**

Micro-to-meso scale approaches for deformable soft robots and sensing capabilities in biomedical microdevices

**Author**

Tilvawala, Gopesh

**Publication Date**

2021

UNIVERSITY OF CALIFORNIA SAN DIEGO

# Micro-to-meso scale approaches for deformable soft robots and sensing capabilities in biomedical microdevices

A dissertation submitted in partial satisfaction of the
requirements for the degree
Doctor of Philosophy

in

Engineering Sciences (Mechanical Engineering)

by

Gopesh Tilvawala

Committee in charge:

Professor James Friend, Chair
Professor Alexander Khalessi
Professor Tania Morimoto
Professor Alexander Norbash
Professor Lonnie Petersen

2021

The dissertation of Gopesh Tilvawala is approved, and it is acceptable in quality and form for publication on microfilm and electronically.

University of California San Diego

2021

# DEDICATION

To my parents Manaswini and Chaitanyakumar, my sisters Forum and Deepal, for supporting my education and career goals even when I had to move two continents and perservere through several set-backs.

# EPIGRAPH

Think big,

Think fast,

Think ahead,

Ideas are no one's monopoly.

—Dhirubhai Ambani.

# TABLE OF CONTENTS

# LIST OF FIGURES

# LIST OF TABLES

# ACKNOWLEDGEMENTS

Forgive me for the length of this section but my journey to obtaining a PhD spans more than 8 long years of graduate school in Australia and the US, not intentionally, but circumstantially. Furthermore, growing up in in Nakuru, once a small town in Kenya, pursuing a PhD in engineering was beyond my imagination, and I have a lot of people to thank for the journey that brought me here.

### *SME 320, La Jolla*

Not due to formality but out of genuine gratitude, I would like to thank my advisor James Friend for his guidance and support that has enabled the completion of this thesis. In the summer of 2014 after over 300 rejections from industry and academia, when very few people were willing to hire me, James recruited me and gave me a chance to pursue research. Over the past 7 years, he not only provided me with research related support but also more importantly gave mentorship to help me develop as a person, and gain meaningful perspectives on other aspects of life without losing sight of the bigger picture. Whenever I lost hope, he gave unwavering confidence. James provided me with skills to perform research both independently and in collaboration with others, and for lack of a better word has been dangerously creative in exploring new ideas. I intentionally use the word “dangerously" in this context because the originality of his ideas and ability to think creatively can be so exciting that even the most daunting problems seem feasible. While no amount of words would do justice, very few would be brave to write this, and even fewer would mean it, but if I had to do my PhD again, I would do it with the same advisor, so thank you for everything!

I would like to express my deepest appreciation to my committee and clinical advisors Alexander Norbash and Alexander Khalessi for always being there to provide unconditional research support and suggestions throughout my PhD. Despite their busy schedules, they are

among the quickest to respond, and generous with their time to ensure we overcome any hurdles that arise. Without their support and directions none of the steerable catheter work would be realized. I will forever be grateful to them for giving me the opportunity to shadow procedures in the angiography suites, provide directions to conduct animal trials and above all for being very supportive mentors. The opportunity to shadow procedures had a profound impact not only on my understanding of the medical devices used but also increased my motivation for pursuing medical device research by an order of magnitude. To my clinical advisor in Melbourne, Bernard Yan, thanks for dedicating your time, through frequent zoom calls and multiple visits to San Diego. Despite being thousands of miles away from us, your time and efforts not only helped expedite progress of my research but also provided deep technical insights into catheter dynamics and clinical problems.

I am also thankful to David Santiago-Dieppa for generously giving his time during countless after-hours meetings, testing devices, and providing advise on how to strategically make progress on the research front. If not for the testing and feedback conducted after-hours and weekends, multiple phone calls, iterative development and progress of the device would not have been possible. When I arrived in San Diego, I had a lot of motivation and drive to explore new research areas. Through the first two years I thought I was productive with my time until I met Jessica Wen thorugh the BlueLINC program at UCSD. To Jess, thank you for helping with testing and validation of the catheter, assisting with countless proposals, prepare amazing presentations on short notice, your selfless dedication of time on weekends to conduct testing, and for teaching me vascular anatomy. Your kind efforts expedited progress of my degree, helped me increase productivity, and you are an inspiration, so thank you! David and Jessica, you were my main partners in conducting the testing and validation for the steerable catheter, and no amount of appreciation would be enough for all the heavy lifting you helped with.

For the intraocular pressure measurement project I was very fortunate to work with Robert Weinreb and Andrew Camp from the Shiley eye center at UCSD. I am grateful to both of them for giving me the opportunity to explore additional research areas for medical devices. Their dedication to research and ability to leverage engineering capabilities to solve a medical problem are inspiring. This was one of the quickest concept to successful completion of animal trials and would not have been possible without their generous dedication of time for the research projects depite the burden of intense clinical duties.

I have had amazing lab mates in the medically advanced devices lab (MADLab), whether it is because James is good at selecting students or it is by way of good fortune, I could not have asked for a better experience. Thanks for all the time we spent together, from intense discussions and brain storming sessions on new fabrication methods and research ideas, to exploring San Diego, throwing axes, its been a pleasure and certainly very memorable. Special thanks to An Huang and Edward Aminov, particularly for making the first two years in San Diego more adventurous and fun. Many thanks to my fellow lab members Shuai Zhang, Jiyang Mei, Naiqing Zhang, William Connacher, Jiaying Wang, Aditya Vasan, Amihai Horesh, and Jeremy Orosco. I also had great pleasure working with our visiting members, Yuta Kurashina and Chikahiro Imashiro, it was truly fun working with you in the lab and hearing the interesting stories about Japan. I'd like to acknowledge Michael Unanian for not only helping crack a challenging circuit development problem but also helping me see some of the practical perspectives on life. I must also thank my friends in SME, Brato Chakrabarti, Ernesto Criado-Hidalgo, Lorenzo Rossini, Andrew Bright, Achal Mahajan, Debashish Das, Arijit Mahapatra, and Grace Luo, for the fun conversations and lighting up the long days.

I would also like to thank Todd Coleman and Amr Zoul Omar, for helping expand research areas beyond my vision and gain some valuable skills during the early days. Even though we worked together briefly, I enjoyed working with you and hope that one day in the future we will have to opportunity to work on a cross-collaborative project again.

While most conventional research projects require limited direct interaction with industry, none of the projects presented here would be possible without generous support from friends in Industry. Special thanks to Scott Van Voorhis from David-Schnurr Associates, for relentless efforts in getting polymer tubing, balloons, braiding wires among many other accessories even on short notice to expedite the testing and development of the steerable catheter. I would like to extend my sincere thanks to Irina Roof, Arnold Evangelista, and Mike Herr at ZEUS for their guidance and support to obtain radio-opaque tubing and understand reflow procedures for assembling catheters. Thanks to Caroline Liberti at microlumen for assistance with obtaining small order quantities of polyimide tubing and technical advise for bonding elastomers and plastics, the latter was a far more difficult challenge than anticipated. Despite an almost infinite number of 3D printing services available out there, the complexities of 3D printing the vasculature models are challenging to handle, special thanks to Griffin Harrison and his team at Automaticmfg.com for being so patient and providing all the 3D prints needed with intricate details.

Life at UCSD would not have been smooth without the support of the administrative staff at UCSD. Linda McKamey, Devaney Kerr, Marina Robenko, and Lawrence Berman, this goes out to you. It is rare to get administrative staff who go well out of their way to make our lives easier, so big thanks to Lusia Veksler for all the help and support, whether it was booking last minute conference travels or expediting orders during the COVD-19 pandemic, you have been a reliable pillar and you are awesome!

*RIMAC weightroom, La Jolla*

During all the years in San Diego, barring for the COVID-19 pandemic, regularly working out at RIMAC early in the morning was perhaps the single most important activity that kept me going through the most challenging times. Thanks to the “morning crew": Isiah

Aceves, Chaz Lichenstern, Milton Ramirez, Nathan De Marco, Matt Levesque, Tiffany Tran, Alan Bui, Luis Cortez, Defne Sevil, Martin Magno, Peter Weigel, William Graham, Monica Acosta, Sebastian Troncoso, Mariana Marquez, Nikhil Khare, Akhil Patel, Amar Gupta, Josh Nichols, Jason Kim, Ana Bucknum, MJ, Kaz Fujita and anyone else I've forgotten. It was the morning workouts that usually kick started my day. Interactions with people outside the engineering bubble was a great place of learning for me, and always made me look forward to waking up every morning.

### *IGE*

During my second year, I was fortunate to receive a fellowship from the institute of the global entrepreneur to pursue the technology management certificate. I'm especially thankful to Prof. Vish Krishnan, Ricardo dos Santos, and Kimberley Davis-King for their captivating lectures when pursuing the technology management certificate, and all the mentorship and support provided post-completion. My sincere thanks to initial classmates and now friends Jonas Kurniawan, Jordan Furlong, and Ana Moreno for making the discussions lively, preparing pitches, and sharing interesting business ideas.

### *COVID-19, Melbourne-San Diego*

In March 2020, while I was visiting Melbourne (Australia) for the first time since moving to San Diego, the COVID pandemic escalated exponentially and flights were getting curtailed. In fear of losing valuable research time, I managed to catch the last flight out of Melbourne to Los Angeles. However, upon reaching San Diego, it was inevitable that non-essential research activities would be put on hold. I was fortunate to get the opportunity to lead the projects on developing barrier enclosures for preventing viral contagion and provide safe administration of non-invasive ventilation therapy. I cannot begin to express my thanks to Timothy Morris for giving me the opportunity to collaborate on such impactful projects. Dr. Morris' dedication towards improving patient care even when burdened with a patient overload and departmental responsibilities was extraordinary. It was exciting working on these projects and I hope to continue working on the next phase. I would ike to extend my sincere thanks to Alexander Girgis for working with us to develop barrier enclosures for safe intubation of COVID-19 patients. The latter project was the quickest I have seen a concept translate into clinical use – 21 days.

For the development of VEIL and COSIE project during the COVID-19 pandemic we had to film high resolution videos of lengthy experiments while changing multiple variables. Despite short notice and the ominous situation of conducting experiments in a hospital during a pandemic, special thanks to Sarah and Cory Moesta, Mark Alexander, and the MMGM team who generously gave their time and helped film lengthy experiments past-midnight on multiple occassions. I will forever remember transforming the interventional pulmonology suite into a dark-field imaging suite by erecting a black canopy, and also having burritos and pizzas to make it through the long days at the hospital.

*98 Clayton Road, Clayton, Australia*

Before my journey to San Diego, I lived in Melbourne (Australia) where I pursued my bachelors and masters degrees in Mechanical Engineering. After a turbulent masters that was initially supposed to be my PhD, without the support of my friends in Melbourne, I would probably not have commenced pursuing PhD again. I am grateful to Amarin McDonnell, Neil Christian, Ganaka Chandrakumara, Peter Firus, Samuel Raymond, Vaibhav Verma, Dinaz Tamboli, Johnny Gong, Kimi Chen, Edward Liang-Hua, Mathew Lui, Caesar Perkasa and all my friends for everything during the 7 years I lived there. To Vaibhav Verma, the candid conversation we had on $8^{th}$ March 2013 at 98 Clayton Road helped me decide what field I really wanted to research on for my PhD, so thank you.

*Nakuru, Kenya*

Finally, this goes out to my teachers in Nakuru, Kenya. While growing up in Nakuru, I had never imagined that one day I would receive fellowships and pursue a PhD in Engineering, that too in the US. Thank you! the years 2005-2007 were particularly transformative for my educational career and if not for the efforts of my teachers back then, my journey would have ended before it began.

**Chapter Acknowledgements**

**Chapter 2** is partially based on the material prelminarily accepted in *Science Robotics* (2021), authored by Gopesh Tilvawala, Jessica Wen, David Santiago-Dieppa, Scott Pannell, Bernard Yan, Alexander Norbash, Alexander Khalessi and James Friend. The dissertation author wrote background and problems faced in endovascular neurosurgical procedures.

**Chapter 3** is partially based on the material that is prelminarily accepted in *Science Robotics* (2021), authored by Gopesh Tilvawala, Jessica Wen, David Santiago-Dieppa, Scott Pannell, Bernard Yan, Alexander Norbash, Alexander Khalessi and James Friend. The dissertation author designed microcatheter based on the clinical needs.

**Chapter 4** is partially based on the material that is prelminarily accepted in *Science Robotics* (2021), authored by Gopesh Tilvawala, Jessica Wen, David Santiago-Dieppa, Scott Pannell, Bernard Yan, Alexander Norbash, Alexander Khalessi and James Friend. The dissertation author fabricated the steerable tips and assembled the full length catheters.

**Chapter 5,** the first part of this chapter is based on the material published in *Soft Robotics* (2020) authored by Gopesh Tilvawala and James Friend [4]. The dissertation author was the primary researcher and author of this paper. The second part of this chapter is partially based on material that is prelminarily accepted in *Science Robotics* (2021), authored by Gopesh Tilvawala, Jessica Wen, David Santiago-Dieppa, Scott Pannell, Bernard Yan, Alexander Norbash, Alexander Khalessi and James Friend. The dissertation author worked on this chapter in entirety.

**Chapter 6** is partially based on the material that is prelminarily accepted in *Science Robotics* (2021), authored by Gopesh Tilvawala, Jessica Wen, David Santiago-Dieppa, Scott Pannell, Bernard Yan, Alexander Norbash, Alexander Khalessi, and James Friend. The dissertation author was responsible for 3D printing, acetone smoothing and assembly of the full-size model.

**Chapter 7** is entirely based on the material that is published in *Translation Vision Science and Technology* (2020) authored by Gopesh Tilvawala, Andrew Camp, James Friend, and Robert Weinreb [5]. The dissertation author was responsible fabrication, assembly, and testing of the device.

**Chapter 8** is entirely based on the material that is published in *Infection Control and Hospital Epidemiology* (2021), authored by Gopesh Tilvawala, Alex Grant, Jessica Wen, Teresa Wen, Ernesto Criado-Hidalgo, William Connacher, James Friend, and Timothy Morris [6]. The dissertation author was responsible for the device design, machining, assembly, experiments and image processing of the videos.

# VITA

| | |
|---|---|
| 2012 | B.E in Mechanical Engineering<br>Monash University, Melbourne (Australia) |
| 2014 | M.S in Engineering Sciences (Mechanical Engineering)<br>Monash University, Melbourne (Australia) |
| 2021 | PhD in Engineering Sciences (Mechanical Engineering)<br>University of California San Diego |

ABSTRACT OF THE DISSERTATION

# Micro-to-meso scale approaches for deformable soft robots and sensing capabilities in biomedical microdevices

by

Gopesh Tilvawala

Doctor of Philosophy in Engineering Sciences (Mechanical Engineering)

University of California San Diego, 2021

Professor James Friend, Chair

Micro-medical devices have found new life in medical applications, offering advanced control, precision, and safety in surgery to augment or sometimes replace surgeons. However, current medical devices' utility is limited just as a surgeon is, with all the functionality, all but the end tool outside the patient. Many interventional procedures would benefit from having the active medical device scaled down to fit within a few hundred micrometers, to work in the confined space of the eye, vasculature, lymphatic vessels, and so on, enabling complex motion and sensing at such a scale via remote or external control by the surgeon. Due to their inherent rigidity and size, traditional robotic tools cannot be utilized to achieve the desired clinical needs, and are limited to a few hundred niche applications.

The projects presented here have been constructed to deliver micro-scale tools for

some of the most challenging clinical needs in endovascular surgery and ophthalmology. Endovascular surgical intervention for aneurysm and stroke treatment requires a means to controllably orient a catheter deep within a patient's cerebral arteries in tortuous, complex, and challenging anatomical locations. The measurement of intraocular presure is another, for patients with artificial corneas to enable prompt, preventative treatment to avoid glaucomatous damage. The absence of controlled actuation and sensing at the sub-millimeter length scale is the leading cause of procedural failures in these medical applications.

Through a novel combination of large aspect ratio, soft-robotic structures and saline-driven micro-hydraulics, dexterous tools to translate commands of surgeons into complex motions within brain arteries are presented. High resolution pressure sensors are combined with micro-scale needles to enable effective measurement of intraocular pressure for patients with artificial lenses. Unlike passive fundamental studies or bench-top innovations, these projects deliver clinically functional medical devices. These approaches were validated *in vivo* to assess their performance and the results obtained lay the foundation for an entirely new discipline of dexterous sub-milimeter scale soft robotic tools for surgical intervention and sensing.

# Chapter 1

# Introduction

Macro-to-micro scale medical devices have found new life in medical applications, offering unprecedented control, precision, and safety in surgery to augment and replace human surgeons. However, current devices' utility is limited in ways identical to a human who carries all but the end tool outside the patient. Many interventional procedures would benefit from having the devices scaled down to fit into a few hundred micrometers, in unstructured anatomical locations as present within the eye, blood vessels and bronchi. Minimally invasive procedures in these locations that require dexterous surgical tools to enable complex motion and sensing at such a scale and remotely controlled by the surgeon are not available. The projects detailed in this disseration have been developed to deliver such technology for the some of the most challenging clinical needs in neurosurgery; endovascular treatment of intracranial aneurysms, and ophthalmology; measurement of intraocular pressure for patients with artificial corneas. The absence of controlled actuation and sensing at the sub-millimeter length scale is the leading cause of procedural failures in these medical applications. Subsequent to this, in light of the COVID-19 pandemic, barrier enclosures to enable safe administration of non-invasive ventilation therapy to patients experiencing hypoxemic respiratory difficulties were developed in an emergency response effort.

The focus of the present work has been subdivided into three studies:

- Steerable soft-robotic microcatheter
- Device for measurement of intraocular pressure
- Barrier enclosures for COVID-19 patients

These projects were designed from concept, through to design, fabrication, assembly, iterative testing and eventually animal trials. Below is a brief overview of the following chapters and their content:

**Chapter 2** is partially based on the material preliminarily accepted in *Science Robotics* (2021). This chapter provides a detailed overview of endovascular neurosurgery, the shortcomings of the existing catheters, and lays the premise for developing a steerable microcatheter.

**Chapter 3** is partially based on the material that is preliminarily accepted in *Science Robotics* (2021). This chapter provides details of the catheter design process, the clinical requirements, and dimensional constraints for the steerable microcatheter.

**Chapter 4** is partially based on the material that is preliminarily accepted in *Science Robotics* (2021). This chapter provides the detailed fabrication process, including intricate molding and casting details, assembly, and surface chemistry to prepare a clinically functional steerable micro-catheter.

**Chapter 5**, the first part of this chapter is based on the material published in *Soft Robotics* (2020) [4]. The second part of this chapter is partially based on material that is preliminarily accepted in *Science Robotics* (2020). This chapter includes biaxial membrane tests and analytical derivation required to obtain the first and second hyperelastic constants. The second half incorporated the hyperelastic constants obtained in the first half to implement a computational model to validate the experimentally obtained curvature and radial expansion for the steerable catheter.

**Chapter 6** is partially based on the material that is preliminarily accepted in *Science Robotics* (2021). The first part of this chapter describes the development of a representative silicone model of the vasculature from the femoral artery to the brain arteries. The model provides are vital step for the second part that decribes the *ex vivo* testing and validation of the steerable catheter paving the way for the animal trial. The last part provides details of the animal trial conducted at the Center for Future Surgery (CFS, UCSD).

**Chapter 7** is entirely based on the material that is published in *Translation Vision Science and Technology* (2020) [5]. This chapter describes the development of a needle based intraocular pressure sensing device from concept to successful completion of animal trials in rabbits. The device described enables measurement of the intraocular pressure in the anterior chamber of patients with artificial corneas.

**Chapter 8** is entirely based on the material that is published in *Infection Control and Hospital Epidemiology* (2021) [6]. This chapter describes the development of a barrier enclosure to safely administer non-invasive ventilation therapy to patients experiencing acute hypoxemic failure while preventing viral contagion. This chapter provides details begining with concept design, through manufacturing, assembly, clinical testing and eventually patient use.

**Chapter 9** provides concluding remarks and lays some prelminary framework for potential future work for along the lines of the projects described in this dissertation.

# Chapter 2

# Endovascular neurosurgical procedures

## 2.1 Macro-to-micro scale medical devices

Due to clinical demand for minimally invasive procedures and targeted therapies, medical robotics represents one of the fastest growing sectors in the medical device industry. The therapeutic and commercial success of robotic systems such as Intuitive Surgical's da Vinci system has spurred a number of commercial ventures targeting surgical applications, which echo the emerging trend in precision surgery with minimally invasive intervention for faster recovery and potentially improved outcomes. However, the majority of traditional robotic tools comprise of rigid components that are not designed to perform precise fine maneuvers in delicate unstructured surgical environments. Procedures that would benefit particularly from sub-millimeter diameter steerable catheters that enable fine precision procedures are shown in Figure 2.1. Among endovascular procedures, a subset of specialist procedures requiring access to small distal vessels that would benefit from dexterous locomotion of sub-millimeter diameter catheters are shown in Figure 2.1.

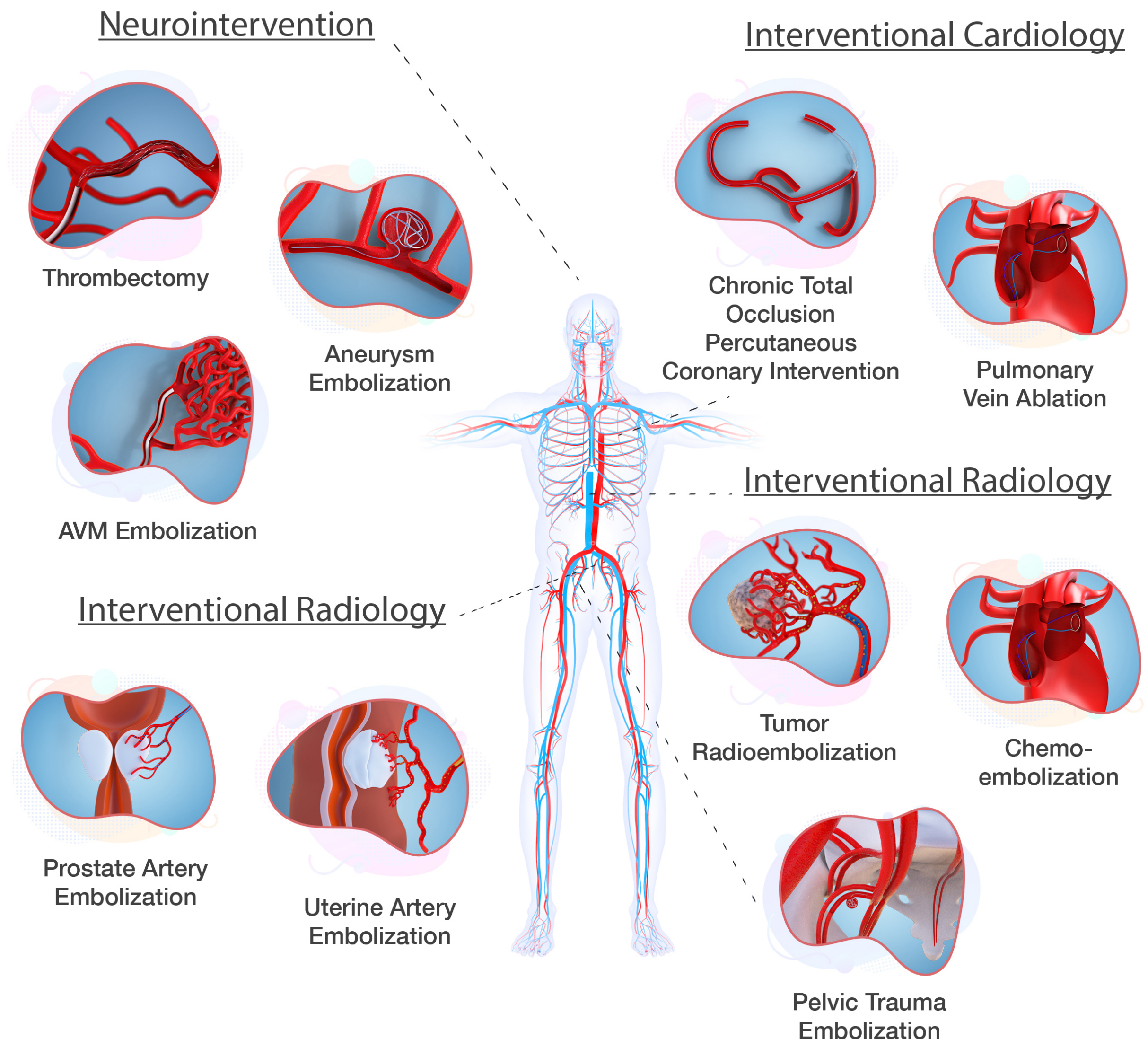

**Figure 2.1**: Endovascular procedures that would benefit from sub-millimeter diameter steerable catheters. Aneurysm embolization is the focus of this project, but steerable sub-millimeter catheters are broadly useful across the human vasculature.

One specific environment includes the smaller structures of distal blood vessels that gradually decrease in diameter is the brain vasculature. With a wide variety of vascular pathologies now treatable through endovascular procedures in several fields including but not limited to the cardiovascular space, there is a growing need for steerable tools and systems that can effectively aid in performing procedures in these smaller and more fragile endovascular environments with finer precision without causing damage.

## 2.2 Endovascular neurosurgery

Endovascular treatment of brain aneurysms via coil embolization in neurosurgery is one such procedure that may benefit from the ability to controllably orient a microcatheter tip. An estimated one in fifty people in the US have an unruptured intracranial aneurysm, a thin-walled blister-like lesion in a cerebral artery that is prone to rupture in the setting of increased blood pressures. A recent study indicates cerebral aneurysms affect 2% of the population worldwide [7,8], growing by over 5%/year [9] and are responsible for 500,000 deaths/year worldwide; half the victims are younger than 50 [10]. Annually, there are 30,000 new cases of brain aneurysm ruptures in the US alone [11]. Cerebral aneurysms and associated long-term medical complications impose an enormous economic burden ($500 million per year in the U.S [12]) due to morbidity and mortality often secondary to hemorrhagic stroke.

Cerebral aneurysms form due to weakness in the walls of blood vessels and excessive pressure from within the artery [13]. Typically once an intracranial saccular aneurysm is detected the treatment method is decided based on both aneurysmal and patient factors. Aneurysmal factors include location, size, morphology, presence of daughter sacs or multiple lobes. Patient factors include age, medical history and family history of subarachnoid hemorrhage [12]. If untreated, the consequences of a ruptured aneurysm are complex and undesired. Intervention for unruptured aneurysms is generally [14] known to be beneficial: without treatment, over 50% of those aneurysms of a size greater than 5 mm eventually rupture [15, 16]. For patients that suffer ruptured aneurysms, a significant proportion (57% [17] and 67% [18]) of first bleeding of a brain aneurysm leads to death [13], and half the survivors have long term disabilities.

In the case where aneurysm treatment is required, options include surgical clipping or endovascular coiling. Surgical clipping is an invasive surgical procedure that involves making an incision in the skull to locate the aneurysm and to place a metallic clip across the neck of the aneurysm in order to exclude it from blood circulation. Aneurysm treatment was limited to surgical clipping until the invention and broad clinical adoption of endovascular coil embolization [19–21], a minimally invasive approach that involves inserting a microcatheter at the femoral artery, navigating it through tortuous anatomy under radiological guidance to the cerebral aneurysm via the aortic arch and carotid arteries, and deploying detachable coils into the aneurysm. The coils aid to induce embolization within the aneurysm, effectively occluding it from blood flow. Endovascular coiling is now the most preferred, [22] relatively cost-effective, and statistically more successful option for treating cerebral aneurysms [23, 24].

Although over 50% of intracranial aneurysms are treated via endovascular coiling, the efficacy of endovascular aneurysm embolization is still inferior to traditional invasive clipping [25]. The current drawback of treatment through endovascular coiling (coil embolization) is the lack of steerability of the microcatheter and microguidewire during surgery. As the micro-catheter is guided from the femoral artery of the patient to the location of the cerebral aneurysm, three common problems are encountered: navigating tortuous vasculature, optimally directing the catheter tip to the center of the aneurysm dome, and holding it in a stable position to deploy coils and treat the aneurysm accounts for many coil embolization procedure failures. These include incomplete aneurysm occlusion [26], aneurysm recanalization [27], coil malposition [28], and intraoperative rupture [29, 30]. These failures can be attributed to unfavorable vessel tortuosity and aneurysm geometry. Furthermore, up to 25% of intracranial aneurysms cannot be endovascularly treated, often due to aneurysm location — where the vessel is too difficult to reach, or geometry — where the dome, neck, or angles are unfavorable for micro-catheter cannulation or coil support. Up to 25% of surgical neurointerventions fail in attempted endovascular treatment of intracranial aneurysms [25, 26]. The ability to treat aneurysms of unfavorable shape and size, and the durability of embolization coils in the dome post intervention remain challenges in the endovascular coiling technique [27].

In cases of severe carotid system tortuosity, intracranial positioning of microcatheters to access the aneurysm dome may be impossible or hazardous. In tortuous or fragile vasculature, turns of 180 degrees and 360 degrees are particularly difficult, catheterization often requires multiple attempts, and vasospasms are often induced [31]. Tortuous arterial anatomy forces micro-catheters along the outer curvature of the vessels at each turn, creating stresses on the vessel, a potential mechanism for vessel dissection [32]. Furthermore, minimizing overall procedure time is important to not only minimize costs, but to avoid excessive x-ray fluoroscopy exposure and associated risks such as thromboses or tumor growth [33–35].

To address the lack of steerability, catheter manufacturers provide 45°, 90°, and C-shaped tips in fixed orientations, and neurointerventionists will often retrieve, reshape, and reintroduce their microguidewire tips in hopes of accessing tortuous aneurysm geometries using a “trial and error" approach. However, upon retrieval of the guidewires, the catheter tip will return to its native shape and none of the catheters can be steered once inside blood vessels.

During certain instance coil embolization has failed (32% [36]) or is precluded (25% [37]) and clipping is preferred instead due to tortuous navigational vasculature. Even when the current microguidewires with custom preshaped tips can reach the aneurysm location by repeated *torquing*, *pushing* and *prodding*, in a proportion of cases it cannot be steered into the dome of the aneurysm because it is simply pointing in the wrong direction. This results in loss of precious angiography time as the micro-guidewire is retrieved, reshaped based on the aneurysm dimensions and then reinserted in hopes of successfully accessing the aneurysm dome; a presently common process despite inconsistently leading to successful entry. At times this can result in intra-procedural aneurysm rupture during treatment (2 - 4 % [38,39]). Furthermore, in present surgeries once the catheter is inserted in the dome of the aneurysm and is pointing in the direction of the rupture/weaker part of the aneurysm, there is no way to steer the tip away from the ruptured side.

Although quantitative measures for the difficulties experienced in existing methods is limited in literature, the clinical need for navigation through tortuous anatomy and catheterization of challenging vessels has been reported [40–42]. The primary cause of inability to reach the dome of the aneurysm during treatment using endovascular coiling has been the inability to steer the catheter tip while in procedure.

## 2.3 Previous approaches for catheter steering

There have been advancements in other sophisticade implantables such as flow diversion devices and intracranial stents. However, these fail to alleviate the issues faced due to lack of steerability at the micro-catheters tip and furthermore are contra-indicated for ruptured aneurysms due to the anti-platelet/anti-coagulant requirement. Additionally, it can be very difficult to deploy stents around sharp curves such as the carotid siphon [43], and proximal tortuous vessels add to this difficulty.

### 2.3.1 Magnetic systems

Magnetic approaches to catheter steering were proposed in the 1950's [44]. Despite limitations associated with miniaturization of magnetic actuation [45, 46], magnetically driven micro- and nanorobots have made valuable contributions towards steerable catheters [47–55], micro-scale flagella [56], and tunable microstructures [57]. A more recent study combined soft polymer structures and ferromagnetic domains to steer continuum soft robots using an externally applied magnetic field [58]. Magnetically driven steering has been demonstrated previously in humans in pulmonary vein ablation [59, 60] and in cardiac electrophysiology procedures [61]. A key challenge to overcome with magnetic actuation is the magnitude of magnetic force needed to drive actions. When a system is miniaturized, the force generated magnetically decreases by a factor 4 [45]; this implies a significantly large magnetic force is required as devices are scaled down, while a large distance between the driving magnet and medium must be maintained. In addition, implementation of magnetically controlled catheters requires costly infrastructure such as robotic arms and external control systems [62].

### 2.3.2 Wire-pulley systems

Pull-wire systems, based on the Bowden cable technique, were proposed as a means of catheter steering in the 1960's [63–67]. Wires run from the proximal end of the catheter to the distal tip where a deflection can be achieved based on the push or pull motion of the cables. These range from single cable systems for unidirectional deflection [68] to multi-segment [69] for dual directional control. Pull-wire systems are hampered by inevitable undesired torsion [70], buckling [71], internal friction [72], and external friction [73, 74]. These factors, and the stiffening often used to avoid them, can independently or together result in undesired tip motion resulting in vascular damage [75–77].

### 2.3.3 Piezoelectric ultrasonic systems

Piezoelectric ultrasonic approaches [78, 79] have also been proposed, but currently face practical reliability and safety challenges. Using vibration transmitted across a contact interface to a steerable component, the devices are liable to lose the steerable component or exhibit unanticipated motions when in contact with the vascular wall. They also require 1 MHz or greater frequency oscillating electrical signals to be transmitted to the distal tip, and neither wired nor wireless methods are able to do this to date.

## 2.4 Soft Robotics and steerable actuators

Traditional robots are embedded with various rigid components which limit their use in delicate and unstructured environments as required in minimally invasive surgery. A large variety of biological organisms exhibit complex movements with soft structures, for instance octopus arms or elephant trunks which comprise of muscular hydrostats and plant cells which can change shape when pressurized by osmosis [80]. This fascinating natural behaviour has led to an array of bioinspired soft robots, usually driven pneumatically or hydraulically.

Hydraulic and pneumatic microactuators can be divided into three distinct categories: elastic fluid actuators, piston-cylinder fluidic actuators and drag based fluidic actuators [1].

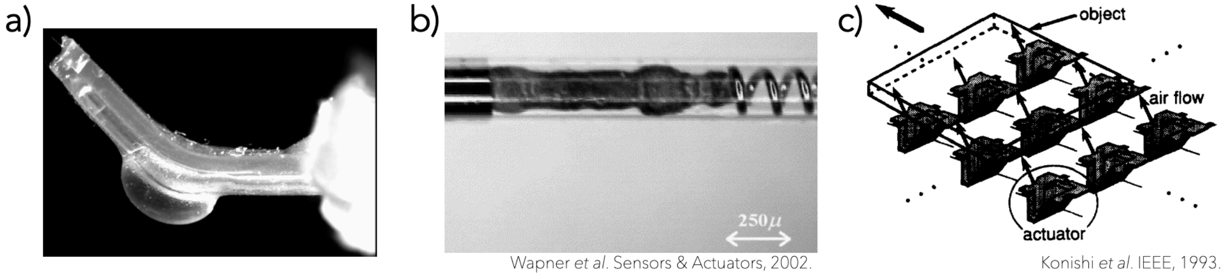

Wapner *et al*. Sensors & Actuators, 2002.

Konishi *et al*. IEEE, 1993.

**Figure 2.2**: Categories of hydraulic and pneumatic actuators. Image reproduced from De Volder *et al* [1].

Elastic fluid actuators comprise of components made of an elastic material that can be actuated by application of fluid pressure, usually applied on a membrane, balloon or bellow to perform a desired motion.

**Figure 2.3**: Types of elastic fluidic actuators. Image reproduced from De Volder *et al* [1].

Over the past decade, the burgeoning field of soft robotics; a subfield of robotics that comprises of highly deformable materials typically drawn into bioinspired 3D structures has seen unprecendented growth and gained traction both in scientific research and a variety of applied technology [1, 81–84] ranging from anatomical replacements such as prosthetic limbs to surgical tools [85–89]. Anatomical replacements include prosthetic limbs, hands and sensory robots used to translate nervous signals into physical motion meant to replicate the functionality of the real body part. Soft actuators can also be used to access tortuous paths and perform compounded miniature movements in minimally invasive surgery which would otherwise require the invasive route or be inaccessible altogether. Although various soft actuators have been proposed to conduct complex surgical manouvres over the last two decades, few if any have translated into clinical application. However, owing to rising demand and advances in microfabrication techniques the field is rapidly progressing towards miniature devices feasible for adaptation into clinical practice.

The actuation mechanism, materials, design and fabrication method for soft robots is dependent on the targets. Soft robots have been developed over a wide range of length scales which is dependent on the application being targetted. For instance, prosthetic limbs require features that are $10^{-1}$-$10^{-2}$m where as actuators for surgery range from $10^{-3}$ to feature sizes up to $10^{-6}$ m depending on the anatomical part being treated. The latter is also dependent on the surgery route being opted: minimally invasive or otherwise.

Embedded pneumatic networks (PneuNets): soft actuators that link balloons of different wall thicknesses on either side [90, 91], have previously been used to develop a range of actuators. These include a star-fish shaped multifunctional gripper device with tip-to-tip diameters of 9-14 cm that demonstrated gripping of chicken eggs, thin tubes, threads and mice [92], and 1 cm diameter soft robotic tentacles with three-dimensional mobility enabled by 4 mm wide channels to grip and manipulate objects with complex shapes [93]. Other studies at a relatively larger scale, $15(\mathrm{L})\times 2(\mathrm{W})\times 1(\mathrm{H})$ cm, presented pneumatically actuated multi gait soft robots made using soft lithography with different sections of PneuNets to perform a variety of motions such as crawling, undulating into gaps and supporting objects of much higher density [94, 95]. This was extended at an even larger scale (65 cm long) to make an untethered version using heat resistant silicone to perform motions such as walking, lifting weight in extreme temperature environments ranging from -20° to 300°C. With advancements in 3D printing and soft lithography, Wehner *et al.* presented an eight arm soft robot dubbed the "octobot" [96], where each arm can be pneumatically controlled to alternate between actuation states. At $6(\mathrm{L})\times 6(\mathrm{W})$ cm, and actuation pressures of 3-9 psi, the arms powered by hydrogen peroxide as fuel, allow for untethered actuation.

At relatively smaller length scales, Parry *et al.* first analyzed the joint angle and torque developed at the hinge joint of spider legs as a function of internal pressure generated via microfluidic actuation [97]. However, due to the complicated 3D structure, it was four decades later a physical model of a spider leg was fabricated and tested [98]; with 1 mm diameter microjoints it exhibited bending angles of 40 degrees with 20 $\mu$Nm of bending moment at driving pressures of 15 psi. Suzumori *et al.* first developed a 1-12 mm flexible balloon microactuator with three internal chambers that relies on electro-pneumatic or electro-hydraulic actuation to inflate the chambers at upto 60 psi to obtain bending up to 100 degrees for a 4 mm version [99]. Fiber-reinforcement in the circular direction was used to promote axial deformation and resist radial deformation while spiral reinforcement promoted rotational displacement. The 12 mm diameter version of this was later extended to combine multiple FMA's to replicate the functions of a human hand such as holding, pinching, grasping and rotating [100]. Subsequent to this various studies utilized stereolithography to fabricate balloon actuators utilized for conveyance of loads [101–103].

Simaan *et al.* [104] utilized Nitinol tubes to make a 4.2 mm diameter multi backbone snake like mechanism that can bend 90° in any direction for laryngeal surgery. Subsequently, the optimized motion of the same device was used for suturing [105]. Kim *et al* integrated a stretchable mesh sensor on a balloon catheter that can be used in cardiac electrophysiological mapping and ablation therapy [106].

The first balloon based surgical tool, comprising of 3 balloons actuated via resistive heating of nitrogen to generate differential pressure was used to steer a 4 mm diameter catheter in the desired direction at pressures of 3 psi [107]. Later, to eliminate traditional spatula induced tissue damage in neurosurgery, a 70(L)×9.6(W)×2.2(H) mm latex balloon actuator operating at 15 psi, was used to conduct complex bending maneuvers between the brain and endocranium of a pig [108]. Extending into the ophthalmic space, Watanabe *et al.* developed a 3×3×0.1 mm PDMS pneumatic balloon actuator requiring a bending moment of 3 mN to demonstrate smooth *in vivo* operations on the eyeball of a pig without causing eyeball damage [109]. At the sub-milimeter length scales, a parylene balloon actuator driven by electrolysis to generate bending motion was used as a neural probe [110].

Balloon actuators have also been used to fabricate fluid actuated PDMS microgrippers (1(W)×3(L) mm) requiring 400 kPa for actuation [90, 91]. In a separate study, 1 mm diameter parylene balloon biological microhands [111], requiring 115 psi for actuation demonstrated manipulation of capelin eggs without causing damage.

Paek *et al.* presented a high aspect ratio microtube with a single channel for actuation to safely handle delicate micro-objects [112]. The microrobotic tentacles had an inner diameter of 100 $\mu$m and an asymmetrical wall thickness with the thicker side being 36 $\mu$m and the thinner side being 8 $\mu$m, implying an average outer diameter of 150 $\mu$m. These were fabricated to lengths of 5-8 mm and required 4-10 psi for actuation. While the wall thickness and outer diameter may not be consistently repeatable with high accuracy, the soft tentacles were used to successfully hold 600 $\mu$m diameter capelin eggs and ants by actuating the tip into a spiral. In the most recent study involving the penetration mechanics of a beetle intromittent organ showed how the challenge in inflation induced bending of high aspect ratio soft structures without buckling or rupturing is solved by nature [113], and could be used for the development of safer catheters.

## 2.5 Limitations of existing fabrication methods

Fabrication methods have advanced over the last half century to enable machining arbitrary shapes to the micro-scale. Progress in photolithography, nanoimprint lithography, two-photon lithography to electron-beam lithography and ion-beam machining have enabled the creation of massively parallel integrated semiconductor circuits, microelectromechanical (MEMs) devices, and micro and nanofluidics. These technologies have revolutionized medical devices and practices [114, 115]. However, manufacturing arbitrarily-shaped structures using hyperelastic materials at length scales between 10 $\mu$m and 1 mm remains a challenge due to the convergence of van der Waals, electrostatic, gravitational, and other forces of similar magnitudes at this scale, making machining and manufacturing difficult [116]. Both photolithography and 3D printing are inadequate for manufacturing devices at these length scales. Despite this, advancements in manufacturing methods have produced reductions in catheter diameters down to 1.8 Fr (600 $\mu$m). This has enabled new endovascular techniques at more distal anatomical locations which is accompanied by increased tortuosity, additional bifurcations, and decreasing vessel diameters. This added complexity of distal vessel pathologies requires even more precise positioning for device deployment for effective treatment, requiring dexterous maneuvers by the interventionist [117–119]. As a result, robotic-actuator assistance has grown to become a pressing unmet need in interventional procedures.

With readily available 3D printing and CNC machining capabilities, complex mold designs at length scales above 1 millimeter are relatively easy to fabricate. Over the last few decades, microfabrication technology has seen immense growth, this is evidenced by the wide variety of fabrication methods presently available. These include though are not limited to photolithography, nano-imprinting, hot-embossing among many others which enable fabrication of designs in the order of $10^{-9}$ m to $5 \times 10^{-6}$ m. However, hitherto there have been limited attempts to combine microfabrication methods with the burgeoning field of soft robotics to develop tools at the $50\mu$ m to 1 mm length scale as required for delicate micro-surgical procedures.

## 2.6 Clinical rationale for steerable catheters

Randomized controlled trials have demonstrated that the use of steerable sheaths in procedures such as ablation for atrial fibrillation results in reduced procedure time and X-ray exposure as well as improved single procedure success rates likely due to improved precision of ablation target access [120]. Comparative studies between steerable and non-steerable catheters have also demonstrated significant reductions in procedure time and improvements in patient safety in patent foramen ovale closure and mitral valve repair [121–123]. Steerable catheters have also been demonstrated to yield better positioning of sophisticated implants in atrial septal defect repair and mitral valve clipping [124, 125]. Although steerable sheaths are now commonly used, some limitations remain [126]. Commercially available steerable sheaths are typically no smaller than 8F, and deflection is limited to a single plane [126]. Steerable catheters are a potential solution, though are not yet widely available.

## 2.7 Proposed approach

In addition to the clinical need for steerable catheters, a significant step is to recognize that the safe and broadly accepted use of microballoons in neurointervention, represents a crude form of soft robotics. Balloon catheters have been frequently used to conduct angioplasty or balloon septostomy via cardiac catheterization (heart cath), tuboplasty in uterine catheterization pyeloplasty using a detachable inflatable balloon stent positioned via a cystocopic transvesicular approach. In neurointervention, balloon catheters are frequently used to reverse blood flow during ischemic stroke clot retrieval and to perform balloon assisted coiling in difficult to access tortuous vasculature locations. The focus of the next chapter is on the design constraints based on the clinical needs leading to a novel fabrication method synthesizing micro-fabrication and soft-robotics to develop a steerable tip micro-catheter that has potential to overcome the short-comings of the current devices.

## 2.8 Acknowledgements

**Chapter 2** is partially based on the material prelminarily accepted in *Science Robotics* (2021), authored by Gopesh Tilvawala, Jessica Wen, David Santiago-Dieppa, Scott Pannell, Bernard Yan, Alexander Norbash, Alexander Khalessi and James Friend. The dissertation author wrote background and problems faced in endovascular neurosurgical procedures.

# Chapter 3

# Catheter design

## 3.1 Endovascular surgical approach

Endovascular surgery involves inserting catheters from the femoral artery near the groin and navigating them to the desired location for treatment. The dimensions and mechanical properties of the catheter vary depending on the target disease indication. The material choice and catheter mechanics are decided based on the confluence of size, tortuosity of the target geometry, delicate anatomy, and surrounding environment. For instance, general vascular procedures near the descending thoracic aorta and the abdominal aorta require large bore catheters. Cardiovascular procedures require slightly smaller catheters, and neuro-endovascular procedures require micro-catheters (<1 mm diameter).

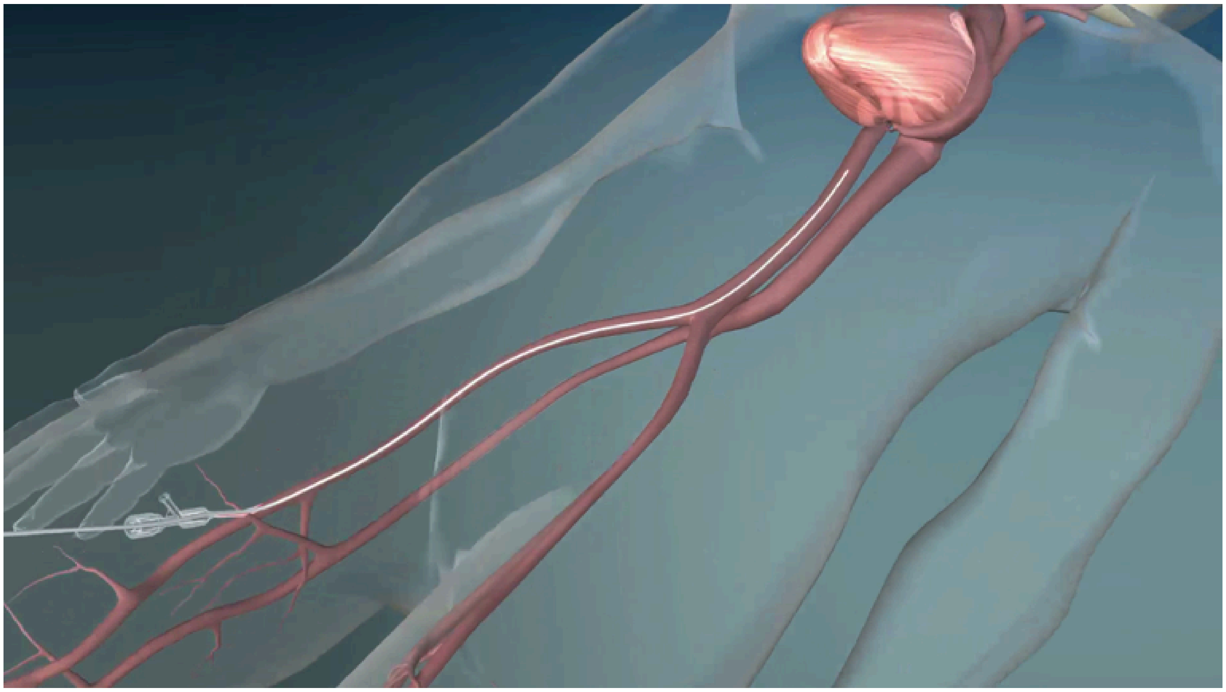

**Figure 3.1**: Illustration of the insertion of a catheter at the femoral artery, navigated to the heart.

During a typical neuro-endovascular procedure, first an introducer is inserted into the femoral artery (Fig. 3.1); this provides a large bore space to enable insertion of the guide catheter (Neuro 070 in Fig. 3.2). Guide catheters typically have diameters within a range of 5-8 Fr (1.67 - 2.67 mm) and are advanced to the base of the internal carotid artery using large diameter guidewires (0.041" = 1 mm). The guidewires have a curved tip and are used to lead the catheter via torquing. Once the guide catheter is positioned, a reperfusion catheter (Reperfusion 041 in Fig. 3.2), that ranges over 4-5 Fr (1.33 - 1.67 mm) is advanced within the guide catheter. The reperfusion catheter is positioned at the top of the internal carotid artery and provides a transitional zone between the guide catheter and the microcatheter. The microcatheter (SL10 microcatheter in Fig. 3.2), normally 2.7 Fr (900$\mu$m) in diameter is inserted and led using a micro guidewire (0.014" = 360 $\mu$m diameter).

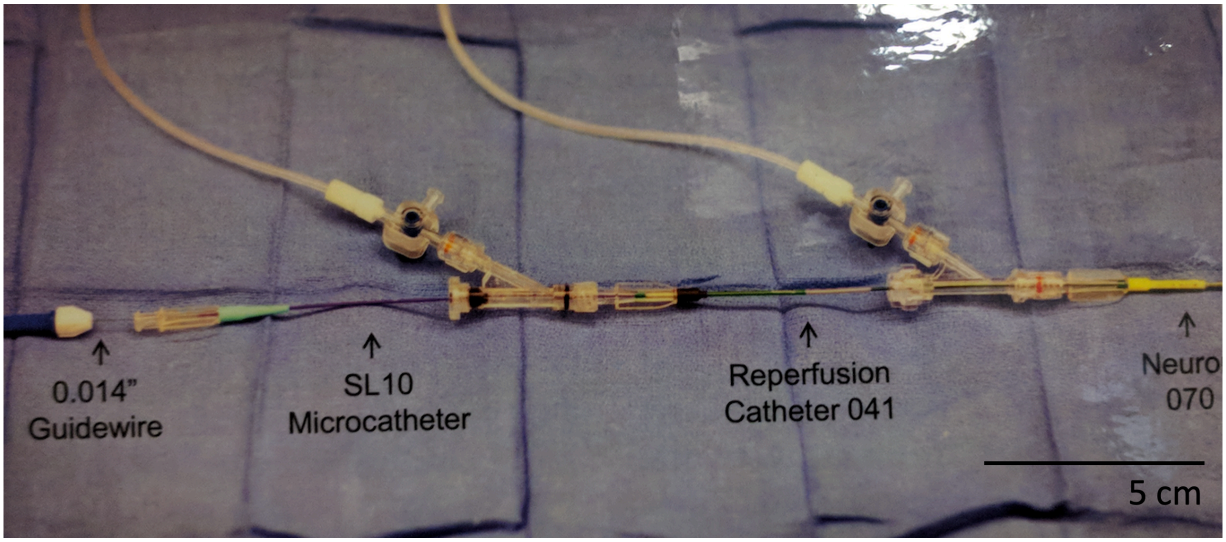

**Figure 3.2**: Endovascular catheter setup.

Each of the rotating hemostatic valves (RHV's) are connected to an external flush line establishing a continuous fluid column between the flush system and the catheter a pressure of 300 mmHg. Heparinized saline is used to as the flushing fluid within the catheters to prevent blood from clotting provide a smooth passageway for devices passing through the central lumen of the catheters.

## 3.2 Dimensional constrains

Cerebral arteries supplying blood to the different parts of the brain begin above the neck at the base of the internal carotid artery (ICA) and go through to the middle carotid artery (MCA) bifurcation which leads to smaller and more tortuous cerebral vessels. The MCA has a diameter of approximately 2.6 mm [127] (Fig. 3.3); blood vessel branches beyond the MCA gradually decrease in size to 1 mm or less [128]. The majority of aneurysms occur in vessels of 1.5 mm diameter or less. To navigate smoothly within the cerebral blood vessels, current gold standard microcatheters have an outer diameter of 900 $\mu$m (3 Fr) and inner diameter of 400 $\mu$m (1.2 Fr) to provide a lumen for guidewires, detachable coils, and sophisticated endovascular devices such as stents and flow diverters.

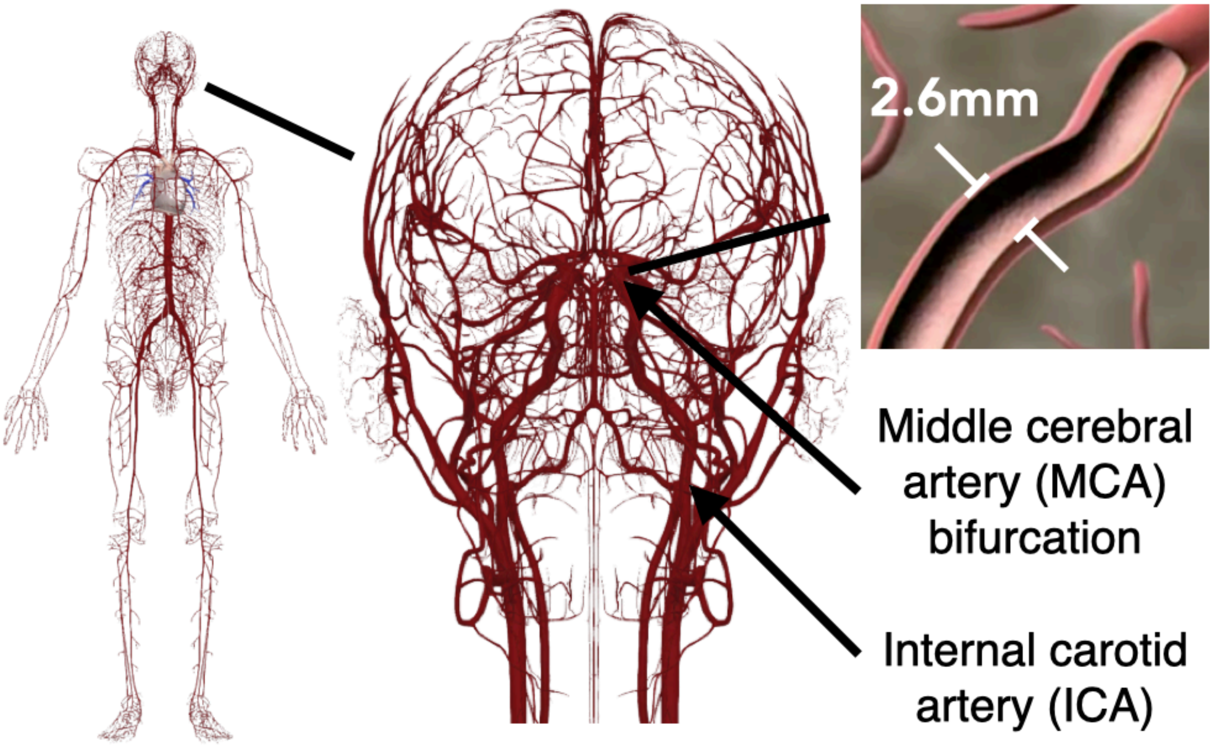

**Figure 3.3**: Illustration of middle carotid artery dimensions.

## 3.3 Proposed design of the soft-robotic microcatheter

To provide clinical compatibility and immediate familiarity when used in existing procedures, and to augment the existing guidewires and implantable coils, the steerable tip micro-catheter described here was designed to have an outer diameter of 900-$\mu$m, and a 400-$\mu$m diameter central lumen. The wall of the micro-catheter encloses four 50-$\mu$m diameter channels for hydraulic actuation (Fig. 3.4 b). Upon pressurizing one of the 50-$\mu$m diameter channels, an axial differential strain is induced in the structure about its midplane —the axis of symmetry along the length of the tip —causing bending of the tip away from the pressurized channel (Fig. 3.4 c).

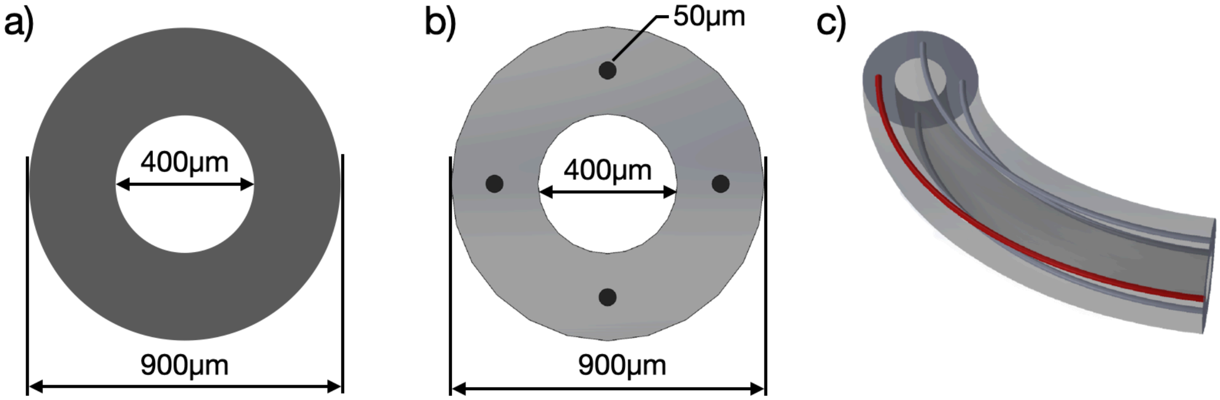

**Figure 3.4**: Dimensional constraints, a) existing gold standard catheters, b) proposed steerable catheter design and c) working principle of the soft-robotic microcatheter via with hydraulic actuation.

To provide clinical compatibility and immediate familiarity when used in existing procedures, the steerable tip micro-catheter described here was designed to have an outer diameter of 900 $\mu$m, enclosing four 50 $\mu$m diameter channels for hydraulic actuation and a 400 $\mu$m diameter central lumen. Upon pressurizing one of the 50 $\mu$m diameter channels, an axial differential strain is induced in the structure about its mid-plane—the axis of symmetry along the length of the tip—causing bending of the tip away from the inflated channel (Fig. 2.2 b).

Accessing the smaller tubular structures in arteries requires dexterous interventional systems of catheters, wires, and devices that can perform complex maneuvers in three-dimensional space. Novel and existing fabrication techniques can be augmented to create these steerable tools. Due to their hyperelastic and deformable nature, soft-bodied actuators demonstrate promise for traversing tortuous paths and performing compound miniature movements in interventional procedures that would otherwise require an invasive route or would altogether be inaccessible. The next chapter provides the detailed fabrication and assembly process.

## 3.4 Acknowledgements

**Chapter 3** is partially based on the material that is prelminarily accepted in *Science Robotics* (2021), authored by Gopesh Tilvawala, Jessica Wen, David Santiago-Dieppa, Scott Pannell, Bernard Yan, Alexander Norbash, Alexander Khalessi and James Friend. The dissertation author designed microcatheter based on the clinical needs.

# Chapter 4

# Fabrication method

Catheters are the primary tool utilized for treating vascular pathologies such as cerebral aneurysms via endovascular approaches. Although catheter technology has improved over the past few decades, with notable advancements in *pushability* [72] and polymer coatings [129], the inability to steer the catheter tip *in vivo* remains [119]. This complicates the navigation of tortuous anatomy, gaining access into geometrically complex vascular pathologies that occur with aneurysms, and placement of the catheter tip in a stable position while deploying coils, stents or sophisticated implants. Current gold standard aneurysm embolization procedures use curved-tip guidewires to provide access via a previously introduced guidewire into aneurysm geometries that require acute catheter turns from the parent artery. However, upon retrieval of the guidewire in preparation to deliver coils, the catheter tip bends back to its original curvature, preventing coil deployment in the desired optimal direction. The need to develop a fabrication approach for soft robotic steerable catheters arises from the confluence of a clinically unmet need and the engineering challenge described in chapter 2. Despite advances in industrial extrusion and manufacturing methods, given the design constraints described in the previous chapter (chapter 3), the required feature size presents a challenge even for existing large scale industries with experience. Feedback received includes the feature sizes are too small, impossible to extrude, or not feasible with the existing machinery available. This consolidates the need to develop a new approach to fabricate micro-scale soft robotic devices with high aspect ratio features.

## 4.1 Mold cast technique

The fabrication of the steerable tip is a multi-step process starting with preparation of the molds, followed by formation of thin polymer films, alignment of metal rods, and casting of the silicone rubber before demolding to obtain the steerable tips. A meso-scale molding process employing thin wires cast with silicone rubber in polyurethane plastic molds was used.

### 4.1.1 Mold preparation

To fabricate a mold for a circular catheter tip, 900$\mu$m diameter glass rods, and 450$\mu$m high rectangular glass sheets were laid out in parallel on a microscope slide as shown in Figure 6.2. The capillary tubes and glass strips we bonded to the microscope slide using using a UV cured epoxy (NOA60, Norland Inc.). As a general rule it is important to ensure the diameter of the circular tubes, $D$ is equal to that required for the final silicone rubber tubing, and the height of the rectangular glass tubing is $D/2$.

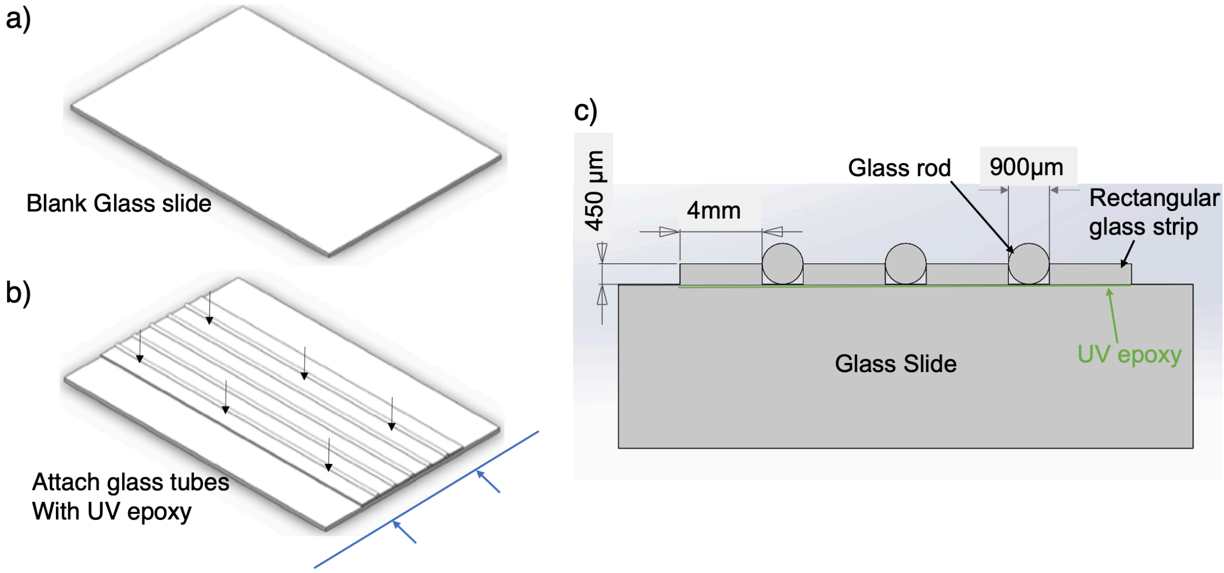

**Figure 4.1**: Ilustration of mold preparation process. a) Circular glass rods (diameter 900 $\mu$ m) were placed next to rectangular glass sheets (height 450 $\mu$ m) and bonded to a microscope glass slide using UV epoxy (b).

Subsequent to this, the assembly was placed in a dessicator to deposit silane (as shown in Figure 4.2a) through chemical vapor deposition under −0.05 MPa vacuum for 1 hr. This provides a nanometer thickness release coating on the surface of the glass tubes and flat glass strips which will enable easy demolding of the mold in the next step. The molding material, a two-part polyurethane plastic, Smooth-Cast® 327 (Smooth On, Inc), selected for its high hardness and smooth finish, was poured over the assembly and degassed, Figure 4.2b. Upon curing this forms a negative of the catheters' final outer diameter comprising of a high hardness material with a smooth surface finish, Figure 4.2e.

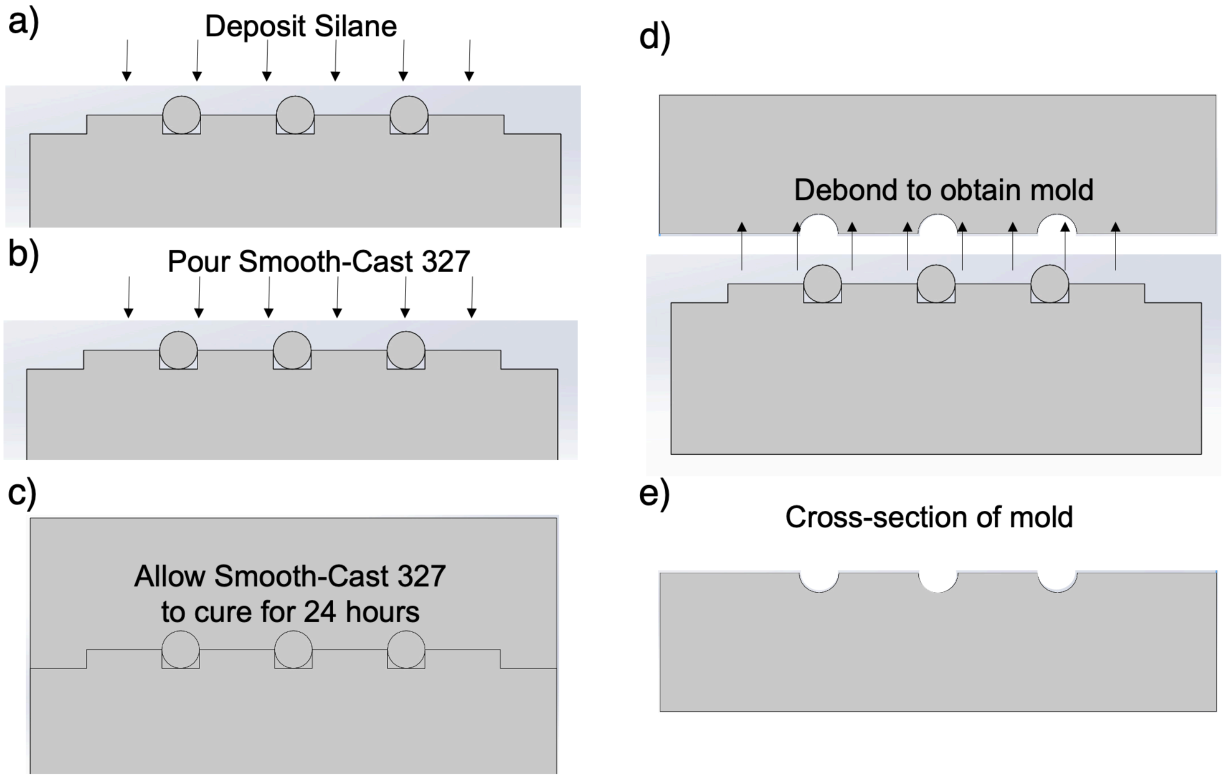

**Figure 4.2**: Ilustration of mold formation process. a) Silane was deposited via CVD on the assembly, b) Smooth-Cast® 327 was poured over the assembly and allowed to cure for 24 hours. c) Upon curing d) de-bonded to obtain e) the mold.

### 4.1.2 Casting the steerable tip

A custom extruded multibore glass-capillary tube (Vitrocom, Inc, NJ, USA) with an outer diameter of 900 $\mu$m, inner diameter of 400 $\mu$m, enclosing four 60 $\mu$m channels in the wall was placed in the mold. Two molds were placed facing each other with the custom manufactured glass capillary tube hemmed between them, Fig. 4.3b. A 400 $\mu$m diameter glass capillary tube was placed in the central lumen of the custom manufactured multi-bore tube, extending out by 30 mm. Dragon-Skin® 10 SLOW (Smooth On, Inc) was pumped into the the Smooth-Cast® 327 mold and compressed air used to clear the channel and leave a thin ( 20 $\mu$m) layer of Dragon-Skin, Fig. 4.3e. The Dragon-Skin was cured at 100°C for 30 minutes.

Heat curing Dragon-Skin causes the material to stiffen relative to curing at room temperature [4].

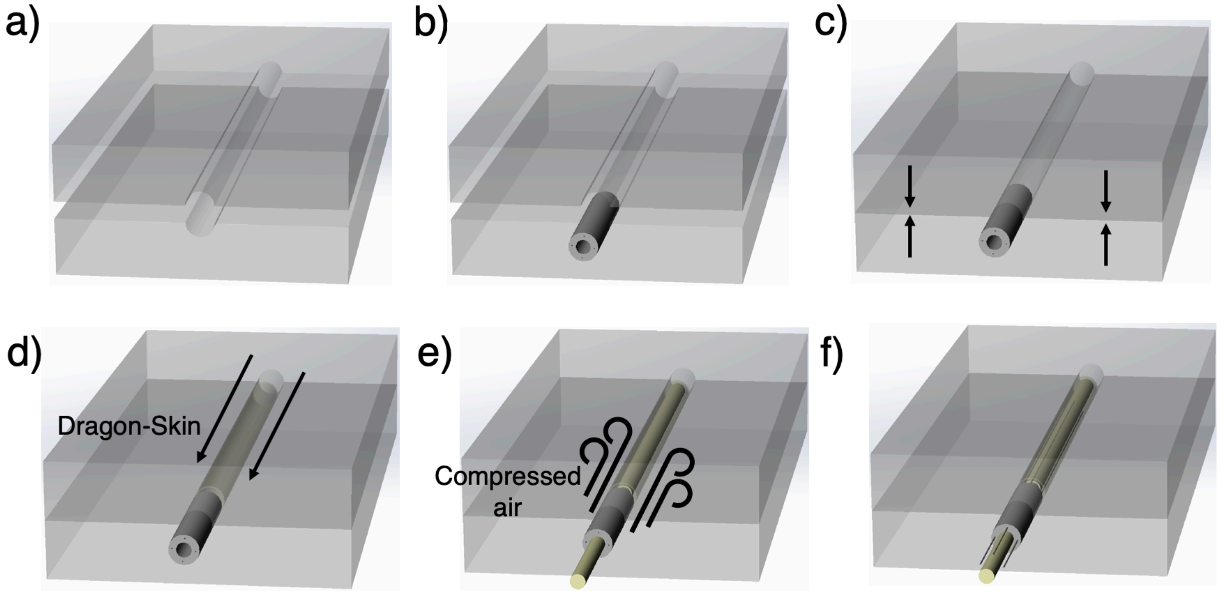

**Figure 4.3**: Ilustration of the casting process. a) Two molds are placed facing each other, b) A custom extruded glass-capillary tube is placed in the mold and c) hemmed between the two molds. d) Dragon-Skin® 10 SLOW (Smooth On, Inc) was pumped into the mold and compressed air (2 psi) was pumped through the custom extruded glass capillary tube. e) (Silane was deposited via CVD on the assembly, b) Smooth-Cast® 327 was poured over the assembly and allowed to cure for 24 hours. c) Upon curing de-bonded to obtain the mold e).

Thin, custom manufactured rods of equal length with a diameter of 50 $\mu$m and made of 3% rhenium-tungsten (Mitaka co ltd, Tokyo, Japan) were slipped into the 60$\mu$m bores of the multi-bore tube so that they extend out by 15 mm in the mold as shown in Figure 4.3f. The 3% rhenium-tungsten is used instead of 100% tungsten for higher hardness and a smooth surface finish. The four rods are placed parallel to each other in a square array as defined by the 4 bores of the glass tubing. A 1:1 mixture by weight of the Dragon-Skin® 10 SLOW and hexane (CAS 110–54–3, 95% anhydrous hexane, SigmaAldrich, St. Louis, MO USA), prepared for its low viscosity and mechanical properties was injected into the region enclosed by 100% Dragon-Skin® 10 SLOW formed in the previous step. Upon curing, the rods and the 400$\mu$m glass capillary tube were carefully withdrawn leaving behind the cavities for the hydraulic microchannels. The Smooth-Cast® 327 molds were then separated to obtain the silicone rubber tubing with four hydraulic channels measuring 50$\mu$m in diameter and a 400$\mu$m central lumen, image and cross-section of the tubing shown in Figure 4.4.

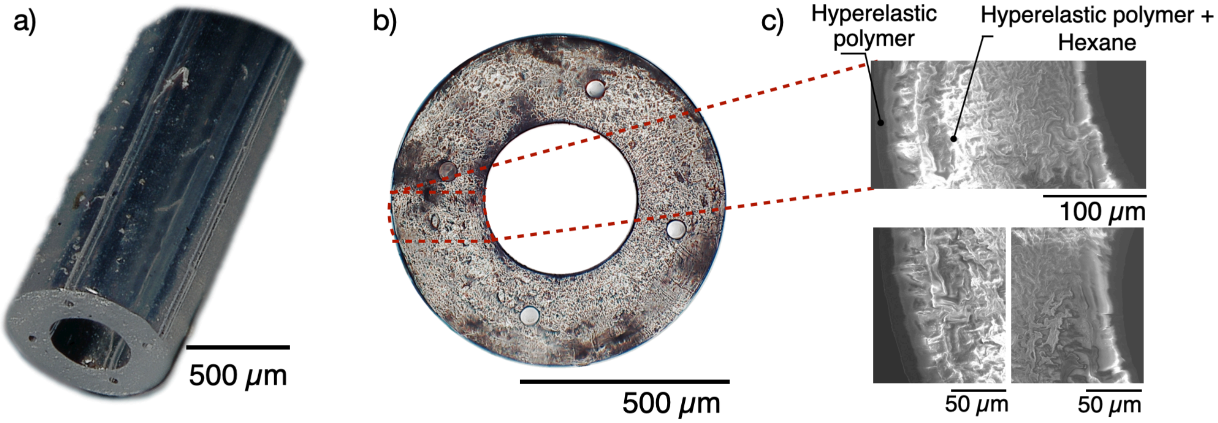

**Figure 4.4**: a) Plan and b) cross-section images of the as-fabricated steerable tip tubing, with a length of 15mm, an outer diameter of 900 $\mu$m, an inner diameter of 400 $\mu$m, and four 50 $\mu$m channels in the tube wall. The relatively rigid coating upon the softer interior material that forms the hydraulically-driven tip is visible via SEM cross-section images, and is approximately 25 $\mu$m thick.

### 4.1.3 Biplane x-ray visible radiopacity

To ensure the steerable tip is visible via digital biplane x-ray typical in interventional angiography suites, gold radiopaque markers (27121A, Johnson Matthey, San Diego, CA USA) were embedded in the soft polymer tip. The markers are positioned at three distinct locations. The first and second markers indicate the beginning and end of the steerable portion of the micro-catheter tip. The third marker, the most proximal, is located 3 cm from the distal end of the catheter tip and during procedures aligns with the marker on the coil pusher of an embolization coil. This third marker aids in visualization of the point at which an entire coil has been deployed into an aneurysm, indicating that the pusher should not be advanced further and can be detached. This marker could be similarly used for other types of devices, including flow diverters or stents that may be placed in the lumen of the micro-catheter. The remainder of the non-steerable portion of the catheter was made with custom-extruded barium-filled pebax tubing to achieve clinically required radiopacity and transitional stiffness, described in the next section

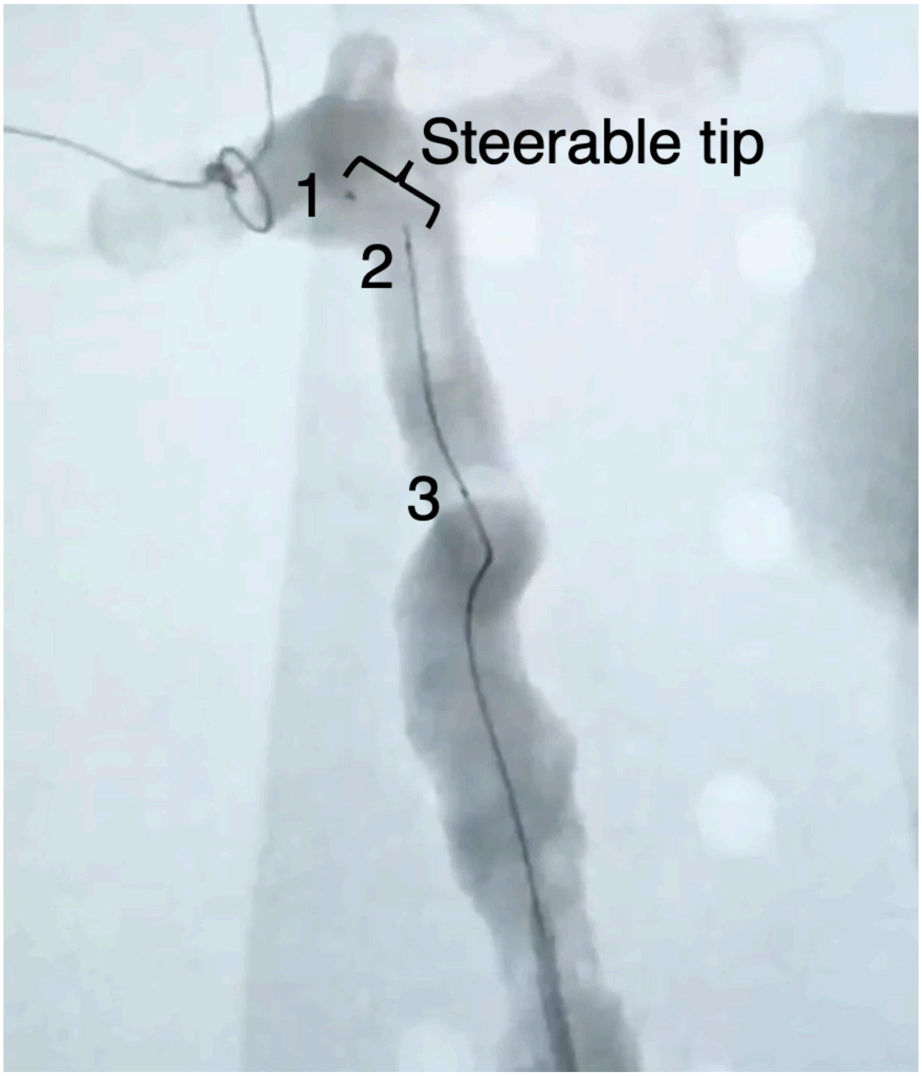

**Figure 4.5**: Image of the micro-catheter as visualized under bi-plane x-ray in the *ex vivo* model showing the radiopaque markers and their respective locations. Markers 1 and 2 are at the begining and end of the steerable tip. Marker 3 is located 3 cm from Marker 1.

### 4.1.4 Assembly of full length devices with transitional stiffness:

For each assembled microcather, the 400 $\mu$m diameter central lumen and 50 $\mu$m-diameter channels were tethered to a handheld controller through microtubing to luer lock connectors. This process involves connecting polyimide micro-tubing (Microlumen, Oldsmar, FL USA) with the hyperelastic material steerable tip. A special epoxy (LOCTITE ®4061 ™, CT, USA) that enables bonding of elastomeric materials to plastic was used to complete this bonding step.

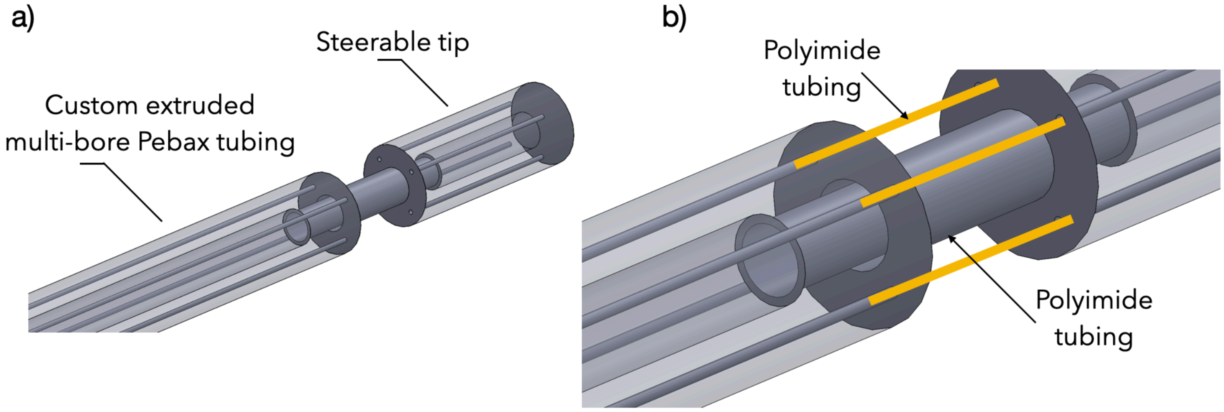

**Figure 4.6**: Illustration of a) connecting the steerable tip to the custom extruded multi-bore tubing, b) inset showing the placement of the polyimide microtubing.

Pebax, a copolymer made up of rigid polyamide and soft polyether, is the gold standard tubing material used to make catheters. Manipulating the ratio of polyamide to polyether defines the material's stiffness or *durometer* for the creation of a large range that spans the flexibility spectrum from very hard and rigid to very soft and flexible, without the need for plasticizers. These unique polymers are biocompatible and maintain the highly desirable combination of the toughness traditionally associated with polyamides and the flexibility/elasticity more often seen with polyethers/polyesters.

While general factors relating to guide catheter selection often come down to personal choice or experience, generally desirable properties in a catheter are a soft atraumatic distal end, a sturdy proximal shaft for support, and multiply graded transitions in rigidity from the proximal to distal ends [130], as illustrated in Fig. 4.7b.

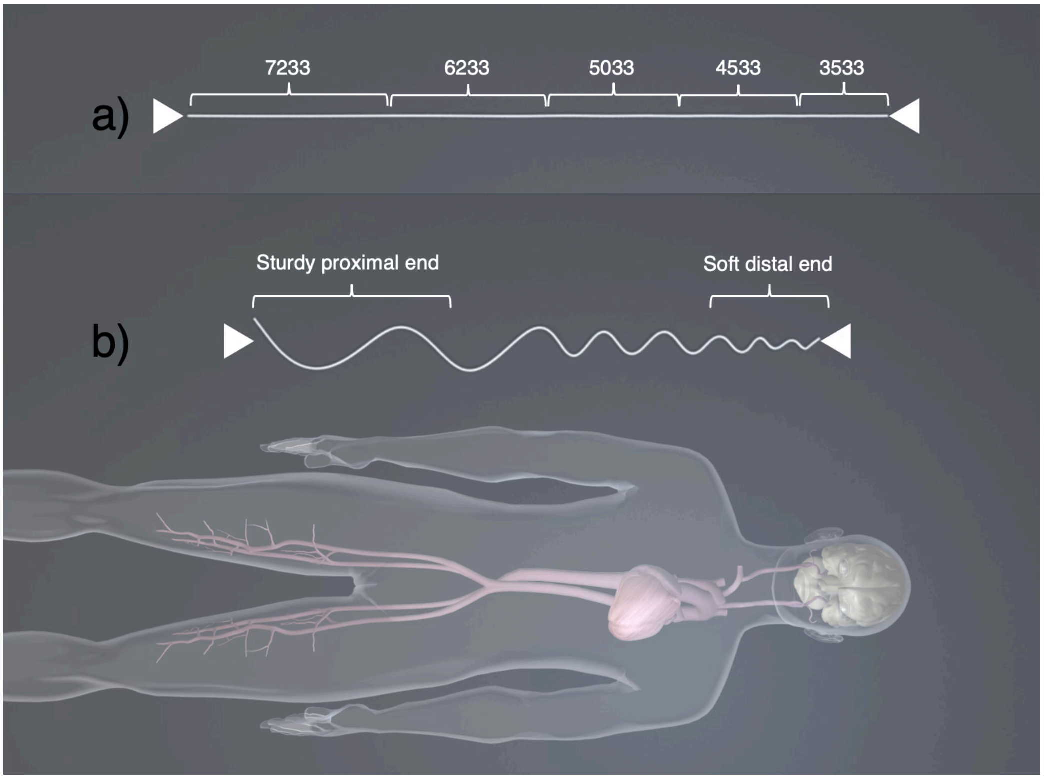

**Figure 4.7**: Illustration of a) catheter in a stretched state, b) compressed at both ends, along with vasculature model to demonstrate transitional stiffness requirements.

In commercially available catheters the lengths and durometer hardness of each section are proprietary. Different systems have been previously proposed in research [131], some including 12 segments [132], others specifically analyzing respective lengths of stiff and soft sections at the tip [133]. However, due to the subjective preferences, anatomical and clinical case variations, no gold standard exists for lengths of the transitional rigidity zones. Using the representative lengths of the internal carotid artery, common carotid artery, brachiocephalic trunk, descending aorta, abdominal aorta, common iliac, and external iliac artery, sections of the catheter were assembled. These were iteratively tested in the ex vivo silicone model and clinician feedback used to modify the lengths to improve pushability while maintaining a soft distal end.

Pebax® 3533 (Nordson Medical, Huntington Beach, CA USA), selected for its softness and flexibility, was reflowed over the polyimide-Dragon-Skin interface to complete the bonding process and formed the distal end. Pebax tube segments of increasing durometer hardness were telescopically connected via standard reflow procedures [134] to obtain full length (160 cm) catheters. The transitional stiffness design was selected to comply with clinical requirements, where lower durometer materials (pebax 3533, pebax 4533) are used closer to the distal end that traverses cerebral arteries, intermediate durometer materials (pebax 5033, pebax 6233) are used in the cardiovascular region, and higher durometer materials (pebax 7233) are used at the proximal end that is near the insertion point at the femoral artery as shown in Fig. 4.7a. The final design had pebax 3533 (10 cm), pebax 4533 (12 cm), pebax 5033 (15 cm), pebax 6233 (23 cm), and pebax 7233 (100 cm).

A reflow procedure involves placing a mandrel in the central lumen and thin wires in the hydraulic channels, both extending from the catheter tip to the proximal end of the catheter. These have to be kept in a stretched state to ensure alignment of the hydraulic channels and maintain structural homogeneity along the length. Heat shrink tubing (FluoroPEELZ, ZEUS, Orangeburg, SC USA) is sleeved over the assembly. Using a controlled heat source, a temperature of 150 °C is applied along the length of the heat shrink tubing. This causes the enclosed pebax tubing with a melting point of 150 °C to flow. This enables bonding the distal end of the catheter to the steerable tip and multiple durometer pebax tubing along the length to achieve transitional stiffness. Once the pebax has been flowed the heat source is withdrawn. Upon cooling, the mandrels and thin wires are removed and the heat shrink tubing peeled away leaving behind a full-length catheter with hydraulic channels in place.

### 4.1.5 Catheter hub at the proximal end

To enable seamless entry of guidewires and coils, a Luer lock catheter hub was attached at the proximal end of the microcatheter to pebax 7233 tubing. The microcatheter hub must be precisely aligned with the proximal end of the microcatheter to ensure the guidewires and coils being inserted are not obstructed.

### 4.1.6 Hydrophillic coating

The assembled micro-catheter comprises of pebax tubing tethered to a hyperelastic material tip. Silicone rubbers and pebax are known to exhibit substantial friction when navigating through highly unstructured environments [117,135]. Commercial catheters have proprietary hydrophillic coatings to reduce the frictional effects during clinical use. In order to reduce the friction effects on the assembled steerable tip micro-catheter, both the inner lumen and outer surface of the catheter were coated with a hydrophilic coating (ON-470, Aculon Inc, San Diego, CA USA) to reduce friction between the micro-catheter and the endothelial walls of the arteries, and between the micro-catheter and devices such as coils passed within the lumen. The external coating was applied via submerged dip coating followed by a sponge constricted wipe along the length of the micro-catheter. The interal coating was applied by first injecting the hydrophillic solution through the catheter hub. To obtain a clear passageway in the central lumen, compressed air was injected at 2 psi for 2 min. This leaves behind a thin layer of the hydrophillic coating on the inner walls of the central lumen.

A fully assembled 160 cm long micro-catheter with a hyperelastic material steerable tip comprising of 4 hydraulic channels for steering is shown in Figure 5.1.

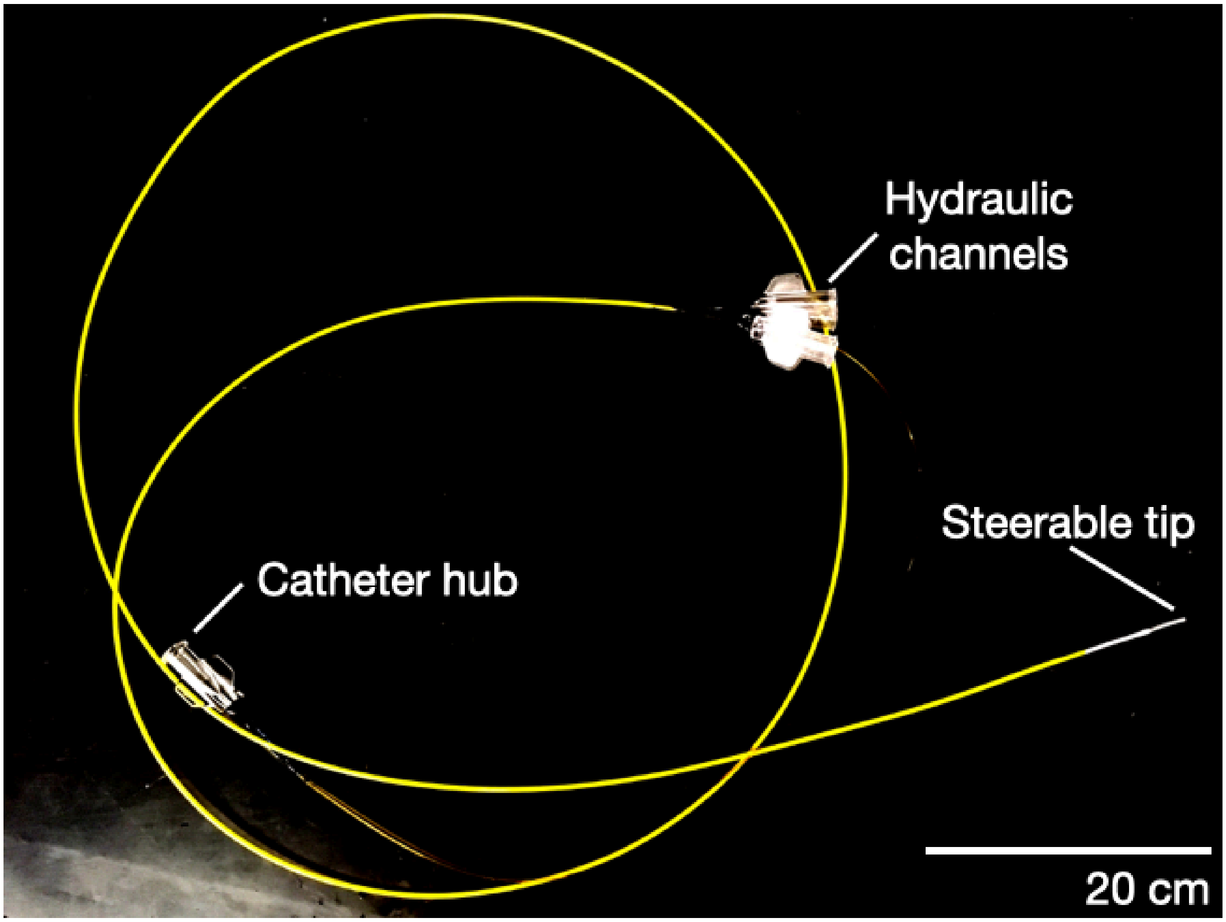

**Figure 4.8**: Image of a fully assembled microcatheter showing the steerable tip, luer connectors for the hydraulic channels and the catheter hub.

## 4.2 Acknowledgements

**Chapter 4** is partially based on the material that is prelminarily accepted in *Science Robotics* (2021), authored by Gopesh Tilvawala, Jessica Wen, David Santiago-Dieppa, Scott Pannell, Bernard Yan, Alexander Norbash, Alexander Khalessi and James Friend. The dissertation author fabricated the steerable tips and assembled the full length catheters.

# Chapter 5

# Material properties, analyses and characterization

## 5.1 Radius and radial location of the hydraulic channels

The inner and outer diameters of the steerable micro-catheter tip are inherently constrained by the diameter of the cerebral arteries [127] and designed to be commensurate with the dimensions of the existing gold standard micro-catheters. However, producing a steerable tip without radial expansion requires a design study focusing upon the hydraulic channel radius, $R_h$ and radial position, $R_{\mathrm{P}}$, of the hydraulic channels as parameters.

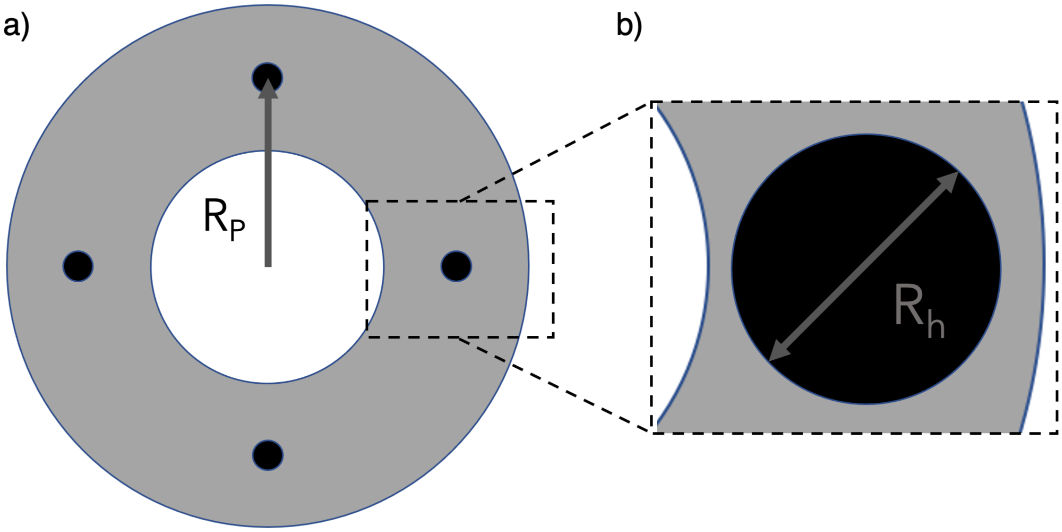

**Figure 5.1**: Illustration of a) Radial position $R_P$, and b) Radius $R_h$ of the hydraulic channel in the micro-catheter.

To assess the influence of varying the radius and radial position of the hydraulic channels on the curvature of the steerable tip, a computational model is required. In order to implement the computational model, the material properties of the hyperelastic polymers used to fabricate the steerable tip need to be established. This first part of this chapter elaborates on a combination of experimental and analytical approaches to obtain the properties of the hyperelastic materials used. The second part of this chapter utilizes the material properties obtained from the first part to implement a computational model and characterize performance of the steerable tip against experimental data.

## 5.2 Hyperelastic material properties

Soft robotics has increasingly gained traction in research and applications over the last decade [84]. This typically involves making actuators of different sizes and configurations using hyperelastic materials, biological materials, or synthetic soft tissues [136] to perform dextrous maneuvers that would otherwise be impossible to conduct using conventional rigid robots. Hyperelastic materials can be manufactured with biocompatibility and a broad range of elastic moduli, failure strains from 200% to over 1000%, surface properties, solvent resistance, and thermal resistance. The material choice depends upon the target application, making it one of the most critical parameters in research design and development. The exponential growth of the soft robotics discipline has been driving a similar growth in the number and variety of hyperelastic materials. Understanding and controlling their behavior in applications is crucial to continue this growth.

In order to design and characterize the behavior of hyperelastic polymer materials, various constitutive models have been developed in the past. Beyond the classic Neo-Hookean model [137], the theory for large deformations of hyperelastic polymers was initiated by the seminal work of Mooney [138] and further elaborated by Rivlin and Saunders [139] which has come to define the Mooney-Rivlin model. Other well-known models include the Ogden [140], Yeoh [141], Blatz-Ko [142], Arruda-Boyce [143], and Gent [144] models. Each of these constitutive models require one or more hyperelastic constants, and finding values for those constants typically require a regimen of experiments.

In the case of the Neo-Hookean model, uniaxial tests are sufficient to fully determine the single constant that it requires to define the material. However, most other models require more than one material constant, and so more experimental tests are required, usually among the following choices: pure shear, equibiaxial tension, planar tension, uniaxial compression, uniaxial tension, and biaxial membrane (bulge) tests [145]. An alternative approach using atomic force microscopy nanoindentation tests was studied by Dimitriadis, *et al.* [146], and subsequently in a few more studies [147–149] where parameters $B_1$ and $B_2$ represent the hyperelastic constants. This approach requires extraction of $B_1$ and $B_2$ using the Young's modulus $E$, however there is no established relationship between $B_1$, $B_2$, $C_1$, and $C_2$.

There has been demonstration of a purely computational approach, without experimental validation, that involves a finite element model (using ABAQUS, Dassault Systèmes, Vélizy-Villacoublay, France) comparing the results obtained from neo-Hookean, Mooney-Rivlin and Yeoh models. Other approaches involve extraction of the storage modulus [147, 150] to iteratively tailor the behavior of PDMS. The tensile and compressive moduli can also be extracted using [151] tensile and compressive testing. In the two-parameter Mooney-Rivlin model, second-order Yeoh and second-order Ogden models, two hyperelastic constants are required. For instance, the first and second hyperelastic constants $C_1$ and $C_2$, also referred to as $C_{10}$ and $C_{01}$, respectively, in the two-parameter Mooney-Rivlin case. While uniaxial tensile tests are sufficient to obtain the first hyperelastic constant $C_1$, biaxial membrane tests are typically necessary to obtain the second hyperelastic constant $C_2$. Various methods and results have been presented to extract the hyperelastic constants [152, 153], however, there are limited benchmark results for the values of hyperelastic constants of common materials such as polydimethylsiloxane (PDMS, Sylgard™ 184, Dow Corning Corp., Midland, MI USA) and many other proprietary hyperelastic materials, such as the platinum-cure silicone Dragon Skin (Smooth-On Corp., Macungie, PA USA).

The first reported values for PDMS were $C_1$ = 34.3 kPa and $C_2$ = 46.9 kPa [154], obtained from uniaxial tensile tests. In a subsequent study, uniaxial experiments were conducted in both axisymmetric and asymmetric fashion, and computational simulations using constitutive models were used to compare against experimental data and establish material constant values for the models [155]. Sasso *et al.* [145] added biaxial tests to uniaxial tests on rubber-like materials and validated the results with finite element analysis (ABAQUS) to determine the values of the material constants for the Neo-Hookean, Arruda-Boyce, Mooney-Rivlin, Ogden, and Yeoh material models. Later, the results of ultra-large deformation bulge tests conducted on PDMS microballoons were compared to finite element analysis (ANSYS, Inc., Canonsburg, PA USA) to obtain $C_1 = 75.5$ kPa and $C_2 = 5.7$ kPa for PDMS [156], remarkably different than Kawamura *et al.* [154]. Uniaxial tensile and compression tests of dielectric elastomers have been used in conjunction with finite element analysis (ABAQUS) to determine the properties of dielectric elastomers [157], though these materials would certainly be expected to exhibit mechanical properties different than pure PDMS.

The overall approach in the literature has been to validate experimentally-obtained results with finite element analysis, and then use the results of this validation to derive the appropriate constants necessary to represent the material with an analytical model. While the use of computation to compare with experimental results and determine the constants for use in an analytically-derived model is convenient, it is tedious and subject to modeling and representation errors made in finite element analysis. Since it is actually possible to directly use the theory in determining the appropriate values for representative constants such as $C_1$ and $C_2$—without having to resort to computational analysis—a viable alternative is to omit the computations. This avoids potential problems arising from approximate representation of the boundary conditions and interfaces present in the system when using finite element analysis. The theoretical approach likewise eliminates the computational costs associated with obtaining and running FEA models.

We consider as an example of this approach the inflation of a small cylindrical disk of hyperelastic media restrained at the periphery. Christensen and Feng [158] long ago combined the theory developed by Mooney [138] and Rivlin [159] with an approximate closed-form solution for the inflation of a thin circular disk to determine the hyperelastic material constants, but there has been no demonstration since to use this theory to produce, for example, the $C_1$ and $C_2$ values for PDMS. In other words, no one has used a purely analytical approach to validate the experimental data. However, over this same time many [145, 155, 160] have used the comparatively painstaking approach of introducing computations to determine these values, as they enable analogous representations of the respective experiments conducted on the hyperelastic materials. In this paper, a non-dimensionalized analytical validation method is provided as a universally applicable approach regardless of the details, provided the minimum criterion for the stretch ratio is met as discussed later.

## 5.3 Biaxial membrane tests

### 5.3.1 Experiments

Different hyperelastic materials will exhibit independent hyperelastic constants. Uniaxial tensile tests are frequently employed to extract the first hyperelastic constant $C_1$, however to obtain the both $C_1$ and $C_2$, a biaxial membrane test is required. Biaxial tests can be conducted in different configurations, either beginning with a 3-dimensional balloon or biaxially inflating an initially flat disk. Making uniform flat, thin films is easier than fabricating 3-dimensional balloons with good surface uniformity out of unknown materials, and so we adopt the biaxially inflated flat disk approach.

Thin films of five different hyperelastic materials, PDMS (Sylgard™184), Dragon-Skin™10, Eco-flex™30, Sorta-clear™40, and Dragon-Skin™mixed with hexane (weight ratio Dragon-Skin A:B:hexane = 1:1:1), were made made by combining the base and curing agent in the manufacturer recommended ratio. Glass slides were coated with release agent (Ease Release™200, Mann Release Technologies, Macungie, PA, USA). All the hyper-elastic polymers were spin-coated at 750 RPM for 60 seconds. Upon curing, the resulting thin films were placed in a custom fixture shown in Fig. 5.2.

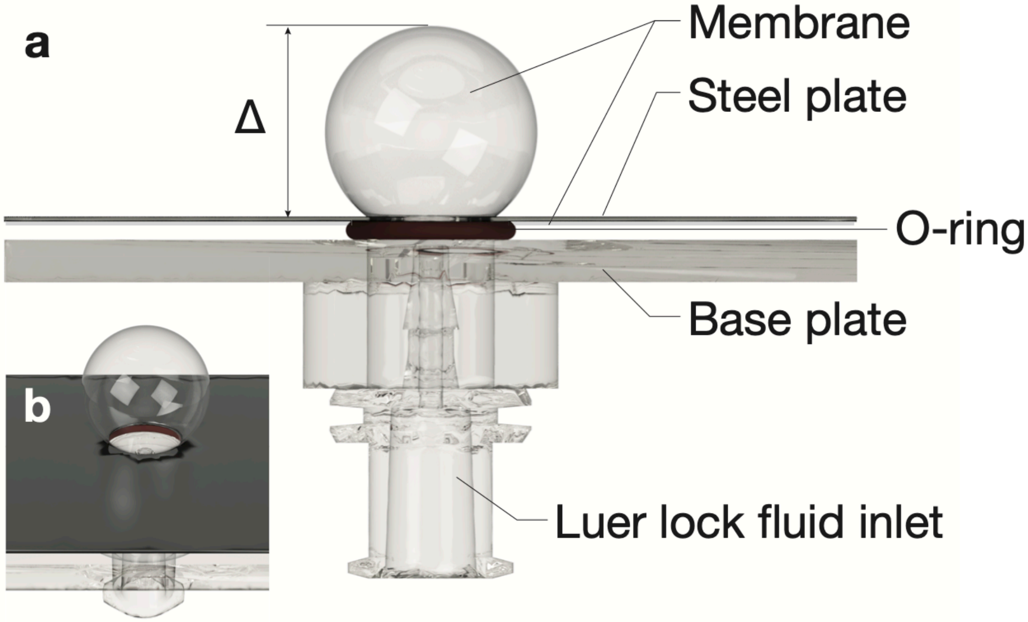

**Figure 5.2**: a) A Luer connector base and steel plate with hole provided to pass the membrane through when inflated, shown (b) from slightly above the horizontal view. The membrane, upon hydraulic inflation from the Luer lock expands as a nearly spherical shape to produce a vertical height above the steel plate of Δ that grows with inflation until membrane failure. The o-ring beneath clamps the membrane in place against the steel plate.

The 3-mm diameter of the circular hole in the base plate and steel plate are similar to eliminate potential lateral stretching. The 4-mm diameter, 0.5-mm thickness O-ring prevents air leakage between the Luer connector base and the steel plate; it is sized to be commensurate with the inner diameter of the steel plate to prevent interference with the membrane expansion from the circular hole. The entire assembly ensures the entire membrane's edge along a circular section is clamped together, leaving a 3 mm radius circular region free to inflate in the middle from an inlet in the substrate to which the membrane and clamp were fastened. Water was introduced through a Luer lock connection into the chamber formed by the clamped membrane and inlet using a high precision microfluidic system (microfluidics control, OB1, Elveflow®, Paris, France). Water was used as the driving fluid to eliminate the potential effects of compressibility associated with pneumatic (air or gas) inflation. The membranes were inflated to failure with pressure increments of 3 kPa/second and filmed using a high-speed camera (Fastcam Mini UX100, Photron, Irvine, CA, USA) combined with a long-distance microscope (CF–1, Infinity, Boulder, CO, USA). The Elveflow system provided the inflation pressure as a function of time to a computer, and was used to trigger the camera to synchronize inflation of the membrane with video recording saved on the same computer. The deformation of the membranes as a function of the inflation pressure was obtained using custom image processing code on MATLAB (MATLAB, Natick, MA, USA).

### 5.3.2 Analytical approach for hyperelastic constants $C_1$ and $C_2$

In order to evaluate the hyperelastic constant values, a relation between the inflation pressure and deformation of the membrane must be established. For a hyperelastic material, the Mooney-Rivlin form of the strain energy function, $W$ is defined as [138, 139]

$$W = C_1 (J_1 - 3) + C_2 (J_2 - 3)\,. \tag{5.1}$$

The constant $C_1$ is proportional to the number of molecular strands per unit volume, and $C_2$ represents additional restraints on the molecular strands; the shear modulus $G = 2(C_1 + C_2)$ while $J_1$ is a measure of the strain defined as [161]

$$J_1 = \lambda_1^2 + \lambda_2^2 + \lambda_3^2, \tag{5.2}$$

and $J_2$ is defined as

$$J_2 = \lambda_1^{-2} + \lambda_2^{-2} + \lambda_3^{-2}\,. \tag{5.3}$$

When an initially flat, circular disc of an elastomeric material with radius $R$ is inflated in a biaxial membrane, or "bulge", test to produce a spherical cap shape, the stretch ratio, $\lambda$, for the maximum displacement of the membrane, $\Delta$, is defined as [158]

$$\lambda = \left(\frac{\frac{\Delta}{R} + \frac{R}{\Delta}}{2}\right) \sin^{-1}\left(\frac{2}{\frac{\Delta}{R} + \frac{R}{\Delta}}\right). \tag{5.4}$$

The relationship between the inflating pressure, $P$, the maximum deformation of the membrane, $\Delta$, and the stretch ratio, $\lambda$ is defined as [158]

$$P = \frac{8C_1H}{R\left(\frac{\Delta}{R} + \frac{R}{\Delta}\right)} \left[\left(1 - \frac{1}{\lambda^6}\right) + \alpha\left(\lambda^2 - \frac{1}{\lambda^4}\right)\right], \tag{5.5}$$

where $H$ is the thickness of the membrane and $\alpha = C_2/C_1$ is the ratio of the hyperelastic constants.

Non-dimensionalizing the pressure and the deformation as

$$\tilde{P} = \frac{RP}{4C_1H} \qquad \text{and} \qquad \tilde{\Delta} = \frac{\Delta}{R_0},$$

where $R_0$ is the initial radius of the membrane, produces

$$\tilde{P} = \frac{2}{\left(\tilde{\Delta} + \frac{1}{\tilde{\Delta}}\right)} \left[\left(1 - \frac{1}{\lambda^6}\right) + \alpha\left(\lambda^2 - \frac{1}{\lambda^4}\right)\right], \tag{5.6}$$

where

$$\lambda = \begin{cases} \frac{\left(\tilde{\Delta} + \frac{1}{\tilde{\Delta}}\right)}{2} \sin^{-1}\left(\frac{2}{\frac{\tilde{\Delta}}{R} + \frac{R}{\tilde{\Delta}}}\right) & \text{if} \quad \tilde{\Delta} \leq 1 \\ \frac{\left(\tilde{\Delta} + \frac{1}{\tilde{\Delta}}\right)}{2} \left(\pi - \sin^{-1}\left(\frac{2}{\frac{\tilde{\Delta}}{R} + \frac{R}{\tilde{\Delta}}}\right)\right) & \text{if} \quad \tilde{\Delta} \geq 1 \end{cases}. \tag{5.7}$$

The dimensionless analytical pressure $\tilde{P}$ was obtained as a function of the stretch ratio $\tilde{\Delta}$ using eqn. (5.6). The experimental $P_{\text{exp}}$ was scaled by $P_R \equiv P_{\text{exp}}\big|_{\Delta=R}$ to produce the nondimensional pressure $\tilde{P}_{\text{exp}} = P_{\text{exp}}/P_R$. The pressure $P_R$ is the pressure required for the membrane to deform an amount equivalent to the initial membrane radius, $\Delta = R$. For an increase $dr$ of the membrane radius, the expansion of the surface requires an amount of work proportional to the pressure. The hyperelastic constants define the factor of proportionality. Least-squares minimization was used to determine the best value of $\alpha$ in minimizing the error between the dimensionless experimental pressure-deformation data and the analytical dimensionless pressure obtained from eqn. (5.6) across the stretch ratios. Since the materials tested in this study have different mechanical properties, the values of $P_R$ and $\alpha$ are different for each material.

After establishing the value of $\alpha$, the dimensional pressure $P$ was evaluated in terms of the dimensional deformation $\Delta$ using eqn. (5.5), where the thickness of the membranes was obtained using a surface profilometer (Dektak 150, Veeco, Plainview, NY, USA). Least-squares minimization was performed to determine the value of $C_1$ that minimizes the error between the dimensional experimental pressure-deformation data and the analytical pressure-deformation obtained from eqn. (5.1). Since the value of $\alpha$ is known from the previous step, $C_2 = C_1\alpha$ can also be determined.

## 5.4 Extraction of hyperelastic constants $C_1$ and $C_2$

The experimental nondimensionalized pressure is plotted with respect to the stretch for two of the materials, Ecoflex™and Sylgard™184 (PDMS), as shown in Fig. 5.3. The remaining materials' plots are provided in Appendix .

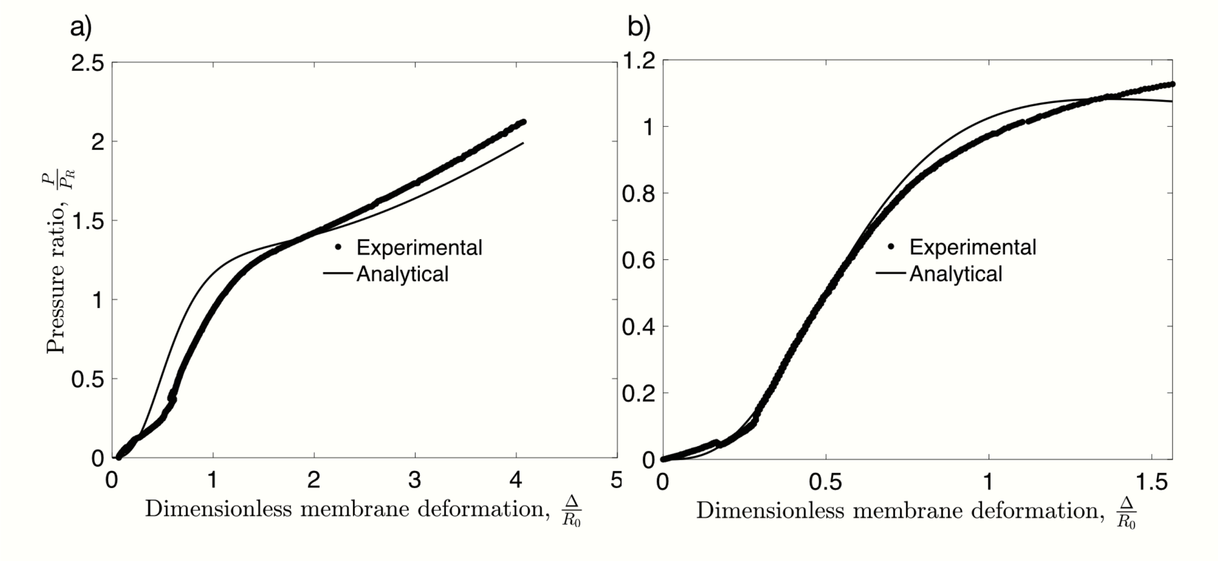

**Figure 5.3**: Dimensionless inflation pressure, $P/P_R$ plotted with respect to the dimensionless deformation of the membrane, $\Delta/R_0$ (x-axis) for a) Ecoflex™ and b) Sylgard™184 (PDMS). Least-squares minimization was used to determine the value of the ratio of the hyperelastic constants, $\alpha$, to directly fit the non-dimensionalized analytical model to the non-dimensionalized experimental data (Ecoflex: $\alpha = 0.1$, $R^2 = 0.91$; PDMS: $\alpha = 0.04$ , $R^2 = 0.99$).

Least squares minimization was used between the experimental data and eqn. (5.3) to determine the value of $\alpha$ and obtain the best-fit plots in Fig. 5.3.

Once the value of ratio of the hyperelastic constants, $\alpha$, is found, the value of $C_1$ may then be found by least squares fitting of eqn. (5.1) to the dimensional pressure-deformation results as illustrated in Fig. 5.4.

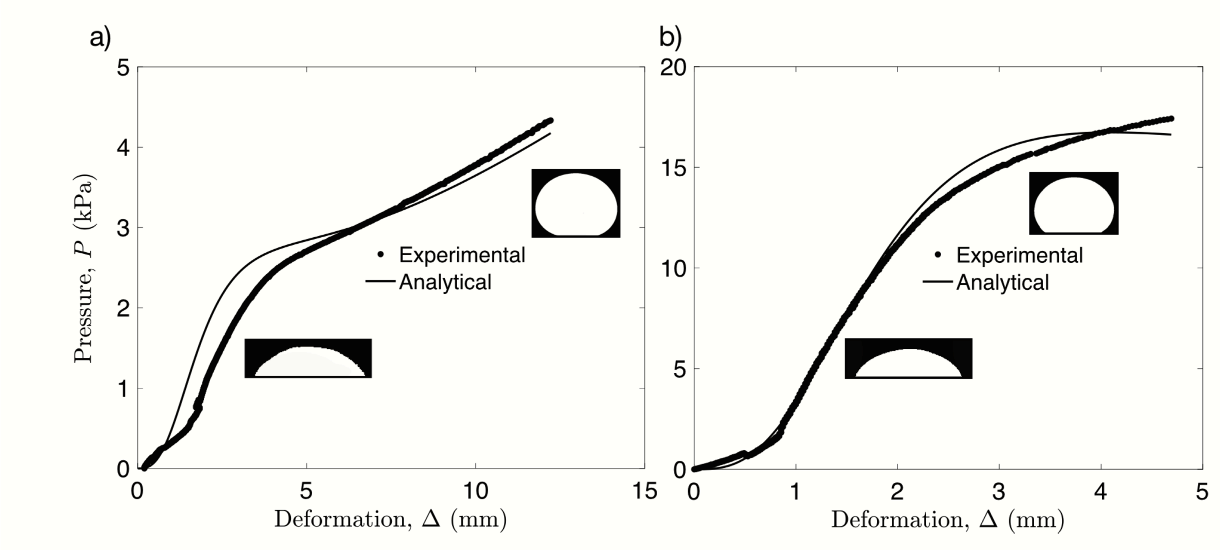

**Figure 5.4**: Dimensional inflation pressure, $P$ as a function of the maximum deformation of the membrane, $\Delta$ for a) Ecoflex™and b) Sylgard™184 (PDMS). Least squares minimization was used to find the best fit for $C_1$ knowing the appropriate value of $\alpha$ from the dimensionless fitting. The values of $C_1$ found from this procedure are provided in Table 5.1 and $R^2 = 0.89$ (Ecoflex) and $R^2 = 0.99$ (PDMS).

Table 5.1 lists all the materials tested in this study, and their respective values of $C_1$ and $C_2$, indicating an ability to test a rather broad range of materials, and likewise notably indicating the remarkable range possible from relatively similar soft polymer materials.

**Table 5.1**: Values of hyperelastic constants $C_1$ and $C_2 = \alpha C_1$ obtained by fitting the two-parameter Mooney-Rivlin model.

| Material | $C_1$ (kPa) | $C_2$ (kPa) |
|---|---|---|
| Dragon-Skin™10 | 210 | 11.7 |
| Ecoflex™ | 75 | 7.5 |
| Sorta-Clear™40 | 830 | 52.3 |
| Sylgard™184 (PDMS) | 270 | 10.8 |
| Dragon-Skin™10 + Hexane at 1:1 weight ratio | 180 | 14.9 |

Table 5.2 shows the values of the hyperelastic constants $C_1$ and $C_2$ obtained for PDMS

compared to previously published results.

**Table 5.2**: Comparison of hyperelastic constant values for Sylgard™184 (PDMS) through the analytical approach and previous studies with biaxial membrane (bulge) tests.

| Sylgard™184 (PDMS) | $C_1$ (kPa) | $C_2$ (kPa) |
|---|---|---|
| Analytical approach | 270.0 | 10.8 |
| Kawamura *et al.* [154] | 34.3 | 46.9 |
| Yoon *et al.* [156] | 75.5 | 5.7 |

## 5.5 Advantages of facile extraction of hyperelastic material properties

Biaxial membrane tests were conducted on five different hyperelastic materials. High resolution imagery, high precision microfluidic systems, and custom MATLAB image processing code were used to extract the inflation pressure as a function of the stretch ratio for the hyperelastic membranes. Each of the membranes were tested to failure to ensure the minimum criterion for the stretch ratio was met. As an example, the two-parameter Mooney-Rivlin model was used in conjunction with an analytical approximation for the large deformation of elastic discs to establish the hyperelastic material properties of five different hyperelastic materials. This approach, although quite simplified, is applicable to a large variety of hyperelastic materials enabling the extraction of their hyperelastic constants through analytical validation of the experimental data. Although the values of the hyperelastic constants in previous studies substantially differ between themselves and the values we found, this can be attributed to different material formulations [150] and curing conditions, particularly temperature and cure duration [151].

However, the facile method presented in this chapter provides a means to easily determine the mechanical characteristics of a hyperelastic material. The method avoids computational analysis which introduces problems of its own, and can be quickly performed so that many material choices can be considered in design. Because it is simple to set up and conduct, the method also enables the reader to quickly produce useful property values from their own materials that may be then used in more accurately modeling their robots and other devices.

## 5.6 Computational model

Unlike the use of saline injection into catheter tips to radially inflate balloons to pin a catheter and deploy coils or expand a stent, avoiding radial expansion of the fluid-filed channels is important in the hydraulically actuated device. This was achieved by carefully designing the placement and size of the fluid channels, and by co-casting concentric layers of a platinum-cure hyperelastic silicone rubber (Dragon-Skin® 10 SLOW, Smooth-On, Inc., Macungie, PA USA).

A finite-element based model was devised (ANSYS, Inc., Canonsburg, PA, USA) to represent the geometrically nonlinear finite deformation of the hyperelastic, nonlinear stiffening material in the catheter tip. Due to the relatively low strains (<10%) induced in this application, a two-parameter Mooney-Rivlin model [138, 139] was used to model the material properties. The Mooney-Rivlin form of the strain energy function is defined as Equation 5.1.

To account for the materials incompressibility:

$$\lambda_1 \lambda_2 \lambda_3 = 1. \tag{5.8}$$

For compatibility with linear elasticity theory, the shear modulus of elasticity $G$,

$$G = 2\left(C_1 + C_2\right). \tag{5.9}$$

For a linearly elastic material,

$$2G(1+\nu)=E, \tag{5.10}$$

where $\nu$ is the Poisson ratio, and $E$ is Youngs modulus. For isotropic materials, the principal Cauchy stresses are coaxial with the principal stretches and are given by,

$$\sigma_1-\sigma_3=\lambda_1\frac{\partial W}{\partial\lambda_1}-\lambda_3\frac{\partial W}{\partial\lambda_3}, \tag{5.11}$$

$$\sigma_2-\sigma_3=\lambda_2\frac{\partial W}{\partial\lambda_2}-\lambda_3\frac{\partial W}{\partial\lambda_3}. \tag{5.12}$$

Substituting the incompressibility function, equation 5.8 into equation 5.11 and 5.12, we obtain:

$$\sigma_1-\sigma_3=2C_1\left(\lambda_1^2-\lambda_3^2\right)-2C_2\left(\lambda_1^{-2}-\lambda_3^2\right), \tag{5.13}$$

$$\sigma_2-\sigma_3=2C_1\left(\lambda_2^2-\lambda_3^2\right)-2C_2\left(\lambda_2^{-2}-\lambda_3^2\right). \tag{5.14}$$

During static conditions,

$$\sigma_1=\sigma_{rr}=-p, \tag{5.15}$$

$$\sigma_2=\sigma_{\theta\theta}=\frac{pR_h}{t}, \tag{5.16}$$

$$\sigma_3=\sigma_{zz}=\frac{pR_h}{2t}, \tag{5.17}$$

where $t$ is the wall thickness. Neglecting the body forces and shear stresses, the equations for static equilibrium can be reduced to:

$$\frac{\partial \sigma_{rr}}{\partial R_h} + \frac{1}{R_h}\left(\sigma_{rr} - \sigma_{\theta\theta}\right) = 0\,, \tag{5.18}$$

$$\frac{\partial \sigma_{zz}}{\partial Z} = 0\,. \tag{5.19}$$

Noting, $\sigma_{rr}\,(=\sigma_1)$ and $\sigma_{\theta\theta}\,(=\sigma_2)$, using equations 5.13 and 5.14, the principal stress relations for an isotropic, hyperelastic Mooney-Rivlin material $\sigma_{\theta\theta}$ can be eliminated and then employing the incompressibility function (equation 5.8, the following equation is obtained for $\sigma_{rr}$:

$$\frac{\partial\left(R_h \sigma_{rr}\right)}{\partial r} + \frac{r}{R_h}\left\{\sigma_{rr} + 2\left(C_1 + C_2\right)\left[\left(\frac{R_h}{r}\right)^2 - \left(\frac{r}{R_h}\right)^2\right]\right\} = 0\,. \tag{5.20}$$

Hyperelastic constants $C_1$ and $C_2$ necessary for the model were experimentally extracted by conducting biaxial membrane tests on thin films [4]. The experimental stress-strain data for the hyperelastic materials were input in the computational model. A manual element control with a reduced brick integration scheme and a linear tetrahedron mesh with adaptive sizing was utilized. The reduced scheme prevents a shape function locking problem that commonly arises for computational models of hyperelastic materials. Boundary conditions include a fixed face at the beginning of the steerable tip and a normal pressure applied within the hydraulic channel.

Applying the boundary conditions, $\sigma_{rr}|_{r=r_o} = 0$, $\sigma_{rr}|_{r=r_i} = -p$ to equation 5.20, we get the pressure-radius relation:

$$p = \left[f\left(\frac{r_1^2}{R_{h_1}^2}\right) - f\left(\frac{r_i^2}{R_{h_i}^2}\right)\right]\left(C_1 + C_2\right) \tag{5.21}$$

Substituting the geometric relationships for the hydraulic channels enclosed within the hypereleastic material initial radius $R_h$ and deformed radius $R_h + R_E$, where $R_E$ is the radial displacement of the inner surface of the hydraulic channel, gives:

$$\frac{p}{C_1 + C_2} = \left[ f\left( \frac{(1 + t/R_h)^2}{(1 + t/R_h)^2 - 1 + (1 + R_E/R_h)^2} \right) - f\left( \frac{1}{(1 + R_E/R_h)^2} \right) \right] \tag{5.22}$$

To account for the changes in size and aspect ratio of the elements during the finite deformation of the tip structure, a nonlinear adaptive deformation (NLAD) scheme [162] was used to ensure convergence with the hyperelastic material. Figure 5.5 shows the boundary conditions, deformed tip and the pressurized channel to demonstrate the computational model implemented.

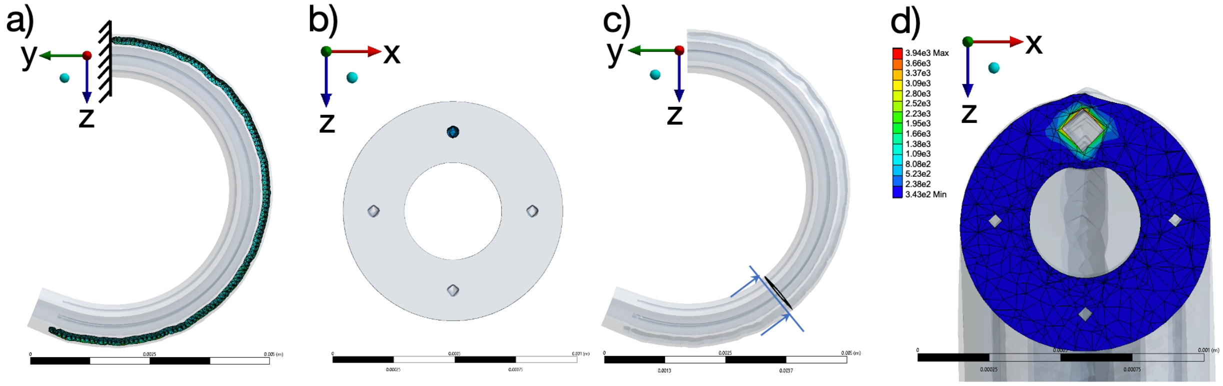

**Figure 5.5**: Result showing the a) pressurized steerable tip with a fixed support and b) cross-section of the tip illustrating the pressurized channel c) illustration of the cross-sectional plane along the length at which the radial pressure is shown in d) achieving an acute at a pressure just under 400 kPa.

## 5.7 Experimental extraction of curvature and radial expansion

The performance of the steerable tip was quantified through measurements of the tip curvature versus input pressure over time. Combining imagery (FASTCAM Mini AX200, Photron, San Diego, CA USA) with a high precision microfluidics system (OB-1, Elveflow®, Paris, France), and custom image post-processing (MATLAB R2020a, MathWorks, Natick, MA, USA), the curvature of the tip was obtained as a function of the input pressure as shown in Fig. 5.6. The experiment was designed such that the Photron camera triggers recording in synchrony with the input pressure from the Elveflow system. The imposed pressure and camera frame rate were set to be equal at 50 Hz.

## 5.8 Comparison of experimental and computational results

Using a computational model, the radii for hydraulic input were varied from 25 $\mu$m to 100 $\mu$m while maintaining a fixed radial position (325 $\mu$m from the center). The position of the hydraulic channel was varied from 260 $\mu$m to 390 $\mu$m from the center of the lumen, while maintaining a fixed channel radius of 50 $\mu$m.

The number of channels also impacts the device mechanics, as a greater number of small channels could produce an improved ability to steer, but the significant drawback in introducing more than three to four channels is the rapid increase in complexity of the tip-to-catheter and catheter-to-hand controller interfaces. Consequently, we limited our study to four channels, and noted that three or fewer channels produce similar results, albeit with reduced functionality with two or fewer channels. Furthermore, the computational expense of accurately computing the nonlinear finite deformation of a non-linearly (stiffening) elastic media in a structure with a length:width aspect ratio of 1:1000, together with practical fabrication limitations imposed by the small scale and intrinsic challenges in making such structures, limited our choices for the channel radius, $R$, and the radial position of the channel, $R_P$ to three values each. Even so, it is apparent from Fig. 5.6b,c (and Fig. 5.7) that the range of choices considered have a significant effect on the performance of the device.

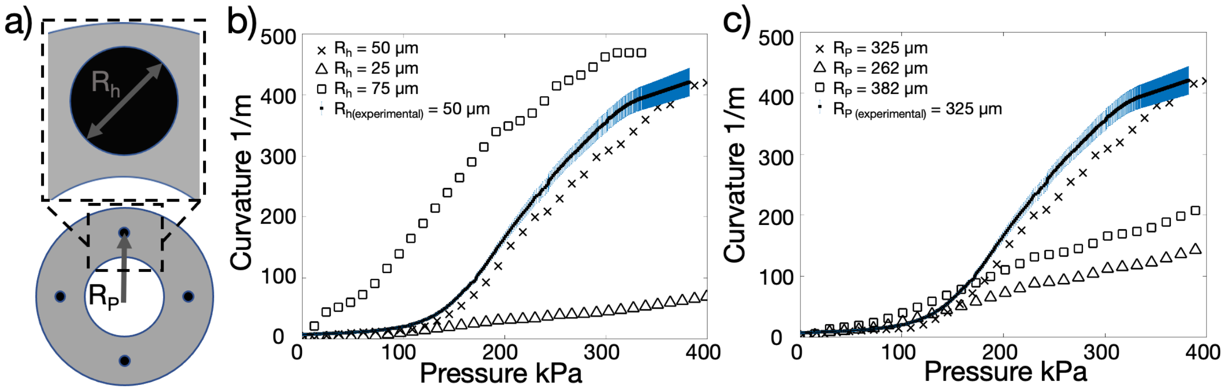

**Figure 5.6**: Design parameters of the steerable tip, and the consequent curvature as a function of input pressure. Nonlinear finite deformable structural mechanics analysis was used to compute the relationship between the tip curvature and input pressure for three values of a) the channel radius, $R$, and the channels' radial position, $R_{\mathrm{P}}$. The b,c) curvature of the tip as a function of the input pressure produces significantly different computational results for the b) radius $R$ with the radial position $R_{\mathrm{P}}$ at $R_{\mathrm{P}} = 325\ \mu$m, and c) radial channel position $R_{\mathrm{P}}$ for a channel radius $R = 50\ \mu$m. The computed results are similar to (solid line in b,c) experimental results obtained with $R = 50\ \mu$m and $R_{\mathrm{P}} = 325\ \mu$m. The experimental results are averaged for four channels, blue lines indicate error bars.

Further, Fig. 5.6b,c: solid lines) plots the tip's curvature versus input pressure using image capture and post-processing. The pressure required to achieve a curvature of 400 1/m (180° total bend, forming a "C" shape) is 350 kPa, significantly lower than traditional balloon catheters (600 kPa) [163] for stent deployment. Positioning the radius away from the midpoint of the wall thickness results in inadequate curvature at higher input pressures (Figure 5.6 b). The 50 $\mu$m diameter channels exhibit 10% strain to achieve a 180° bend. The materials used have a strain at failure >350% [4] at pressures four times that required to achieve 10% strain. In the inadvertent case of over-pressurizing the hydraulic channel, the steerable tip loops on itself at pressures higher than 350 kPa, and will rupture at a pressure of 1200 kPa thus providing a safety factor ≈4.

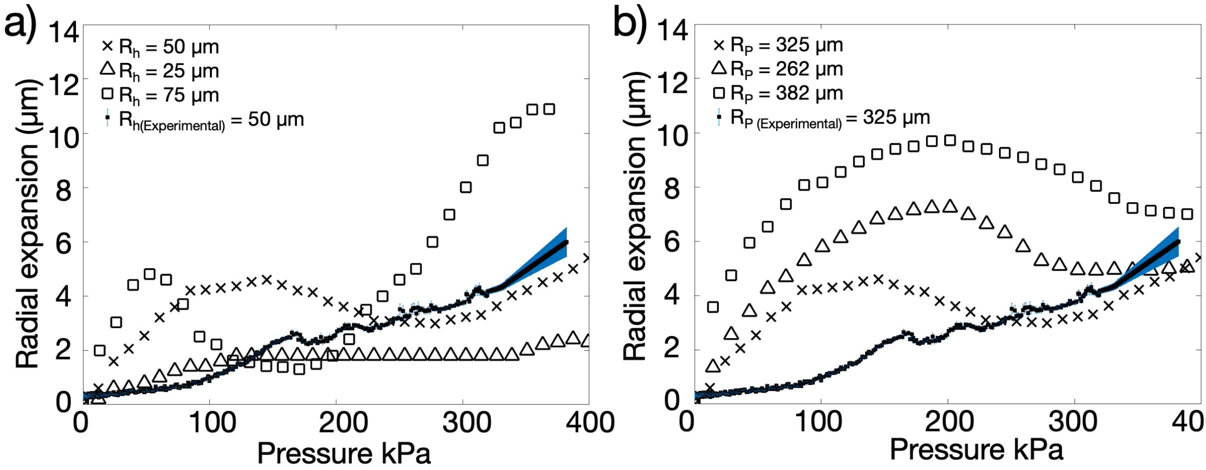

**Figure 5.7**: The hydraulic channels' position and radius affects the relationship between the tip's radial expansion and the input pressure. Computed radial expansion of the steerable tip at its outer surface as a function of a) channel radius $R$ with $R_P = 325\ \mu$m, and b) channel radial position $R_P$ with channel radius $R = 50\ \mu$m, compared to experimental results for a tip with $R = 50\ \mu$m and $R_P = 325\ \mu$m. The experimental results are averaged for four channels, blue lines indicate error bars.

While a smaller channel radius of $R = 25\ \mu$m, for example, helps to reduce radial expansion (Fig. 5.7 a), the bending curvature is significantly reduced for the same input pressure (Fig. 5.6 a). A larger radius, $R = 75\ \mu$m, produces greater curvatures at relatively lower input pressures (Fig. 5.6 a), although radial expansion is also significantly greater (Fig. 5.6 a). The large mismatch in the simulated results for the radial expansion indicates that, initially, the hydraulic channels rapidly expand and reach a maximum saturation point where the concentric layers prevent further expansion. As the hydraulic channels elongate, the radial expansion reduces to compensate. Although the experimental results demonstrate a similar trend, it is more subtle than the simulated results. While the concentric layers prevent excess radial expansion at the required curvatures, the elongation during the experiment does not cause a reduction in the hydraulic channel radius.

**Tailoring the tip's construction to further reduce radial expansion**

The innermost and outermost surfaces are made with the hyperelastic polymer, while the region enclosed by these surfaces is formed from a relatively softer 1:1 mixture by weight of the hyperelastic polymer with hexane (CAS 110–54–3, 95% anhydrous hexane, SigmaAldrich, St. Louis, MO USA).

The purpose of this layering and the placement and sizing of the fluid channels is to promote axial deformation while minimizing radial expansion. The key is to observe that the layering of different hyperelastic materials induces stress-stiffening [4]. Consequently, the introduction of a pressure in one of the channels produces radial, axial, and azimuthal stress, and as these values increase, the rate of strain increase gradually falls. The radial strain, over the relatively short length scale of the wall thickness of the catheter tip, quickly reaches the stiffening portion of the hyperelastic stress-strain response.

However, because the tip is ~100 times longer than its radius, the axial deformation is likewise ~100 times greater than the radial deformation for the same strain value. The axial deformation is therefore far greater, producing ample bending of the tip with negligible radial expansion. This material choice is contrary to the choice of strain-softening hyperelastic media typical in balloons. Further, the relative rigidity of the polymer without hexane treatment serves as a constraint to radial expansion, squeezing the relatively soft hexane-treated polymer within to axially exude from the channel pressure. Catheter tips made without layering exhibit significantly larger radial expansion (Fig. 5.5).

### 5.8.1 One-to-one motion of the catheter

During surgical intervention, tip deflection requires timely response to the hand-motions of the interventionist. The response time, $\tau$ can be analytically estimated as $P = 1 - \exp\frac{-t}{\tau}$ [164]. The hydraulic channel is a closed system between the input and the hyperelastic material tip. The transient response of the tip deflection to step changes in input pressure shows $\tau < 1$s (Figure 5.8), despite 1.6 m of connecting 50 $\mu$m diameter microtubing between the two. Figure 5.8 shows the deflection of the steerable tip with respect to the input pressure. The input pressure $P$ was scaled by the maximum pressure $P_{max}$ and the bending angle $\theta$ by the maximum bending $\theta_{max}$.

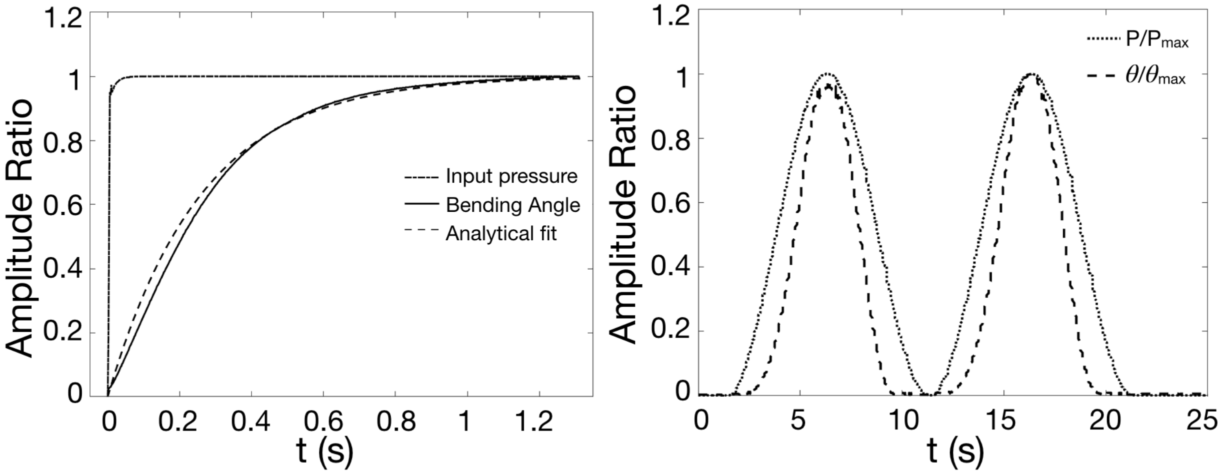

**Figure 5.8**: The distal catheter tip's deflection in response to a commanded input pressure at the proximal end of the 1.6 m-long catheter. When a step increase in the pressure is imposed at the proximal end of the catheter, the distal tip deflects to 95% of its final response within 1 s to achieve a bending angle of 180°. When a sinusoidal input pressure is gradually imposed, the steerable tip deflects concurrently.

## 5.9 Acknowledgements

**Chapter 5,** the first part of this chapter is based on the material published in *Soft Robotics* (2020) authored by Gopesh Tilvawala and James Friend [4]. The dissertation author was the primary researcher and author of this paper. The second part of this chapter is partially based on material that is prelminarily accepted in *Science Robotics* (2018), authored by Gopesh Tilvawala, Jessica Wen, David Santiago-Dieppa, Scott Pannell, Bernard Yan, Alexander Norbash, Alexander Khalessi and James Friend. The dissertation author worked on this

chapter in entirety.

# Chapter 6

# Representative ex vivo model, testing and results

## 6.1 A representative *ex vivo* model of the vasculature with realistic cardiac flow

Performance of the steerable catheter was assessed and iteratively improved through testing by clinical practitioners in *ex vivo* silicone models representative of the human vasculature, similar to models used to test commercially available catheters [165–167]. A single vasculature model of vessels from the femoral artery to the internal carotid artery (ICA), including the aortic arch, was constructed. Anonymized CT-angiogram DICOM images from a patient with representative vasculature tortuosity for the mean age group treated for intracranial aneurysms were segmented using 3DSlicer [168] to obtain the vasculature in a format suitable for 3D printing, as shown in Figure 6.1. The image segmentation to select the relevant blood vessels was conducted using the region based watershed transformation [169].

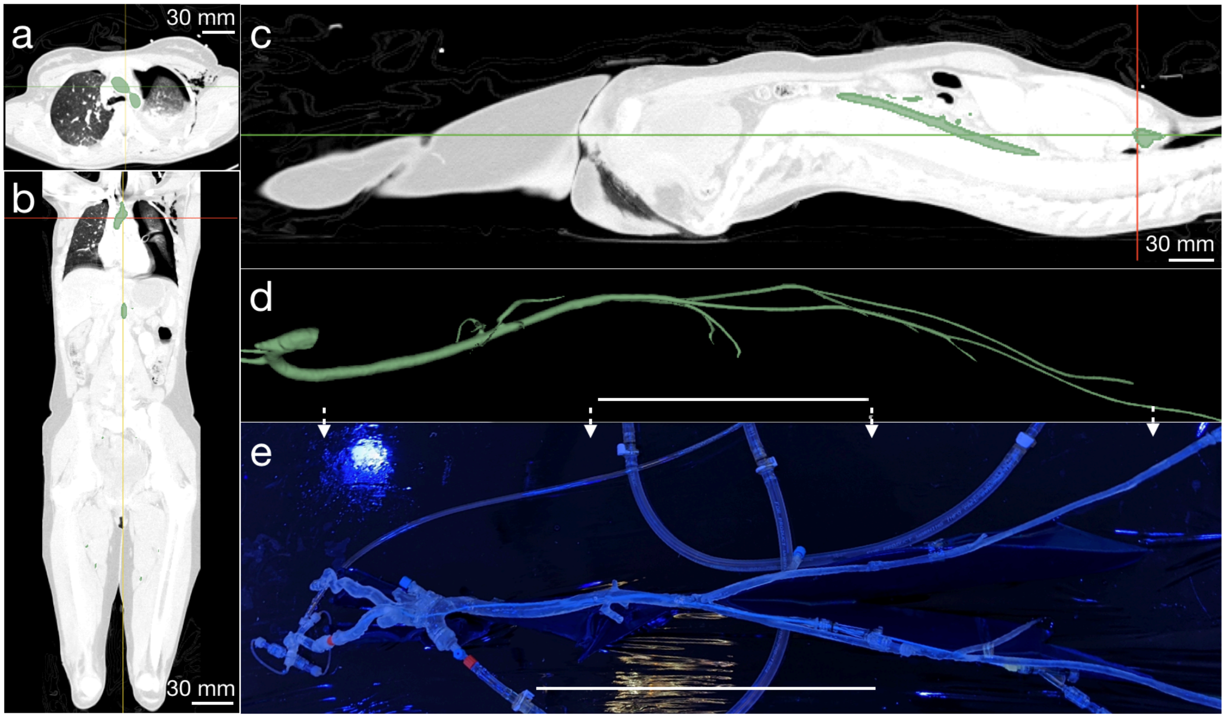

**Figure 6.1**: Fabrication of an *ex vivo* silicone model from anonymized patient data. a) Axial, b) sagittal, and c) coronal views of CT angiogram images with vascular segmentation for a single slice shown in green. This process produces a d) complete vascular model from the femoral artery to the aortic arch, including principal vascular branches, in particular the carotid arteries to the cerebrovasculature. Through 3D printing and lost ABS casting as detailed in the text, e) a functional, fluid-tight vascular model may be produced. (d,e) Scale bar = 25 cm.

The segmented images were converted to .stl format to enable 3D printing. A model of the vascular structure was 3D printed with ABS (Acrylonitrile Butadiene Styrene) plastic. Since 3D prints comprise of layers which contribute to significant surface roughness, the surface of the 3D printed models was treated with an acetone vapor bath at 40°C for 30 minutes to obtain a smooth surface finish. The scale of the vascular model is larger than conventionally available 3D printer beds, the model was printed in three separate parts. The parts were joined using acetone solution to form a homogeneous bond at the joints. The smoothed 3D model was dip-coated with an aqueous sugar solution (10% by weight). The sugar solution prevents reaction between the translucent polymer and the smoothed ABS that can lead to significant clouding of the ex vivo model. After drying the aqueous solutions, eight layers of a translucent hyperelastic polymer (SORTA-clear® 40, Smooth-On, Inc., Macungie, PA USA), were applied, allowing 48 hours cure time for each layer. The polymer coated model was submerged in an acetone bath for 72 hours to dissolve the ABS, leaving behind the *ex vivo* silicone model. Aqueous solution was run through the model to clear out any remaining sugar deposits remaining on the interior surface. The walls of the silicone model were rendered hydrophilic with a surface coating (ON–470, Aculon Inc, San Diego, CA USA) to reduce the friction between the silicone model and the outer walls of the catheter and mimic the lubricity of endothelial cells in the human vasculature.

A separate silicone phantom from the internal carotid to the cerebral vessels including the aneurysm was fabricated using the same approach; the aneurysm presented here was selected to represent a challenging geometry at the posterior communicating artery (PCOM) requiring acute angle turns.

Insert image of the cerebral blood vessels CT-A and silicone model.

### 6.1.1 Pulsatile flow using a blood flow analog

The *ex vivo* silicone model was connected to an external flow system (FlowTek 125, UnitedBiologics, Santa Ana, CA USA) to generate pulsatile flow and pump a physician verified blood analog (SLIP solution, UnitedBiologics, Santa Ana, CA, USA) to provide a representative validation model to mimic blood pumped by the heart. The pulsatile flow pump enables control of the pulse rate and flow rate. An immersion heater was used to maintain the blood flow analog at a temperature of 37°C (98.6°C) representative of the clinical environment. Since the silicone model is an isolated segmentation of the endovascular coiling arterial route, the flow rate through the aneurysm location was calibrated to achieve 50 ml/min prescribed by standard measurements of flow rates through cerebral arteries [170]. The temperature of the blood analog was maintained at 37°C (98.6°F) using an immersion heater with thermostat to represent normal temperature of blood in vessels.

### 6.1.2 Flow rate calibration

The pressure at the inlet of the internal carotid artery and exit of the posterior communicating artery (PCOM) (as shown in Fig. 6.2) was measured using a high resolution pressure sensor (2SMPP-03, OMRON, Kyoto, Japan) [5] at different flow rates generated by the pulsatile flow pump. The pressure difference was used to compute the flow rate assuming laminar flow and therefore the validity of the Hagen-Poiseuille equation to represent the pressure drop-flow rate relationship. The Reynolds number is ~50–100, justifying the laminar flow assumption.

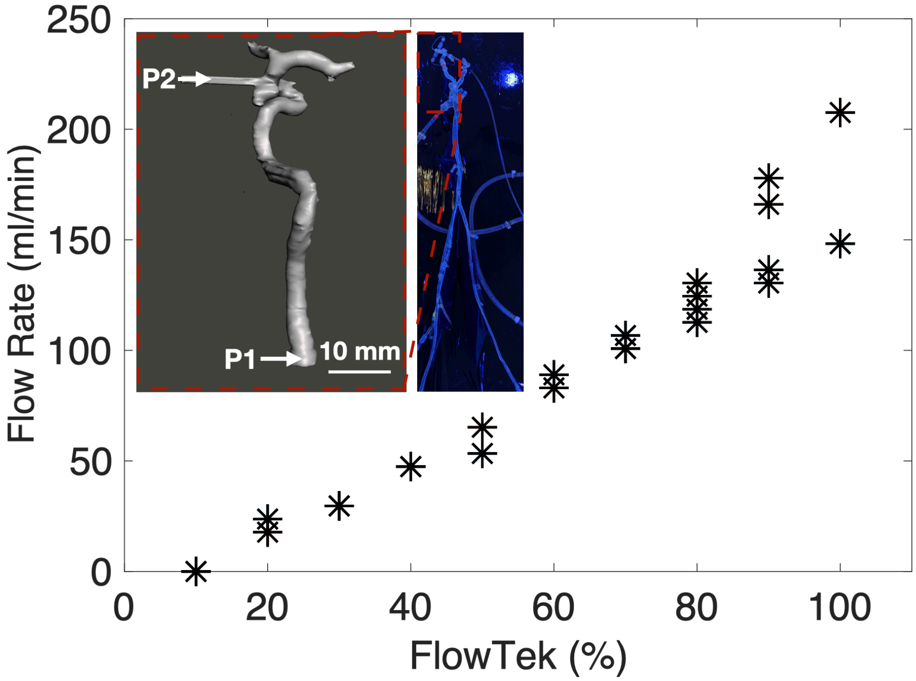

**Figure 6.2**: Calibration of the flow rate through the PCOM aneurysm in the *ex vivo* silicone model. Inset: illustration of the pressure measurement points in the ex vivo model. Point P1 is at the inlet of the internal carotid artery and point P2 is at the exit of the posterior communicating artery. The pressure drop between these two points, together with the observation that the flow in the interceding artery is laminar, allows us to compute the flow rate via the Hagen-Poiseuille equation. This computed flow rate delivered through the aneurysm depends almost linearly upon the commanded flow rate to the pump.

### 6.1.3 Neuroendovascular surgical set up commensurate with clinical procedures

Using a female luer connector at the right femoral artery of the silicone model as the access point, a guide catheter (ENVOY® XB 6F, Codman & Shurtleff Inc, Raynham, MA USA) was inserted into the silicone model, with its tip parked at the middle of the internal carotid artery (ICA). A rotating hemostatic valve (RHV) was connected to the Envoy hub and the steerable micro-catheter was advanced until the distal end of the Envoy. A second RHV was connected to the hub of the steerable catheter. Both the RHV's were connected to standard saline at a pressure of 300 mmHg to set up the flush lines in line with standard endovascular neurosurgical protocols [171]. The second RHV was used as the insertion point for the microguidewire (Synchro$^2$ ™, Stryker Neurovascular, Kalamazoo, MI USA). Upon reaching the distal end, the guidewire was retrieved and the steerable micro-catheter advanced leading the way to the aneurysm. Unlike conventional endovascular neurosurgery, once the guidewire was used to reach the distal end of the guide catheter, the guidewire was retrieved and hydraulic actuation of the steerable catheter engaged to direct the distal end of the steerable through the middle carotid artery and access the posterior communicating artery. Active steering was used to place the distal end of the steerable tip into the dome of the aneurysm. Once the tip was positioned in the geometrical center of the aneurysm, the hydraulic channel was locked using a one way stopcock to hold the steerable tip in a fixed position. Detachable coils (FC-6-20-3D, AXIUM™ PRIME detachable coils (frame), Medtronic, Irvine, CA USA) were introduced through the steerable micro-catheter's hub and deployed into the dome of the aneurysm.

## 6.2 Testing *in vivo* in porcine

This study was approved by the University of California San Diego Animal Care and Use Committee. A skeletally mature (47 kg) female pig underwent general endotracheal anesthesia. Cardiorespiratory monitoring was performed throughout the procedure under the supervision of a veterinary technician.

Referring to Fig. 6.3, after surgical exposure, A 6-F sheath was placed in the left femoral artery using the modified Seldinger technique [172]. Under roadmap fluoroscopic guidance (Siemens Artis Zeego, PA, USA), a 5-F guide catheter (Guider Softip$^{\text{TM}}$ XF, Boston Scientific, MA, USA) was placed in the right common carotid artery (CCA) over a 0.035 in wire (Glidewire, Terumo, CA, USA). A straight 0.014 in micro-guidewire (Synchro$^2$ ™, Stryker Neurovascular, Kalamazoo, MI, USA) was inserted into the steerable micro-catheter. The micro-guidewire and micro-catheter were advanced to the distal end of the guide catheter in tandem. The 6-F sheath, 5-F guide catheter, and steerable micro-catheter were flushed with continuously running saline at a pressure of 300 mmHg using standard rotating hemostatic valves (Touhy-Borst Y-connector). The micro-guidewire was retrieved, the hydraulic steering engaged, and the steerable micro-catheter was advanced to perform *guidewire free* navigation to access the ascending pharyngeal artery. Hydraulic actuation was disengaged, returning the tip to its native, straight orientation. The steerable micro-catheter was further advanced and hydraulic actuation, applied by pressurizing saline through a 1 ml syringe was then engaged to direct the distal end into the parotid artery. The catheter was locked in this curvature and position using a one-way stop-cock and platinum coils (FC-6-20-3D, AXIUM™ PRIME) were deployed via the hub of the micro-catheter.

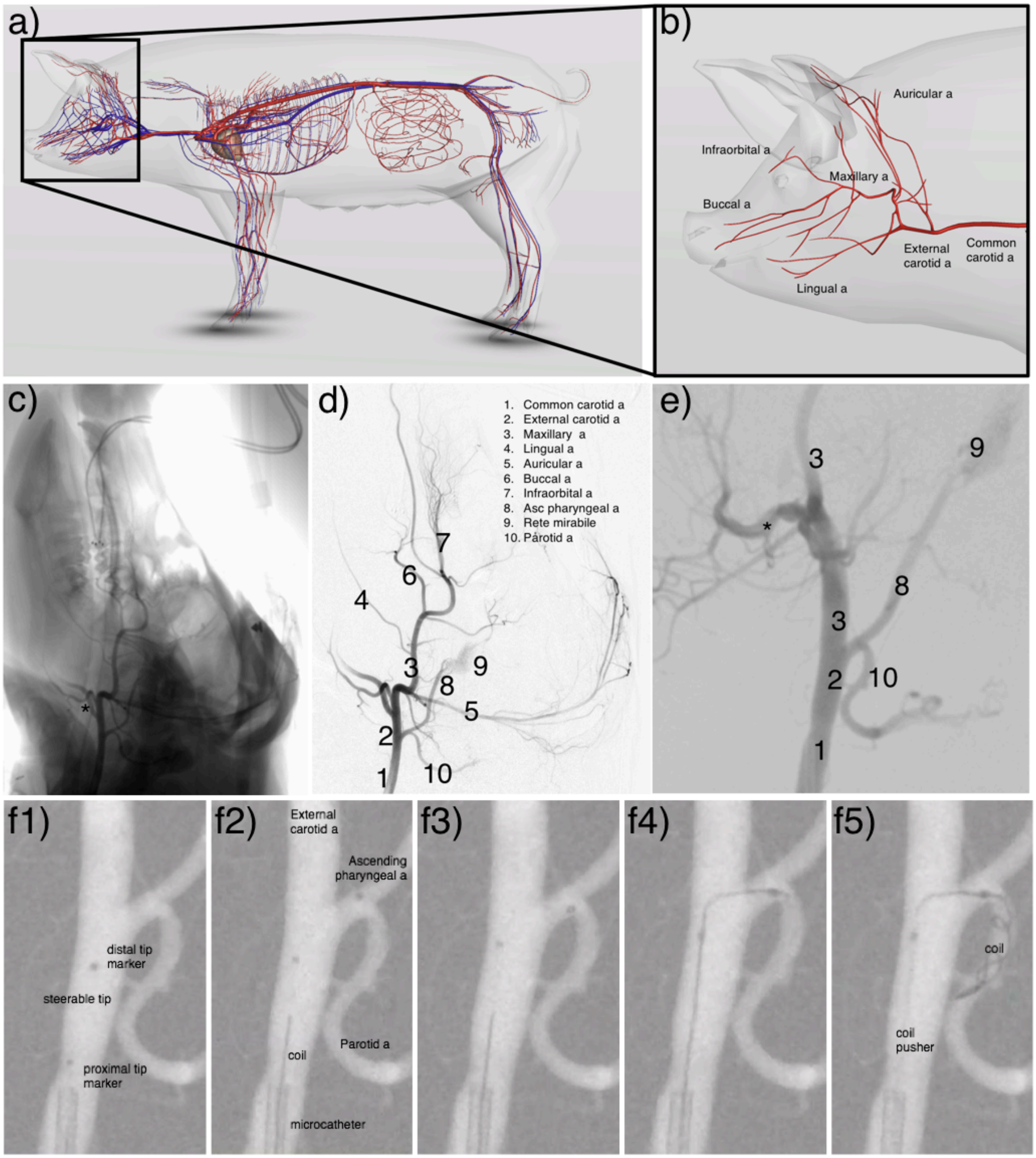

**Figure 6.3**: Animal study: Illustration of porcine (3D Pig Anatomy Software by Biosphera) a) arteries and b) cerebral arteries for reference. (c) Anteroposterior (AP) diagnostic subtraction angiogram of the right CCA. (d) Spot AP roadmap fluoroscopic image of the right CCA. enlarged in (e). (f1) Position one, showing the steerable microcatheter prior to introduction of a hydraulic load. (f2) Position two, showing the micro-catheter after hydraulically steering the tip to access the ascending pharyngeal artery from the external carotid artery. (f3-4) Position three, showing the hydraulic steering of the catheter tip to access the parotid artery from the ascending pharyngeal artery. (f5) Coils deployed in the parotid artery from the stabilized catheter tip.

## 6.3 Discussion

A micro-catheter with a soft tip that can be controllably directed in an artery during endovascular coil embolization could decrease procedure time and reduce the failure rate of these procedures. Comparative studies between steerable and non-steerable catheters have demonstrated significant reductions in procedure time and improvements in patient safety [121–123]. Steerable catheters are known to enable better positioning of sophisticated implants [124, 125] and successful treatment in patients who would otherwise be precluded from endovascular treatment with a standard non-steerable catheter [62, 173].

The work described here demonstrates the use and efficacy of a hydraulically actuated soft polymer tip that can be steered and locked in a desired position at the distal end of a micro-catheter *in vivo*. A micro-catheter with a steerable tip would allow safer and quicker navigation through tortuous anatomy, improved access of a more desirable target location relative to the aneurysm dome, and coil deployment with a more stable platform. Due to their inherent rigidity and size, traditional robotic tools would not be able to achieve this within blood vessels at the millimeter scale. Likewise, a purely soft material approach would present serious technical challenges with regard to pushability *in vivo*. Here we leverage microfabricated soft robotic actuators with engineered hyperelastic materials to assemble full length catheters with transitionally variable stiffness from the distal to proximal end. This device further enables the deployment of devices such as stents and flow diversion pipelines in challenging anatomical configurations. Although balloon assisted coiling [174] has been used to mechanically assist in orienting a catheter tip in endovascular neurointervention procedures, this method does not provide control over catheter tip orientation within the aneurysm dome, and due to anatomical size constraints, cannot be used in smaller blood vessels.

In the present work, a steerable tip micro-catheter at the submillimeter length scales commensurate with endovascular neurosurgical catheters was fabricated, characterized, and tested in *ex vivo* silicone models representative of the human vasculature. Feedback from practicing neurointerventionists was incorporated to iteratively improve device performance before conducting an *in vivo* trial in live porcine. Based on the resulting data, the technology demonstrates promise as a viable approach to augment the function of existing microcatheters in treatment of vascular injuries. Likewise, the present work demonstrates that novel fabrication approaches in combination with bioinspired motion can be used to pave the way for a new set of tools for conducting autonomous vascular surgery, for instance, to specific locations inside the heart [118].

Although the present work focuses on treatment of aneurysms in cerebral blood vessels, the described steerable device can be extended to treat or diagnose a broader set of pathologies through application to other procedures that also require fine, dexterous manipulations. Similar challenges of small vessel diameter and complex vessel tortuosity in addition to vessel occlusions are encountered in interventional cardiology and general vascular surgery. Non-vascular applications include pulmonary nodule biopsy during bronchoscopy in interventional pulmonology, where an analogous branching airway system with progressively smaller branches also involves a navigational procedural challenge. The soft material steerable device presented here has the potential to facilitate a number of procedures that require sub-millimeter diameter catheters in other delicate surgical locations.

## 6.4 Acknowledgements

**Chapter 6** is partially based on the material that is prelminarily accepted in *Science Robotics* (2021), authored by Gopesh Tilvawala, Jessica Wen, David Santiago-Dieppa, Scott Pannell, Bernard Yan, Alexander Norbash, Alexander Khalessi, and James Friend. The dissertation author was responsible for 3D printing, acetone smoothing and assembly of the

full-size model.

# Chapter 7

# Ophthalmology

## 7.1 Introduction

Intraocular pressure (IOP) is the primary modifiable risk factor in the development and progression of glaucoma. Reliable measurements of IOP are crucial in the management of this sight-threatening disease. The gold standard for IOP measurement for more than 50 years has been Goldmann applanation tonometry (GAT) [175]. GAT is a non-invasive measurement technique that infers IOP from the force required to flatten a portion of the cornea. However, accurate GAT assessment of IOP is dependent on an ideal eye and can be affected by many factors including corneal thickness, corneal curvature, and irregular corneal biomechanical properties [176]. Furthermore, GAT is not possible in patients with a Boston keratoprosthesis (KPro) due to the inelasticity of the implant.

New technologies have attempted to address the shortcomings of GAT. The accuracy of Dynamic Contour Tonometry (DCT) is less affected by corneal thickness than corneal curvature [177]. The ocular response analyzer likewise is less influenced by corneal properties and provides measures of corneal biomechanics through corneal hysteresis [178]. The Diaton tonometer measures IOP through transpalpebral tonometry, and can be used to measure

IOP in KPro patients, but the device is not very accurate [179]. Implantable IOP measurement devices circumvent potential artifacts by directly measuring IOP but require a surgical procedure [180, 181].

Intravitreal injections for the treatment of retinal disorders are performed millions of times per year [182]. Intravitreal injections have been widely adopted due to their favorable safety profile, with infections associated with fewer than 1 in 6,000 injections [183]. Anterior chamber paracentesis is less common but is also safe and has a low risk of iatrogenic complications [184]. This presents the possibility of directly measuring intraocular pressure in the anterior or vitreous chambers. Advances in micro-manometric technology have made this increasingly feasible for the clinician. Previous studies have demonstrated the use of needles inserted directly into the eye to measure pressure, but these devices were not hand-held, used larger gauge needles, measured the pressure imposed from an upstream reservoir rather than a direct measure of anterior chamber pressure, and are not disposable [185–188]. In one study the results of upstream measurements were confirmed with direct measurements from the anterior chamber, but this required a large 23 gauge needle and was conducted at specific pressures of 20 and 60 mmHg [188]. Here, we present a novel direct IOP measurement device that provides rapid and accurate measurements and is independent of the cornea. The device is ergonomic, hand held, and has a disposable needle and sensor that can be discarded after use. The device was tested *ex vivo* in rabbits and accurately measured IOP in the anterior chamber and vitreous chamber of vitrectomized eyes.

## 7.2 Methods

**Micromanometry System:**

A high-resolution pressure sensor (2SMPP-03, OMRON, Kyoto, Japan), suitable for both pneumatic and hydraulic sensing, was integrated with a custom designed circuit that enables obtaining accurate measurements of the IOP via a USB interface as shown in Figure 7.1. The pressure sensor and circuit were assembled in a custom designed, 3D printed, and palm-sized housing. The assembled device is comprised of an acquisition circuit and disposable unit which includes the pressure sensor and needle. A 30- or 33-gauge needle (PRE-33013, TSK Laboratory, Japan) was primed with sterile balanced salt solution (BSS) and connected to a pressure sensor through a Luer lock mechanism. Analog signal delivered from the pressure sensor was converted to digital via an Arduino Due (ADU, A000062, Arduino, Ivrea, Italy) board at an acquisition rate of 50ms (20Hz). Internal circuitry ensures that pressures outside the measurement range do not create voltages large enough to damage the Arduino Due. This is achieved via a Wheatstone bridge built into the pressure sensor. The voltage is then amplified with a precise gain using an instrumentation amplifier (INA126, Texas Instruments, Dallas, TX, USA) that sets the sensitivity of the pressure measurement. The output is then limited using two limiter circuits; one for the upper bound and the other for the lower bound of the expected pressure range. The upper and lower bounds are set by the internal ADC of the Arduino Due, but the sensitivity of the measurement can be changed by adjusting the feedback resistor of the instrumentation amplifier. The internal Arduino Due ADC then digitizes the analog signal at a user-defined sampling rate. The digital signal transmitted to a computer through a standard USB interface was used to infer the output reading in mm Hg based on calibration measures described below.

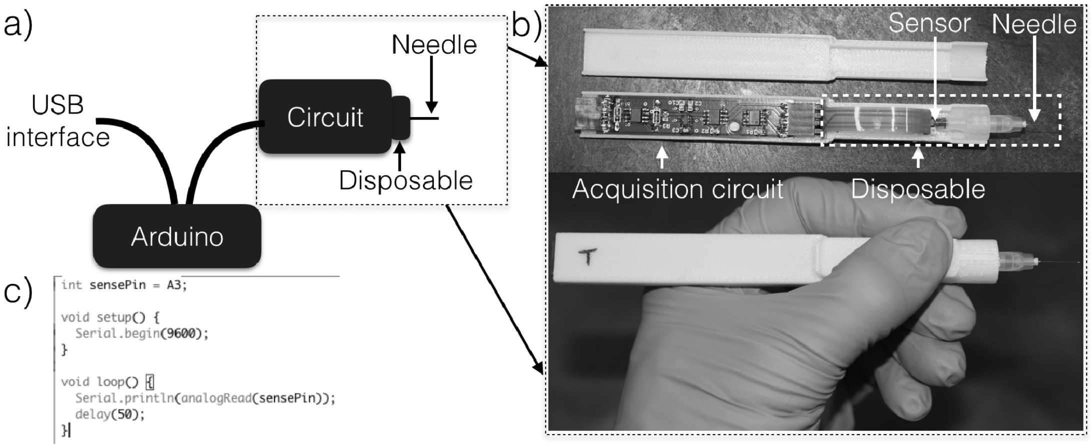

```
int sensePin = A3;

void setup() {
  Serial.begin(9600);
}

void loop() {
  Serial.println(analogRead(sensePin));
  delay(50);
}
```

**Figure 7.1**: a) Illustration of the device acquisition set-up. b) Image of the circuit and disposable part which get assembled in a custom 3D printed housing. c) The code for the Arduino used to acquire data.

**Calibration and Testing:** A high-resolution microfluidics pressure control system (microfluidics control, OB1, Elveflow®, Paris, France) was used to control the pressure imposed on the pressure sensor to produce a calibration curve. This was obtained in the first instance by connecting the microfluidics control system to the sensor needle through an elastic membrane to better represent an actual eye. This test was conducted to ensure the sensitivity of the micro-manometric system was sufficient to capture the changes imposed by the microfluidics control system and subsequently obtain the calibration equation for the sensor. An elastic *ex vivo* model of the eye was constructed to which the microfluidics control system was connected using a 25-gauge needle (25G 1, BD Eclipse®, NJ, USA). The elastic model is a closed membrane chamber comprised of a polymer with mechanical properties similar to a cornea. [189] The membrane chamber was filled with BSS and a vacuum chamber was used to eliminate dissolved air that could later lead to entrapped air bubbles. The microfluidics control system added or removed BSS in the membrane chamber to increase or decrease the pressure of the system. The needle sensor device was connected to the closed chamber with either of two needle sizes (30-g × 1/2 in and 33-g × 1/2 in), effectively submerging the sensor in BSS, and the pressure was varied using the microfluidics control system. Sensor readings were recorded while increasing the pressure from 0 to 103.4 mm Hg (2 Psi), and back to 0 with steps of 10.3 mm Hg (0.2 Psi). The readings were used to calibrate the sensor relative to the pressure imposed by the microfluidics control system. Linear regression analysis was used to compute the $R^2$ values and establish a linear correlation between the sensor readings ($S$) and the imposed pressure ($P_{IN}$) such that: $S = aP_{IN} + b$, where $a$ and $b$ are correlation coefficients.

The sensor needle device was then tested in *ex vivo* rabbit eyes. Rabbits sacrificed following non-ophthalmic studies were obtained through a tissue transfer agreement approved by the University of California San Diego Institutional Animal Care and Use Committee and all work was performed in adherence to the ARVO Statement for the Use of Animals in Ophthalmic and Vision Research. The microfluidics control system was connected to a 25-gauge needle and inserted into the anterior chamber of the eyes. The sensor needle was then inserted into the anterior chamber and likewise maintained in a fixed position on a stabilizer arm as shown in Figure 7.2. Although the device can be hand held during measurements, the stabilizer arm was utilized due to the number of measurements taken. Two needle sizes, 30-g × 1/2 in and 33-g × 1/2 in, were used to obtain sensor readings for the pressure changes in the anterior chamber. After obtaining readings with one needle, the disposable unit comprising of the pressure sensor and needle was replaced with a new unit using a push-fit connection to obtain the next set of readings.

The input pressure in the anterior chamber pressure was varied from 0 to 103.4 mm Hg (2 Psi) in 10 mm Hg (0.2 Psi) increments. The device was evaluated using the calibration equation from the elastic membrane chamber, $P_M = \frac{S-b}{a}$, where $P_M$ is the measured pressure, $S$ is the sensor reading, $a$ and $b$ are the linear correlation coefficients. The

IOP was also measured using a Tonopen following the device reading for each increment in pressure. Measurements were repeated for five eyes using both needle sizes (10 eyes total), replacing the disposable unit comprised of the sensor and needle with a new unit using a push-fit connector.

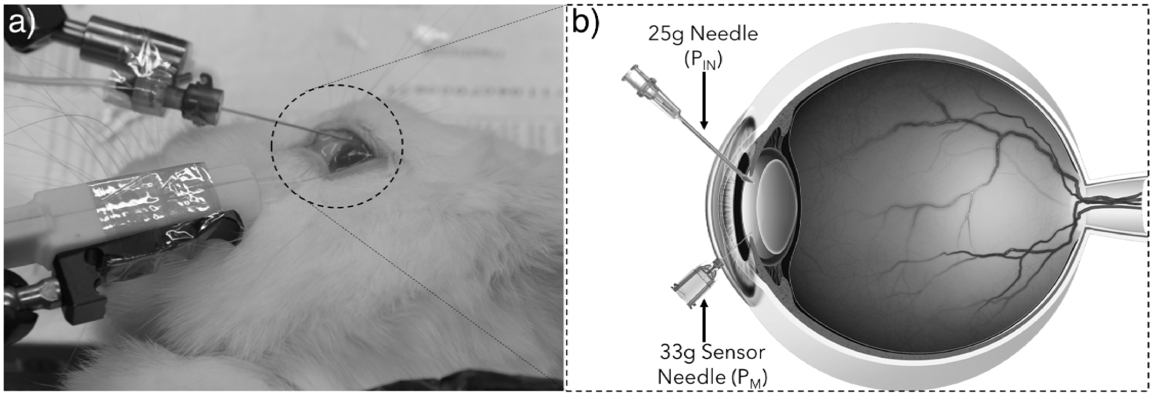

**Figure 7.2**: a) Image of the test setup in rabbit eyes, b) illustration of supply pressure and sensor needle. The 25 g needle was used to supply pressure from the microfluidics control system and the sensor needle used to measure the pressure change in the anterior chamber.

The tests were repeated in the vitreous chamber of vitrectomized rabbit eyes. Similar to the anterior chamber measurements, a 25 g needle attached to the microfluidics control system was inserted into the vitreous chamber and held in a fixed position using a stabilizer arm. The sensor needle was inserted into the vitreous chamber and two needle sizes, 30-g × $^1/_2$ in and 33-g × $^1/_2$ in, were again used to measure the pressure changes in the vitreous chamber. The pressure imposed by the microfluidics control system was varied from 0 to 103.4 mm Hg (2 Psi) in 10 mm Hg (0.2 Psi) increments and sensor readings taken at each increment. The IOP was also measured using a Tonopen simultaneously with the sensor readings.

## 7.3 Results

### 7.3.1 Calibration

The sensor of the micro-manometry system was tested through a connection to an elastic membrane chamber that exhibits a linear relationship with the pressure imposed by the microfluidics control system for both the needles, 30-g × ½ in and 33-g × ½ in. Scatter plots of the pressure recorded by the sensor needle device against the pressure imposed by the microfluidics control system are shown in Figure 7.3.

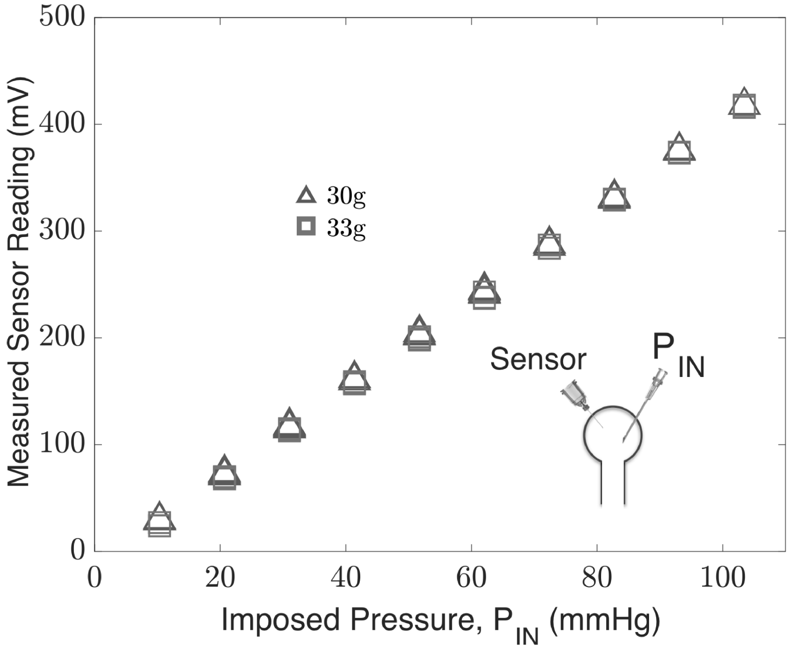

**Figure 7.3**: Sensor needle device readings obtained by connection to the microfluidics control system in an elastic membrane chamber using 30-g × ½ in and 33-g × ½ in needles.

The sensor reading is linearly dependent ($R^2 > 0.99$) over 0 to 103.4 mm Hg, and the change in the reading in replacing a 30-g needle with a 33-g needle is insignificant according to a paired T-test ($p < 0.05$). The results indicate the sensitivity of the device is sufficient to capture the changes imposed by the microfluidics control system over a pressure range of 0 to 103.4 mm Hg (2 Psi), with increments of 10.3 mm Hg (0.2 Psi). The calibration equations for the sensor in an elastic membrane chamber measurements are shown in Table 7.1, where the sensor reading, $S$, is expressed as a linear function of the imposed pressure, $P_{IN}$.

**Table 7.1**: Sensor needle device calibration equations.

| Equation | Needle | |
|---|---|---|
| S = a$P_{IN}$ + b | 30-g | 33-g |
| a | 4.16 | 4.18 |
| b | -13 | -17 |

### 7.3.2 *Ex vivo* rabbit eyes:

The same test was conducted in rabbit eyes, with the sensor acquisition rate at 50ms (20Hz) for both the needles, 30-g × ½ in and 33-g × ½ in. The calibration equations from the elastic membrane chamber (Table 7.1) were used to infer the IOP from the sensor needle device such that: $P_M = \frac{S+13}{4.16}$ (30-g needle) and $P_M = \frac{S+17}{4.18}$ (33-g needle), where $P_M$ is the measured pressure and $S$ is the sensor reading. The sensor device measurements were compared against those obtained by the Tonopen. The results in Figure 7.4 demonstrate the accuracy of the device with a strong linear correlation between the imposed ($P_{IN}$, x-axis) and measured ($P_M$, y-axis) pressure for both the 30-g and 33-g needles. The coefficient of determination ($R^2$) was excellent for both needle sizes ($R^2$ = 1.0 and 0.99 for the 30- and 33-g needles, respectively), and the Tonopen in both trials ($R^2$ = 0.98 and 0.99). The data was confirmed to be normal via the Shapiro-Wilk test with significance $p < 0.05$ and $n = 10$. Pooled variances for the readings were used to determine the average standard deviation of each measurement device. The average standard deviation of the 30- and 33-g needles (1.32 and 2.7 mm Hg, respectively) were much smaller than that of the Tonopen in either trial (6.12 and 9.02 mm Hg, respectively).

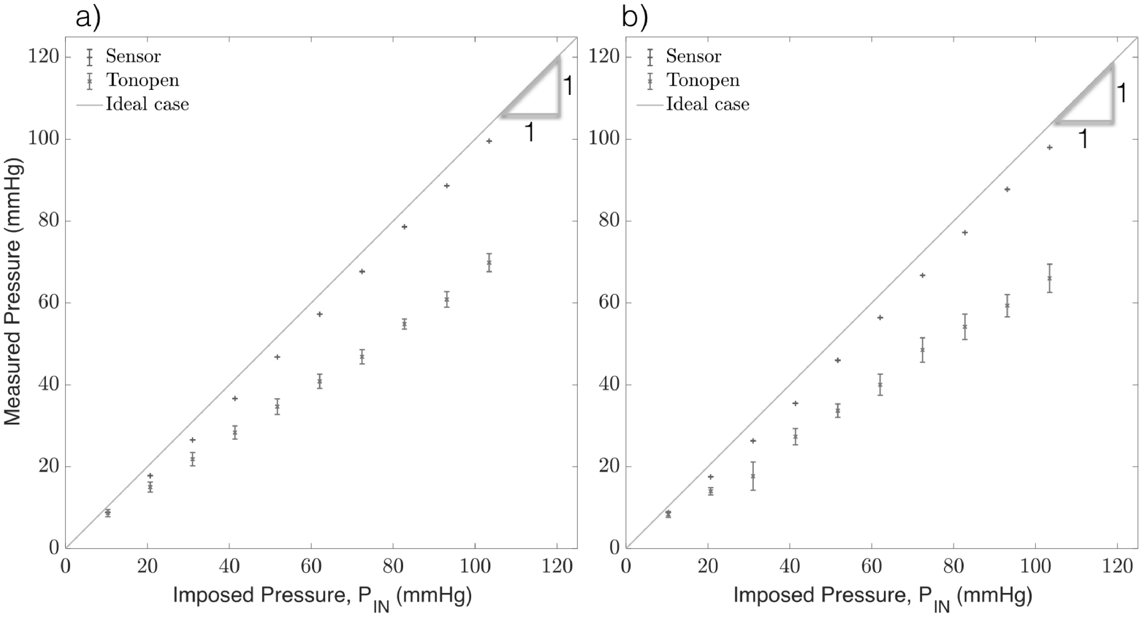

**Figure 7.4**: Anterior chamber pressure measurements using the sensor needle device and tonometry for a) 30-g Needle, b) 33-g Needle.

The relative error was evaluated as $\frac{P_{IN}-P_M}{P_{IN}}$, where $P_{IN}$ is the pressure imposed by the microfluidics control system, and $P_M$ is the pressure measured by either the sensor needle device or the Tonopen. The Tonopen underestimates the delivered pressure, particularly at higher pressures, where the relative error for readings obtained by the Tonopen compared to the sensor needle are significantly larger as shown in Figure 7.5. In contrast, the sensor needle device exhibits higher accuracy at higher pressures.

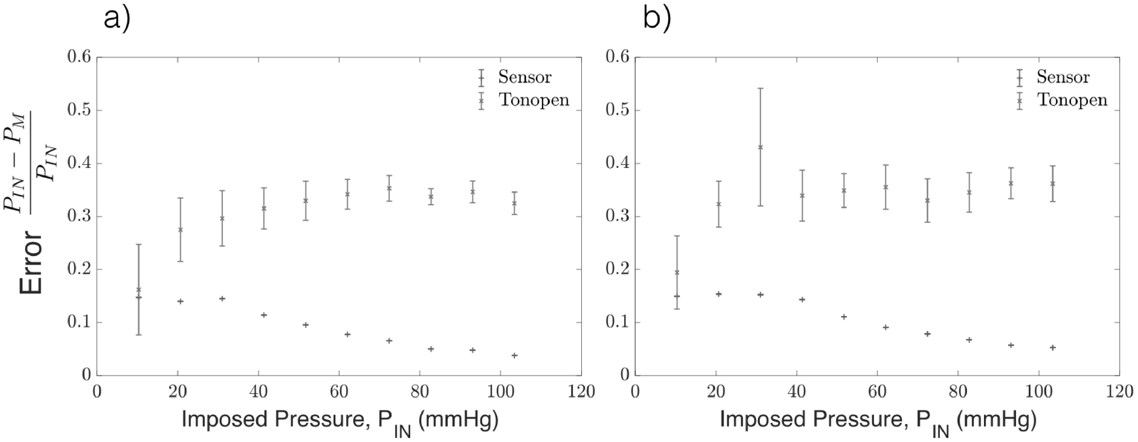

**Figure 7.5**: Error in the anterior chamber pressure measurements using the sensor needle device and tonometry for a) 30-g Needle, b) 33-g Needle.

The tests were repeated in the vitreous chamber of vitrectomized rabbit eyes. Results in Figure 7.6 show the coefficient of determination was excellent for both needle sizes ($R^2$ = 1 and 0.998 for 30- and 33-g needles, respectively). By comparison, the Tonopen readings exhibit a slightly lower coefficient of determination ($R^2$ = 0.97 and 0.98, for tests with the 30- and 33-g needles, respectively).

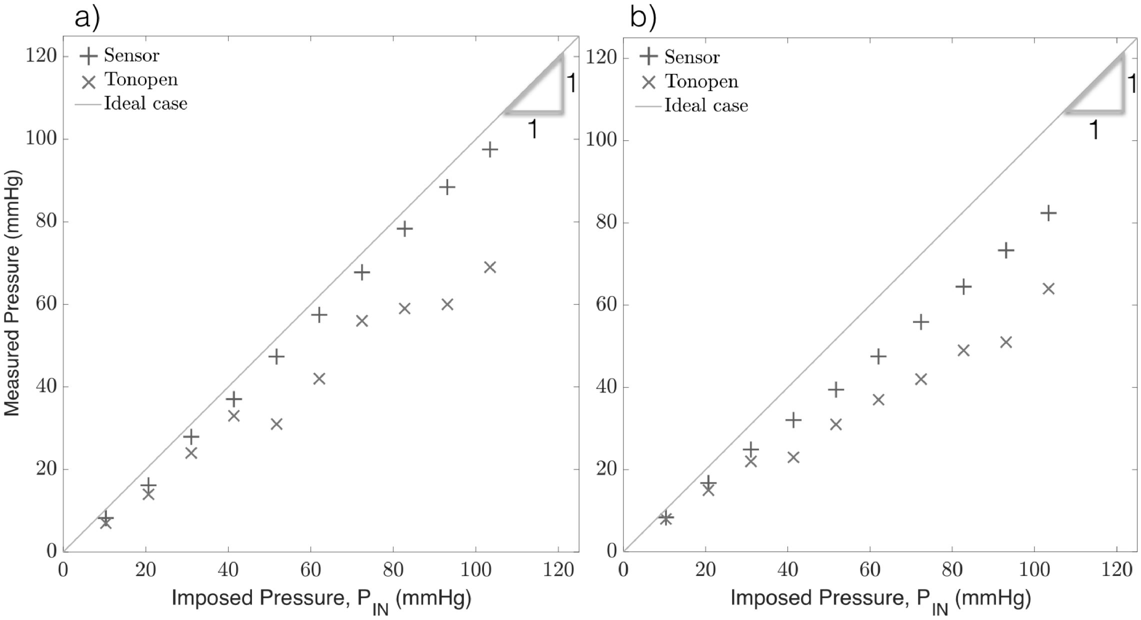

**Figure 7.6**: Vitreous chamber pressure measurements obtained using the sensor needle device and tonometry for a) 30-g Needle, b) 33-g Needle.

The Tonopen also underestimates the pressure readings by over 20% on average as shown in Figure 7.7. The slightly higher error for the 33-g in comparison to the 30-g needle can be attributed to the loss in pressure transmission across the smaller needles' lumen when transmitting pressure from the vitreous chamber to the pressure sensor.

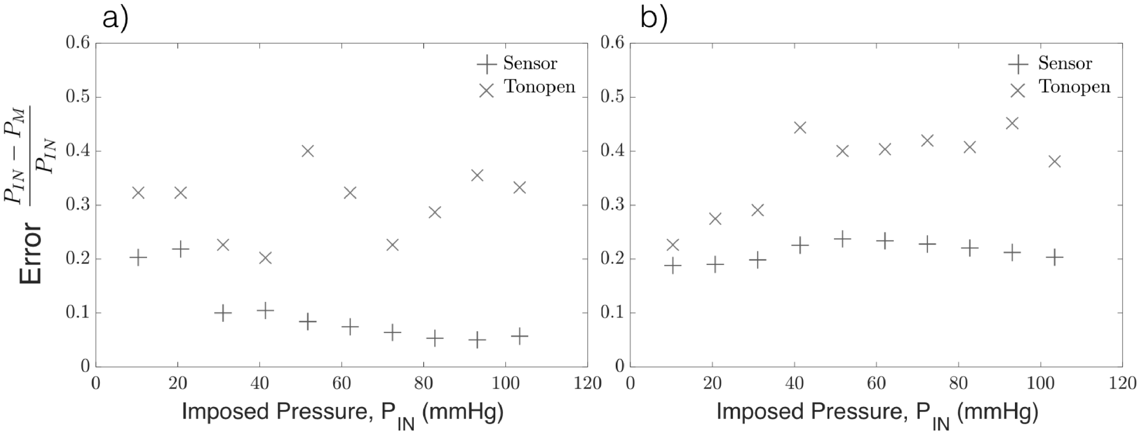

**Figure 7.7**: Error in the vitreous chamber pressure measurements using the sensor needle device and tonometry for a) 30-g Needle, b) 33-g Needle. As the imposed pressure, $P_{IN}$ increases, the error for the readings obtained by tonometry fluctuate or get larger while the sensor needle device stabilizes.

## 7.4 Discussion

Advances in microfabrication have allowed the construction of increasingly sophisticated devices well suited to the small dimensions of the eye. Using the technology described above, a high-resolution pressure sensor was integrated with a 30- and 33-gauge needle to accurately and reliably measure IOP in the anterior and vitreous chambers. Notably, the device provides a direct measure of IOP that is not affected by corneal properties. The device accurately measured IOP in the anterior chamber over a clinically significant range of 10 100 mm Hg (Figure 3.2). In contrast, the Tonopen underestimated the IOP, particularly at higher pressures. This finding is consistent with prior studies showing the Tonopen underestimates IOP in rabbits. [190]

IOP measurements in rabbits can be corrected to account for thinner corneas leading to the underestimation of their IOP. [191] Similar correction factors exist for humans, but their use may not lead to increased accuracy in IOP estimation due to many other factors that may induce artifacts. [192] More complex models that attempt to address additional factors such as the modulus of elasticity are still prone to error. [193, 194] A history of refractive surgery may lead to further inaccuracies in the measurement of IOP due to thinning of the cornea, changes in the corneal curvature, and alterations in the corneal biomechanical properties. [195–197] Corneal scars may influence IOP in even more unpredictable ways due to their varying sizes, depths, and effects on the cornea's biomechanical properties. [198] All of these potential sources of error are frequently encountered in the clinical setting, yet there are limited means to address them. Our device allows for an accurate measurement of IOP in any of these cases. The patient may not need this measurement repeated at every visit if the results are reassuring or can be correlated to GAT or another non-invasive measurement technique. However, the opportunity for direct IOP measurement would be a useful addition to a clinicians armamentarium.

The device also accurately measured IOP in the vitreous chamber after vitrectomy (Figure 3.4). We were unable to measure IOP in the vitreous chamber without vitrectomy because vitreous rapidly clogged the measurement needle, voiding the sensor reading. A similar result was found in prior cannulation studies. [199] However, despite this limitation, direct measurement of IOP in the vitreous chamber following vitrectomy is clinically useful. As many as 60% of Kpro patients develop glaucoma, but the disease is difficult to manage due to the inability to accurately measure IOP. [200] Management of chronic vision-threatening complications like glaucoma in Kpro patients is becoming increasingly important as early complications such as endophthalmitis or device extrusion are becoming less common. [201, 202] Many Kpro patients receive vitrectomies at the time of Kpro implantation. These patients may benefit enormously from the accurate measurement of IOP in the vitreous chamber.

Telemetric IOP monitors have been implanted into a small cohort of KPro patients and offers an alternative method for direct measurement of IOP in these patients. [203] However, three of twelve devices were explanted over the course of a year and there were concerns for potential adverse events associated with the devices. Our device may offer a safe alternative in Kpro patients. Interestingly, data from the implantable IOP monitors were compared to anterior chamber manometry. [204] This suggests that it may be possible to measure IOP using our device in KPro patients even without vitrectomy. However, serial anterior segment imaging has demonstrated progressive angle closure and shallowing of the anterior chamber in KPro patients, so anterior chamber measurements may still not be viable over the long term. [205] Implantable devices also face issues of measurement drift over the lifetime of the device. [206, 207] Implantable devices can be re-calibrated to correct for drift by performing GAT in healthy eyes, but this is not possible in KPro patients. Our device may be useful for re-calibration of implantable devices as their safety profiles become more acceptable.

The use of the term gold standard to describe a diagnostic technique or therapeutic intervention has been criticized as inaccurate or misleading due to the rapidly evolving state of medical care. [208, 209] Nonetheless, GAT has long been referred to as the gold standard for IOP measurement. [175] However, accurate measurement of IOP by GAT is hampered by the corneal and biomechanical artifacts discussed above. Anterior chamber cannulation manometry in animal models allows for accurate IOP measurement but was previously hampered by the invasiveness of the technique. [210,211] Now, microfabrication techniques allow clinicians to directly measure IOP through the use of implantable devices or minimally invasive procedures. Thus, a true IOP is measured rather than the surrogate IOP measured by non-invasive techniques. The small size of the handpiece and needle make this a feasible clinical measurement, with safety offered by the ability to dispose of the needle and sensor after each use. We propose that these new methods could provide a true gold standard for IOP measurement in appropriately selected patients.

This study had several limitations. First, the study was performed entirely in *ex vivo* models so the potential long-term complication rates of direct measurement of IOP in the anterior and vitreous chambers are unknown. However, the safety profiles of anterior chamber paracentesis and intravitreal injections offer promise for a similarly safe procedure that could be performed in an office setting. Second, we performed vitreous chamber measurements in only two eyes. The difficulty of fully closing sclerotomies following vitrectomy led to unstable eyes and variable IOP measurements at higher pressures. Eyes that are allowed to heal and develop fully watertight closures following vitrectomy are not expected to face similar inaccuracies. Finally, the device will benefit from further miniaturization. While the current device requires a USB connection to a computer to obtain readings, future iterations adapting advancements in wireless technology will enable further miniaturization and portability. Despite these limitations, this device offers a feasible alternative for IOP measurement in patients with altered or artificial corneas.

## 7.5 Acknowledgments

This work was performed in part at the San Diego Nanotechnology Infrastructure (SDNI) of UCSD, a member of the National Nanotechnology Coordinated Infrastructure, which is supported by the National Science Foundation (Grant ECCS–1542148). The work presented here was generously supported by a research grant from the state of California via AB2664.

**Chapter 7** is entirely based on the material that is published in *Translation Vision Science and Technology* (2020) authored by Gopesh Tilvawala, Andrew Camp, James Friend, and Robert Weinreb [5]. The dissertation author was responsible fabrication, assembly, and testing of the device.

# Chapter 8

# Vacuum exhausted isolation locker (VEIL) to reduce droplet/aerosol transmission while treating COVID-19 patients

## 8.1 Introduction

Patients with acute respiratory failure from SARS-nCoV-2 infection have strained hospitals in the initial phase of the COVID-19 pandemic, and may again depending on the consistency and adherence to public safety policies. Patient treatment protocols and hospital resources are stressed in these emergencies, not only due to the patient numbers but also due to the risk these patients represent in infecting healthcare workers. Virus-laden droplets from patients with respiratory infections—even those with mild symptoms—may be expressed and deposited on surfaces in hospital rooms [212] to potentially infect those that later come into contact with those surfaces. The lack of sufficient invasive ventilators and trained personnel to set and monitor them in the first surge of COVID-19 in many countries including the U.S. likewise indicates the urgent need for better treatment options, as does the reliance on and inadequate supply of healthcare workers' personal protection equipment (PPE). With evidence now that SARS-nCOV-2 may be transmitted as an airborne virus [213], the importance of introducing and maintaining prophylactic measures for healthcare workers is never greater. Methods to reduce both healthcare worker exposure to COVID-19 and the need for complex medical equipment would therefore benefit both healthcare workers and patients.

The SARS-CoV-2 virus responsible for this public health crisis bears biological similarity to SARS-CoV-1 responsible for an outbreak in Toronto in 2003. Because the two viruses exhibit similar stabilities as aerosols and surface-deposited materials, it is reasonable to presume their transmission characteristics are similar [214]. Knowledge of how SARS-CoV-1 is transmitted may produce ideas in reducing the risk of transmitting SARS-CoV-2 to healthcare workers during this pandemic. A three-fold increase in transmission of SARS-CoV-1 to healthcare workers in the Toronto outbreak was associated with their use of noninvasive mechanical ventilation in treating SARS-CoV-1 infected patients [215]. Compared to invasive endotracheal intubation and ventilation, noninvasive mechanical ventilation was associated with twice the infection incidence in nursing staff caring for SARS-CoV-1 patients [216]. Certainly the exposure of healthcare workers during treatment of SARS-CoV-1 patients increases their risk of infection: a comprehensive meta-analysis of both invasive and non-invasive aerosol-generating procedures (AEPs), including resuscitator bag mask ventilation, endotracheal intubation, airway suctioning, bronchoscopies, bi-level positive airway pressure (BiPAP), and continuous positive airway pressure (CPAP) were all consistently associated with increased transmission risk of SARS-CoV-1 to healthcare workers [217].

Non-invasive ventilation methods, especially heated, humidified high-flow (60 L/min) nasal oxygen (NHF or HHFN) may produce improved outcomes in COVID-19 patients with hypoxemic respiratory failure. Non-invasive ventilation methods have long been used to reduce morbidity and mortality, and, when paired with $\leq$ 15 L/min oxygen supplementation and nebulized bronchodilators, are often used in treating patients with compromised respiration. Furthermore, CPAP/BiPAP machines with modification have been approved for emergency use by the U.S. Food and Drug Administration (FDA) in late March 2020 as non-invasive ventilators.

Over the last decade, however, far higher non-invasive ventilation flow rates of up to 60 L/min in NHF have been associated with outcomes [218–221] superior to lower flow methods. A recent investigation of hypoxemic respiratory failure patients in both meta-analyses of past trials and an additional randomized trial all suggest NHF reduces the rate of invasive intubation and mechanical ventilation [218,219,221] over traditional methods. Likewise, ICU-related mortality of critically ill hypoxemic respiratory failure patients is reduced using NHF [220].

Because SARS-CoV-2 is already known to be highly infectious with $R_0 = 5.7$ [222], and despite the many advantages of non-invasive methods including NHF, physicians are understandably reluctant to use these methods in COVID-19 patients with hypoxemic respiratory failure because they are reasonably perceived to spread patient-exhaled aerosols and droplets, consequently increasing the risk of viral transmission to healthcare workers [223]. The SARS-CoV-1 outbreak predates the widespread use of NHF treatment in patients, and so transmission of SARS-CoV-1, or, indeed any viral pulmonary infection to date using NHF has not been considered. However, pathogenic transmission from traditional non-invasive ventilation and NHF-treated patients with gram-negative bacterial pneumonia has been studied [212, 224]. The bacteria were found on collection plates 0.4 m and 1.5 m away from the patient's head when using NHF or oxygen ventilation via a standard face mask with open ports and no exhalation filters [224]. Coughing—a common symptom of COVID-19—appears to disperse bacteria-laden droplets even further: with 60 L/min NHF and simulated coughing in healthy volunteers, such droplets were found 3 m away, about 0.5 m farther than without coughing. Exhaled smoke, which has particles of a similar size to to 110 nm SARS-CoV-2, appear up to 6.5 cm away from physiological tidal breathing without coughing. Smoke is dispersed much farther away with NHF to 17.2 cm, and notably 62 cm away when the nasal prongs are dislodged from the nose [212, 224]. Like NHF, the lower-flow non-invasive ventilation methods including CPAP and BiPAP machines may increase COVID-19 transmission risk. These methods lack the viral filters and controlled exhalation pathways of invasive methods, allowing viral particles to enter the hospital room and potentially infecting those in it.

There is an urgent need for a device to reduce the risk of COVID-19 virus transmission associated with non-invasive ventilation. Reducing healthcare workers' exposure to the virus would increase their safety, provide non-invasive treatment options that appear to produce better patient outcomes, and altogether serve to reduce COVID-19 transmission and patient morbidity and mortality.

Canelli, *et al.*, described in a recent, COVID-19-related publication the utility of a physical patient enclosure to avoid contamination of a physician's PPE from patient coughing during intubation [225], and there are many variations on this approach now in the literature [226]. Here, we provide a lightweight, rigid enclosure—the *vacuum exhausted isolation locker* (VEIL)—that both provides healthcare providers with a safety barrier while administering care and a means to safely provide non-invasive ventilation. Through appropriately placed vacuum ports connected to hospital suction via viral particle filters and a sputum canister, the exhaled aerosols and expectorated droplets from a patient are continuously removed. Made by waterjet or mechanical cutting a 30-mm thick sheet of polycarbonate plastic that is subsequently bent into a simple box shape by thermal line bending, the VEIL includes two vacuum ports for continuous air extraction at 60–80 L/min. This places the interior of the VEIL in a mild vacuum and prevents loss of virus-laden material to the room, even during noninvasive ventilation using CPAP, BiPAP, and NHF. It also maintains patient comfort, as the

VEIL is large enough for the patient to move around within and to allow inclination of the gurney so the patient may sit upright. Flexible flap-covered slots on the lateral sides of the VEIL allow passage of ventilation tubing without excessive vacuum loss. Polycarbonate was selected as it is more durable than acrylic or polyvinylchloride (PVC), may be disinfected with known methods used in a hospital, and is transparent to xrays. In our experiments, droplets and aerosols were generated and monitored to demonstrate the VEIL system effectively removes virus-laden air when connected to standard hospital vacuum.

## 8.2 Methods

Polycarbonate sheet (1/8") was pre-cut using a table router and formed into a 175 L 3D shell via thermal bending. The enclosure was closed with a polyvinylchloride drape and placed at the head position of a gurney (Figure 8.1). Water-jet cutting of polycarbonate is a useful alternative, though laser machining is not: polycarbonate tends to produce noxious gases when cut by laser. Noninvasive ventilation tubing, including the larger corrugated tubing utilized by NHF, may be passed via flap-closed horizontal slots in the enclosure, minimizing air leakage around the tubing. Two exhaust ports enable continuous evacuation of air using hospital suction via viral particle filters. The design is accommodates standard hospital beds and changes in the inclination without risk of the VEIL becoming dislodged.

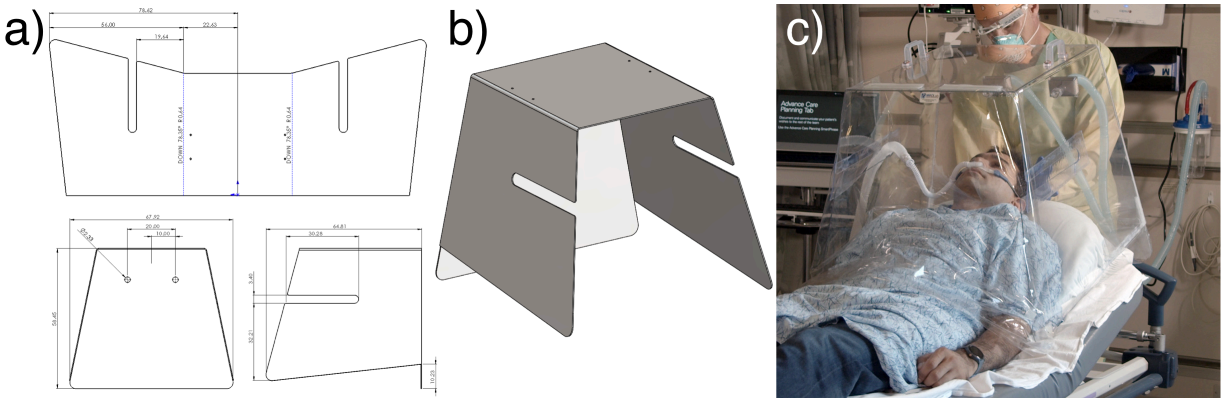

**Figure 8.1**: Polycarbonate sheet (a) cut in a pattern as shown may be bent by heated line bending into a four-sided box (b) as the VEIL shell. It covers the patient's upper body with a (c) soft PVC drape to enclose the space around the midsection of the patient against the bed.

To determine whether the proposed VEIL provides an effective viral barrier to protect healthcare workers, droplets and aerosols were generated within the enclosure at approximately where the patient head would be located. Droplets are relatively large particles expectorated from patients and travel only a short distance, one meter or less, to settle on surfaces. Aerosols are sub-100 $\mu$m particles carried by air convection over farther distances (> 1 m). The VEIL was placed at the head of a standard hospital bed (S3, Stryker, Kalamazoo, MI USA) in a hospital room. A professional video camera (Pocket Cinema 4k, Blackmagic Design, Burbank, CA USA; 16 mm cine lens, Rokinon, New York, NY USA), placed 3 feet from the foot of the bed and 6 inches above the top of the mattress plane, was used to image the veil and droplets and aerosols within. The bed was surrounded by a flat black backdrop in the field of view of the camera as a non-reflective background. Two LED flood lights were placed laterally on either side of the VEIL and out of view of the camera to indirectly illuminate droplets and aerosols around the head of the bed.

An oxygen-driven nebulizer (AeroEclipse II, Monaghan Medicine, Plattsburgh, NY USA), mounted in a position representative of a patient's head on the bed, was used to generate droplets from tonic water (Canada Dry, Keurig Dr Pepper, Burlington, MA USA) containing quinine, which fluoresces under ultraviolet illumination, and 200 $\mu$L of Fluorescein (AltaFluor Benox, Sodium 0.25%/Benoxinate HCl 0.4%) using 15 L/min of $O_2$. A healthy subject used a vaporizer to generate aerosols while in a supine position. The size distributions of the droplets and aerosols generated using these methods were found to represent the reported sizes of expectorated droplets [2] and exhaled aerosols [3] from a human (Figure 8.2).

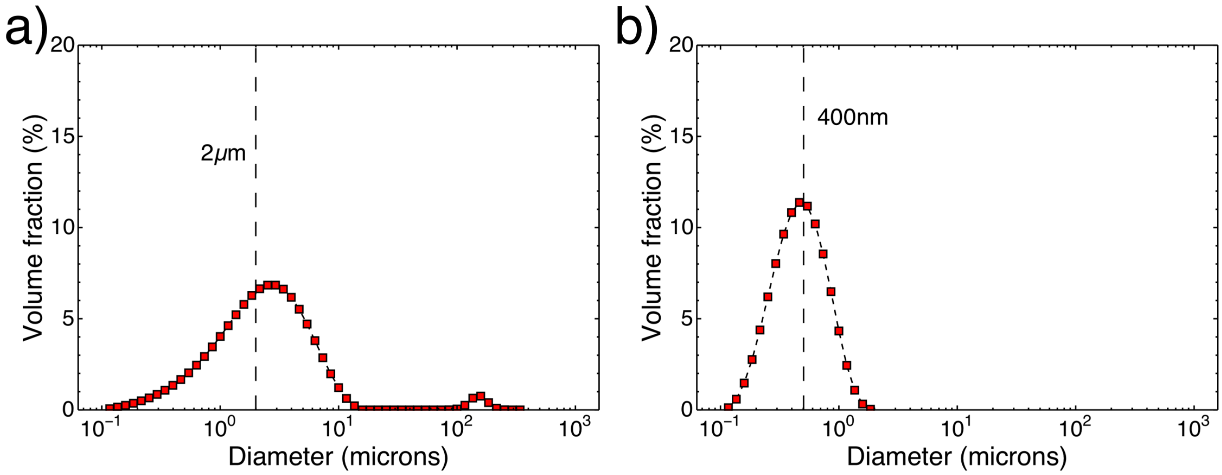

**Figure 8.2**: (a) The nebulizer used in our study produces 200 nm to 100 $\mu$m droplet size distributions representative of expectorated droplets [2] while (b) a vaporizer used by a healthy human subject produces, via expiration, 100 nm to 2 $\mu$m aerosols representative of human exhaled aerosols [3].

Three different conditions were simulated to assess containment and evacuation of droplets and aerosols: (1) ambient air, (2) VEIL without exhaust, and (3) VEIL with continuous exhaust using standard hospital suction. For each condition, the nebulizer was was turned off after continuously running for the first 4 minutes. For (2) the VEIL without exhaust, the vacuum was then turned on four minutes after the nebulizer was turned off. This enables assessment of the suction performance in drawing out droplets and aerosols after they are spread throughout the VEIL, as opposed to condition (3) where the droplets and aerosols were never allowed to accumulate prior to starting the suction.

Scattered fluorescence illumination during video capture together with image processing on MATLAB (Mathworks, Matick, MA USA) was used to produce quantitative imagery of the droplets and aerosols. The post-processing subtracted the background and stationary details in the videos, leaving on a predominantly black background the droplets and aerosols visible as white spots, the pixel intensity and number of which correspond to the amount present [227]. Interrogation regions were defined to quantify the amount of droplets and aerosols present within these regions, as indicated in Figs. 8.3 and 8.4 as follows: inside the VEIL (green), outside the VEIL (purple), upper part of VEIL (red), and lower part of VEIL (blue).

## 8.3 Results

### 8.3.1 Droplet transmission

Without VEIL containment, droplets continuously exit the nebulizer and descend to and along the bed out of view to the room floor (Figure 8.3: A1-A3). With the VEIL in place, the droplets are confined within the VEIL enclosure (Figure 8.3 B1-B3). Introducing standard hospital suction reduces the droplet concentration in the VEIL to match the ambient air outside the VEIL. This occurs whether the suction is on from the start in Figure 2(C1-C3) or turned on after four minutes of droplet nebulization into the VEIL in Figure 8.3(B2, gray box), indicating an effective method for reducing droplet concentration. During the first four minutes running the nebulizer, the effect of suction is evident with a relatively lower mean pixel intensity in the blue interrogation box (Figure 8.3 C2) compared to (Figure 8.3 B2). Likewise, the total pixel intensity within the VEIL (green box) is lower in when the suction is continuously running (Figure 8.3 C3) as compared to no suction (Figure 8.3 B3).

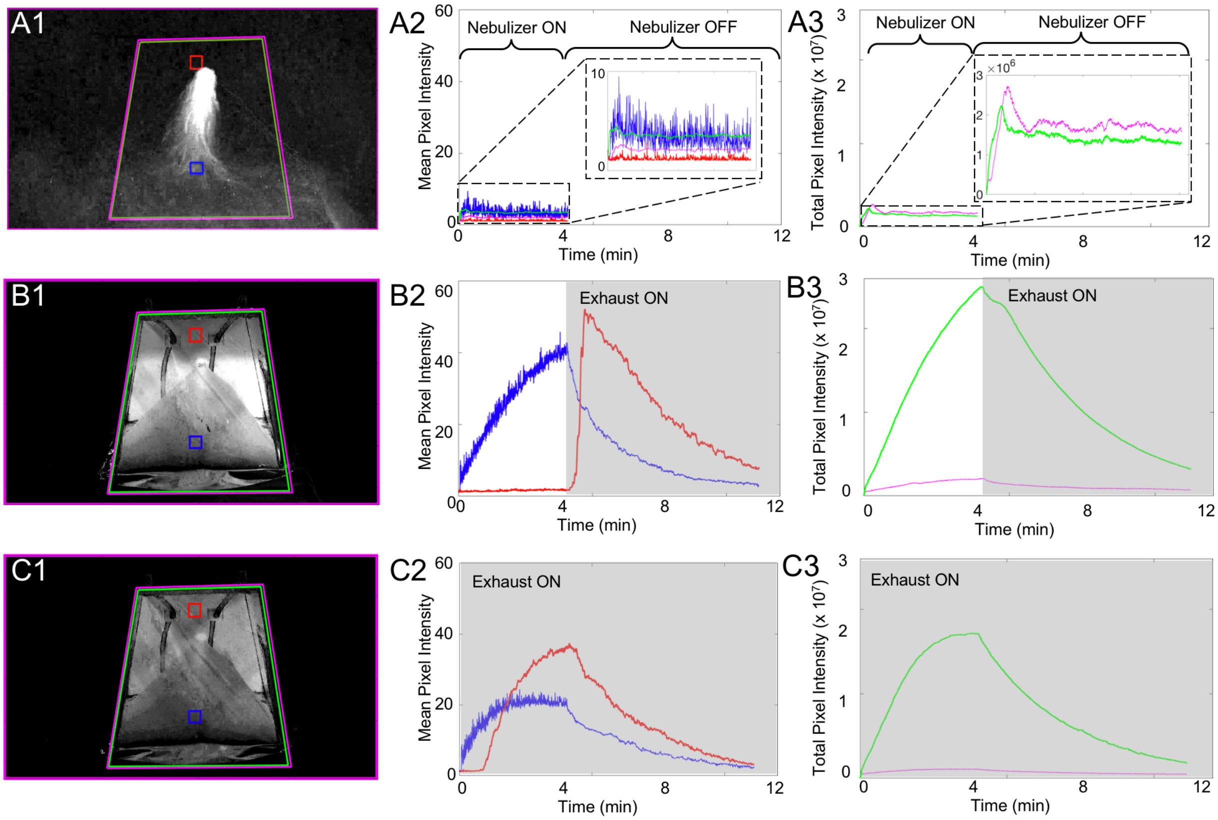

**Figure 8.3**: Scattered fluorescence images, mean pixel intensities, and total pixel intensities from droplet generation experiments serve to quantify the effectiveness of containment and suction extraction of droplets and aerosols. Nebulization continuously produced droplets from 0 to 4 min into (A) ambient air without the VEIL, (B) VEIL with suction turned on at 4 min, and (C) VEIL with continuous suction. Mean pixel intensity measurements were obtained from two regions of interest: the upper portion of the VEIL, outlined in red; and the lower portion of the VEIL, outlined in blue. Total pixel intensity measurements were produced from two regions of interest: inside the VEIL, outlined in green; and outside the VEIL, outlined in purple.

### 8.3.2 Simulated aerosol transmission

Coughs by a healthy subject can project aerosols from a vaporizer over 1.5 m from the patient's head in ambient air (Figure 8.4: A1-A3). As with droplets, the VEIL effectively contains these aerosols as indicated in Figure 8.4(B1-B3), and standard hospital suction applied to the VEIL effectively extracts the accumulated aerosols to lower their concentration to match the ambient air outside the VEIL (Figure 8.4: C1-C3).

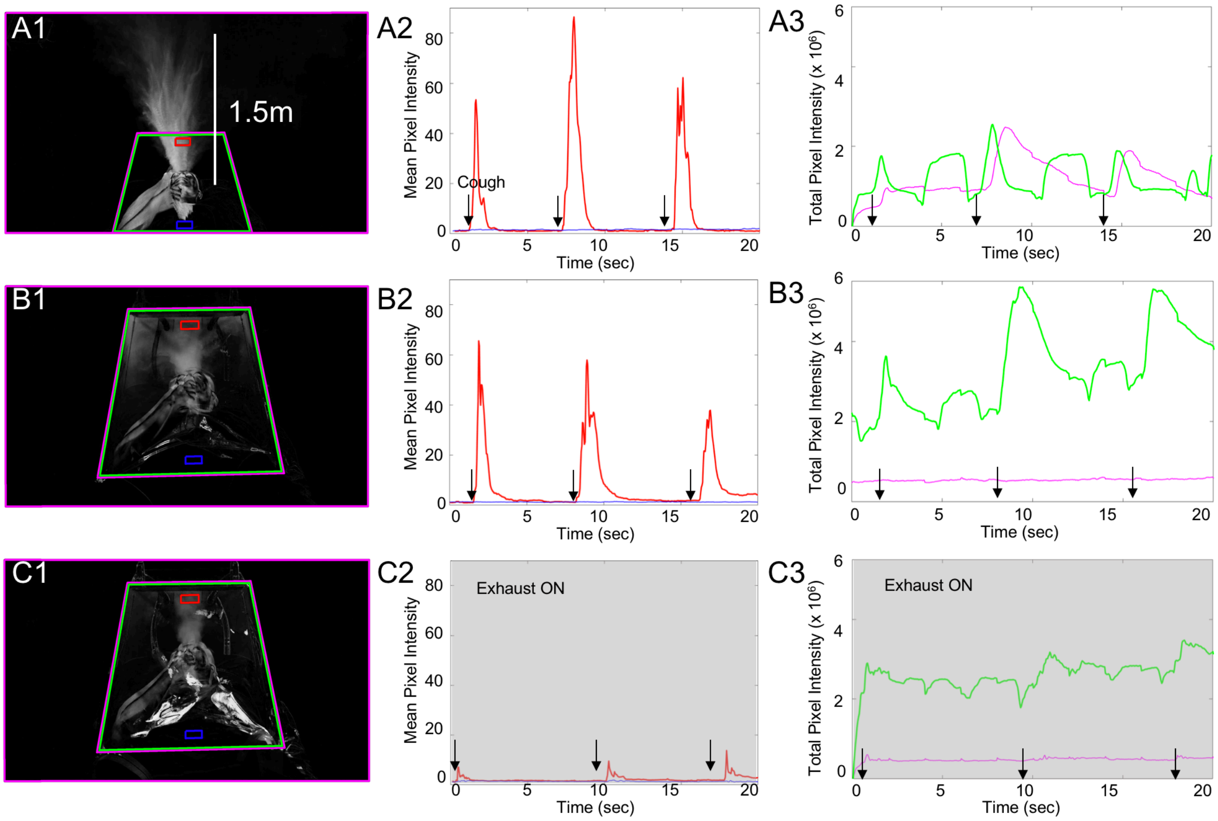

**Figure 8.4**: Scattered fluorescence images, mean pixel intensities, and total pixel intensities from aerosol generation experiments serve to demonstrate the utility of containment and suction in capturing and extracting aerosols. Vaporized aerosols were produced by healthy human coughs (A2-C2, A3-C3 arrows) into (A) ambient air without the VEIL, (B) VEIL without suction, and (C) VEIL with continuous suction. Mean pixel intensity measurements were obtained from two regions of interest: the upper portion of the VEIL, outlined in red; and the lower portion of the VEIL, outlined in blue. Total pixel intensity measurements were obtained from two regions of interest: inside the VEIL, outlined in green; and outside the VEIL, outlined in purple.

## 8.4 Discussion

The VEIL provides an effective barrier for both droplet and aerosol transmission, while the absence of any protective barrier results in wide spread of droplet transmission throughout the room (Figure 8.3A1 and 8.4A1). The use of an enclosure provides a contained environment with slow accumulation of droplets inside the enclosure to a steady-state concentration defined by the loss of droplets due to deposition and continuous introduction of new droplets from the nebulizer (Figure 8.3A2 and 8.4A2). The use of a standard hospital vacuum or suction connected to the enclosure via virus particle filters (Figure 8.3C3 and 8.4C3) achieves baseline level of droplet contents in less than four minutes, more quickly reducing concentration in the VEIL environment as compared to the case of no suction.

Images show that without the VEIL droplets cover the entirety of the bed, aerosols travel 2 m (Figure 8.4A1). With the enclosure the droplets and aerosols are contained within the VEIL. Upon activation of the suction, droplets ascend in response to the suction, increasing their concentration near the top of the VEIL (red curve in Fig. 8.3B2, and subsequently decline to nearly zero after only 10 sec. The concentration of droplets inside and outside the VEIL (green and purple curves in Fig. 8.3B3) slightly increase until the suction is activated, but decline after that in a few seconds. Aerosols likewise accumulate in the VEIL without suction (green curve in Fig. 8.4B3), especially after a cough, but upon activation of the suction the concentration of aerosols within do not increase, and the local aerosol concentrations at the top of the VEIL are far lower with the box (compare Fig. 8.4A2 and B2) and when activating the suction exhaust (compare Fig. 8.4B2 and C2). Unlike the droplets, the aerosols exhibit a continued presence in the VEIL with vacuum due to the simulated patient's respiration and coughs over the brief measurement period of 20 sec.

## 8.5 Conclusions

The VEIL can be rapidly manufactured and deployed to provide safe administration of noninvasive respiratory support therapies such as NHF, BiPAP, or nebulized medications since the suction rapidly draws virus-laden droplets and aerosols away despite rapid gas in-flow rates. During clinical use, the patient will lie semi-recumbent with their head and torso inside the VEIL. About half of the VEILs volume (90 L) will be taken up by the patient.

The air evacuation flow rate of 60-80 L/min is achievable due to current (NFPA 99 [228]) hospital building codes. These require at least 85 L/min vacuum flow rates at 12 $cmH_2O$ vacuum or more for simultaneous use by all patients in a hospital, drawing in air from around the patient and preventing exudate and viral escape. The VEIL enables >30 air changes per minute, a typical hospital room undergoes 2-3. This evacuation rate also prevents the risk of accumulating $CO_2$. Furthermore, the viral particle filters at the exhaust ports effectively extract viral particles and virus-laden droplets from the air passed through them, preventing further viral spread to the environment. In addition, the dimensions of the VEIL provide better mobility and patient comfort, factors which are limited in the case of CPAP "bubble" helmets or SCUBA masks. Finally, the volume of the VEIL provides an additional safety factor in case of suction failure, as $CO_2$ accumulation in this large enclosed volume is relatively slow compared to the far smaller volume of "bubble" helmets and SCUBA masks.

Nasal high airflow (NHF) may provide clinical benefits to patients with hypoxemic respiratory failure due to COVID-19 infection [218]. The VEIL enables its use for this purpose in long-term therapy, and has the potential to reduce rates of intubation [219], re-intubation [221, 229] and mortality [219, 220] in critically ill patients with acute hypoxemic respiratory failure secondary to COVID-19. The polycarbonate plastic is chemically resistant, easy to disinfect, and reusable. The VEIL is compatible with standard hospital beds and changes in bed incline. While this enclosure was developed in light of COVID-19, it is broadly applicable for reducing transmission of other droplet or aerosol-transmitted pathogens.

## 8.6 Acknowledgements

The authors are grateful to the Office of Naval Research (Grant N00014–20–P–2007), Kratos Defense and Security Solutions (Gift R–86X16–VX16), Professor Shu Chien for his kind gift in support of this research via the UCSD Rapid Response GEM COVID-19 grant, and the University of California San Diego for provision of funds and facilities in support of this work. This work was performed in part at the Medically Advanced Devices Laboratory at the University of California, San Diego and the Prototyping Laboratory, Qualcomm Institute. The authors would also like to thank the staff at the University of California San Diego School of Medicine for assisting with testing.

**Chapter 8** is entirely based on the material that is published in *Infection Control and Hospital Epidemiology* (2021), authored by Gopesh Tilvawala, Alex Grant, Jessica Wen, Teresa Wen, Ernesto Criado-Hidalgo, William Connacher, James Friend, and Timothy Morris [6]. The dissertation author was responsible for the device design, machining, assembly, experiments and image processing of the videos.

# Chapter 9

# Remarks and potential future directions

## 9.1 Micro-scale soft robotic devices

### 9.1.1 Qualitative and quantitative metrics for steering

While there exists some framework such as the IC$^3$ST scheme [42] for assessing catheter performance, none include the objective assessment of tip motion, stability, or steerability. To address this, a comprehensive plan including both qualitative and quantitative metrics with an experimental matrix to compare the performance of the steerable catheter to the current gold-standard microcatheters has been developed. These include:

- Navigating to the location, including forward pressure on the steerable tool, occlusive risk, and catastrophic failure events (structure dissection, trauma, perforation);
- Placement in the desired location, including location of tip, angle of device (needle, forcep, stent, wire) deployment;
- Device utility, including procedure time and procedure yield;

- Human factors pertaining to willingness to adopt, including device reliability, ease of use, motion (clumsy/smooth), ability to maintain steerable tip in fixed position after release, device responds as intended.

Interventionists of varying skill levels (4 skill levels, 2 interventionists per skill level, skill levels will be defined by number of procedures performed) will each attempt to perform procedures using 3 methods:

- Current gold-standard method
- Steerable tool system without steering
- Steerable tool system utilizing all steering capabilities as designed

The order in which interventionists will perform the procedures will be randomized. A case report form to record defined metrics will be created. Each procedure will be recorded via high resolution video to aid in tracking steerable tip motions and human interventions. Sentiment analysis with word lists will be used to assess subjective metrics via a Likert-scale survey of each neurointerventionist on design words: “sticky”, “smooth”,“flexible”,“stiff” and so on for both the existing catheters and our novel steerable tools. These words will be quantified through utility analysis [230], a classic engineering design technique applied to surgical devices. Interventionists will be asked to fill out a paper survey with these word lists. The quantities from utility analysis can tell us why there is an improvement in device performance if it exists, and what can be done to achieve further improvement.

The collection of these metrics will provide comprehensive and quantified assessment of the ability of the steerable tools to improve endovascular interventions, and to obtain an understanding as to *why* this improvement occurs.

### 9.1.2 Additional applications

The working principles of the steerable microcatheter system previously assessed for use in neurointervention can be extrapolated to address additional applications in interventional cardiology and interventional pulmonology. Steerable tools for these indications will enable navigating to target locations quicker, with higher precision, and provide diagnosis or treatment more effectively. The existing approach can be used to design, fabricate, and generate performance data and enable varying the diameters and stiffness of the steerable catheters to target additional disease indications. This would further enable investigating and expanding the steerable tool set to include additional devices such as wires or biopsy needles. This will facilitate the broader pursuit of dexterous microsurgical tools ultimately paving the way for improved patient outcomes and recovery times, and reduced procedure times and healthcare costs.

### 9.1.3 Clinical Background and Relevance

In **interventional cardiology**, precise positioning of the catheter tip remains a challenge due to the dynamic and complex three dimensional environment of the beating heart [61, 126]. Targeted ablation procedures, known to be an effective treatment for cardiac arrhythmias such as atrial fibrillation [231], require navigating catheters through tortuous vasculature and the cardiac chambers to access one or several specific ablation target sites. Moving and placing wires and catheters into specific regions of the heart requires manual guidance from skilled and experienced interventionists. In addition, continuous beating of the heart in conjunction with respiration poses significant challenges with stability in certain target cardiac regions [232]. Challenges with precise positioning result in prolonged X-ray exposure for both the patient and the medical staff. Randomized controlled trials have demonstrated that the use of steerable sheaths in procedures such as ablation for atrial fibrillation results in reduced procedure time and X-ray exposure as well as improved single procedure success rates likely due to improved precision of ablation target access [120]. Comparative studies between steerable and non-steerable catheters have also demonstrated significant reductions in procedure time and improvements in patient safety in patent foramen ovale closure and mitral valve repair [121–123]. Steerable catheters have also been demonstrated to yield better positioning of sophisticated implants in atrial septal defect repair and mitral valve clipping [124, 125]. Although steerable sheaths are now commonly used, some limitations remain [126]. Commercially available steerable sheaths are typically no smaller than 8F, and deflection is limited to a single plane [126]. Steerable catheters are a potential solution, though are not yet widely available. With an increasing incidence of vascular disease, advancements in coronary interventions, and increasing complexity of cardiac lesions, addressing the limitations of steerable tools in interventional cardiac procedures may allow for further improvement of accuracy in target access as well as enable percutaneous coronary interventions in previously challenging situations including complex stenoses, tortuous and narrowed coronary vessels, and chronic total occlusions [233, 234].

In **interventional pulmonology**, bronchoscopy is utilized in transbronchial biopsy procedures to sample lung nodules or masses to evaluate for malignancy or parenchymal lung diseases as early as possible. Existing bronchoscopes are too large to access subsegmental bronchi that get progressively smaller distally and peripherally. Navigating through acutely angled bronchi to reach nodules in the peripheral lungs can be challenging as physicians must utilize navigational bronchoscopy systems and steerable guides to reach the target location in the lung [235]. Although comparative studies have demonstrated that navigational bronchoscopy results in better performance within acutely angled bronchi in cadaveric lungs [236], once this target area is reached, pulmonologists must remove steerable guides and rely on extended working catheters or channels with preshaped tips that are not steerable and cannot be maneuvered in the three dimensional space of the airway. This results in suboptimal yield if the working catheter or channel lumen opening does not directly align with the target, even though the tip is in close proximity to the target location; biopsy devices such as needles or forceps, the majority of which are also not steerable, must be aligned appropriately towards the target to obtain an adequate sample [235, 236]. Collecting diagnostic samples at distal airways remains challenging today despite advances in navigational bronchoscopy [237]. Due to these limitations, a number of lung cancer patients fail to receive definite diagnosis and require repeat or more invasive biopsy procedures [235].

### 9.1.4 Proposed steerable tools

Providing interventionists with the ability to precisely steer the distal tip of endovascular and endoscopic tools has the potential to improve single-procedure success rates and outcomes of interventions and procedures requiring small maneuvers in confined environments of small-diameter structures. The basis of the prelminary work established by the neurovascular catheter recognizes that microballoons are routinely and safely used in various interventional procedures, representing a crude form of soft robotics [80]. Incorporating novel microprint-and-cast fabrication techniques and new hyperelastic polymers with microballoon technologies, as we previously done for neurointervention, will facilitate the creation of a suite of novel, inexpensive, safe steerable tools for use in endovascular and endoscopic applications for use in a variety of interventions and procedures at sub-centimeter and sub-millimeter scales.

### 9.1.5 Prelminary future work

To demonstrate that the approach is not limited to steering, the fabrication method decribed in Chapter 4 was used to fabricate actuators with different configurations: a spiral channel to perform localized torquing (Figure 9.1), multiple tentacles off-set from the center to perform micro-grabbing (Figure 9.2).

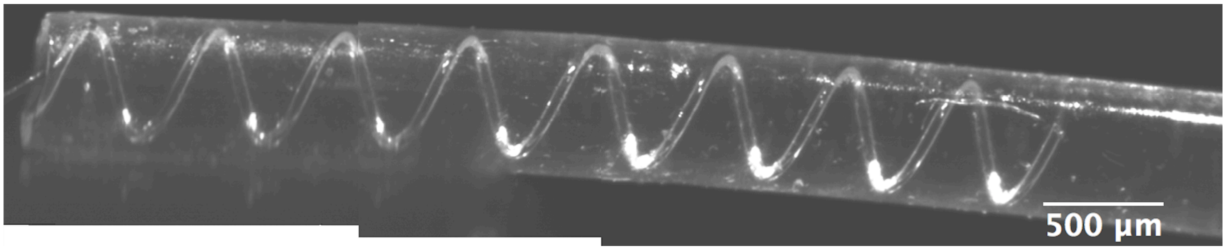

**Figure 9.1**: Image of a soft-tip enclosing a helical shaped hydraulic channel.

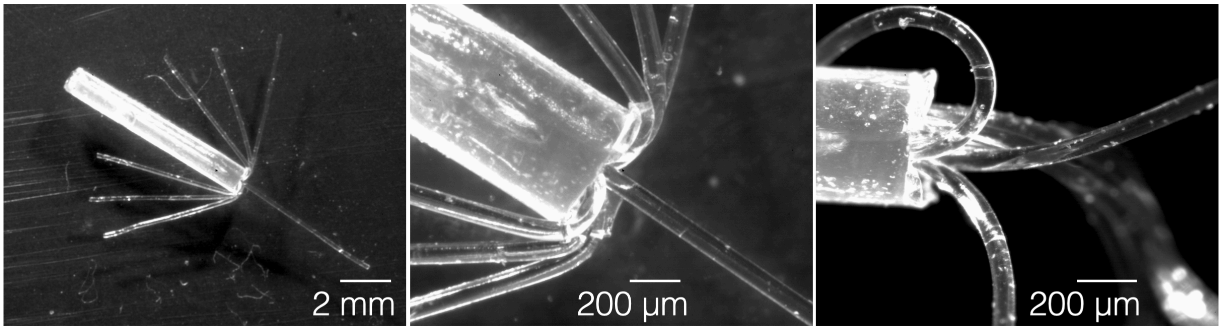

**Figure 9.2**: Image of tentacle structures for potential application in micro-gripping and manipulation. Each tentacle has a diameter of 100 $\mu$m.

While these early stage concepts would take long to translate into clinical application, with the knowledge and experience gained from the neurovascular device, the process would be significantly expedited.

## 9.2 Intraocular pressure measurement

Chapter 7 describes a novel direct IOP measurement device that provides rapid and accurate measurements and is independent of the cornea. The device is ergonomic, hand held, and has a disposable needle and sensor that can be discarded after use. The device was tested *ex vivo* in rabbits and accurately measured IOP in the anterior chamber and vitreous chamber of vitrectomized eyes, the results were published in early 2020 [5]. A key outcome of the research study was the inability to measure IOP in the vitreous chamber without vitrectomy because vitreous rapidly clogged the measurement needle, voiding the sensor reading. A similar result was found in prior cannulation studies. [199].

The research and design methods methods described there can be extrapolated to obtain rapid and accurate readings of IOP in the vitreous chamber. In the future pressure sensing device that enables rapid and accurate measurement of intraocular pressure in the vitreous chamber of the eye can be developed. The key requirements are to obtain readings that are not dependent on the mechanical properties of the cornea and performance would not be hampered by clogging of the vitreous. This would be done by attaching a micro-pressure sensor at the tip of a 33-Gauge needle as opposed to the back. This would enable measuring pressure changes at the location of the sensor and not via a fluid column in the syringe needle as measured previously.

## 9.3 Barrier enclosures for to prevent viral contagion while administering non-invasive ventilation therapy

The barrier enclosure described in Chapter 8 is effective in preventing viral contagion of infectious diseases. However, further studies are needed to ensure temperature control and safe evacuation of viral particles from the enclosure. Although the vacuum exhaust flow rate is higher than the expiratory capacity of a person, the ambient temperature, humidity and carbon dioxide levels within the enclosure have to be quantitative measured. This is not only important to ensure patient safety and comfort but also for more widespread use and clinical adoption. In addition to this, the time period after which the viral particle filters would be too clogged or ineffictive due to humidity build up is unknown. A potential future study is to monitor these parameters and make any design alterations needed to ensure the enclosures safety and efficacy can be further consolidated.

# Appendix A

# Supplementary information for biaxial membrane tests

Plots for the experimental and analytically obtained curves of best fit for the dimensional and dimensionless data.

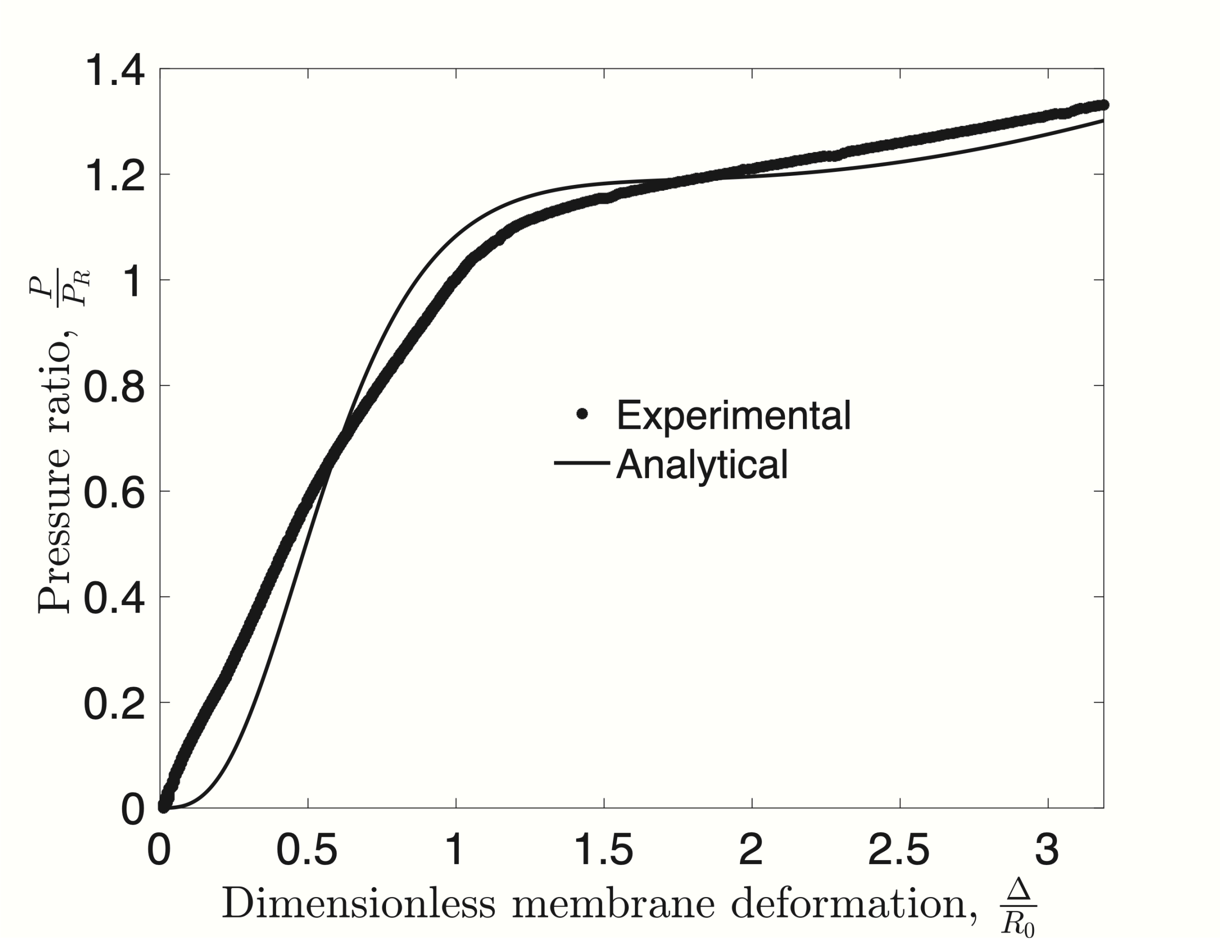

**Figure A.1**: Dimensionless inflation pressure, $P/P_R$ plotted with respect to the dimensionless deformation of the membrane, $\Delta/R_0$ for Dragon-Skin™ with the analytically obtained best fit. $\alpha = 0.07$, $R^2 = 0.94$.

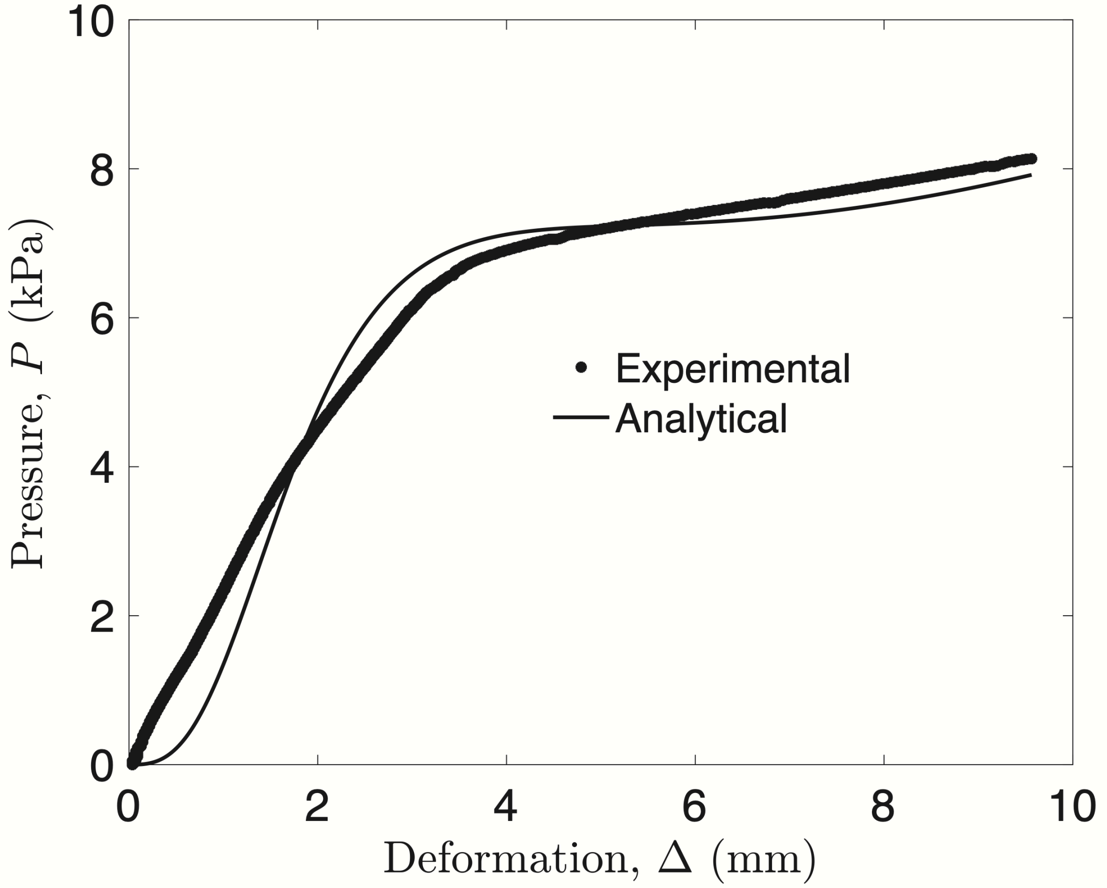

**Figure A.2**: Dimensional inflation pressure, $P$ as a function of the maximum deformation of the membrane, $\Delta$ for Dragon-Skin™, with the analytically obtained best fit. $R^2 = 0.94$.

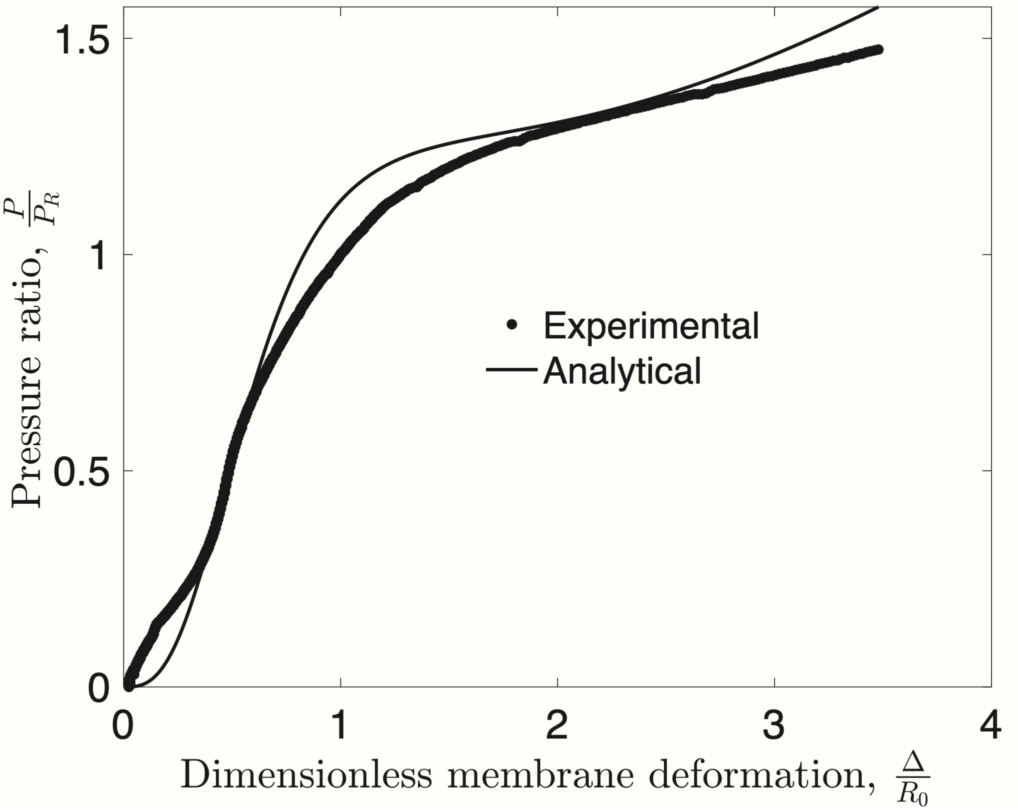

**Figure A.3**: Dimensionless inflation pressure, $P/P_R$ plotted with respect to the dimensionless deformation of the membrane, $\Delta/R_0$ for Dragon-Skin™ + Hexane (1:1, by weight) with the analytically obtained best fit. $\alpha = 0.08$, $R^2 = 0.98$.

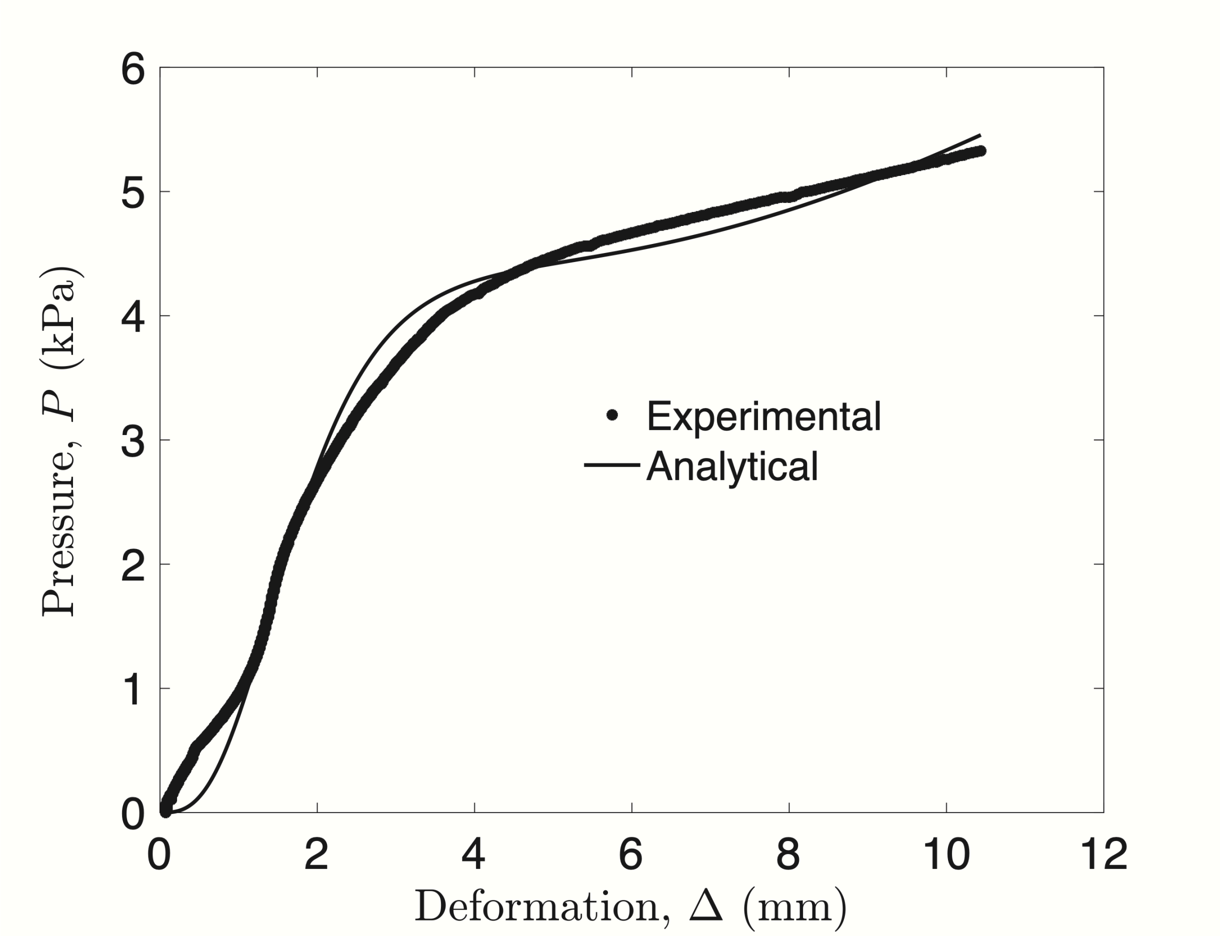

**Figure A.4**: Dimensional inflation pressure, $P$ (y-axis) as a function of the maximum deformation of the membrane, $\Delta$ (x-axis) for Dragon-Skin™ + Hexane (1:1, by weight) with the analytically obtained best fit. $R^2 = 0.98$.

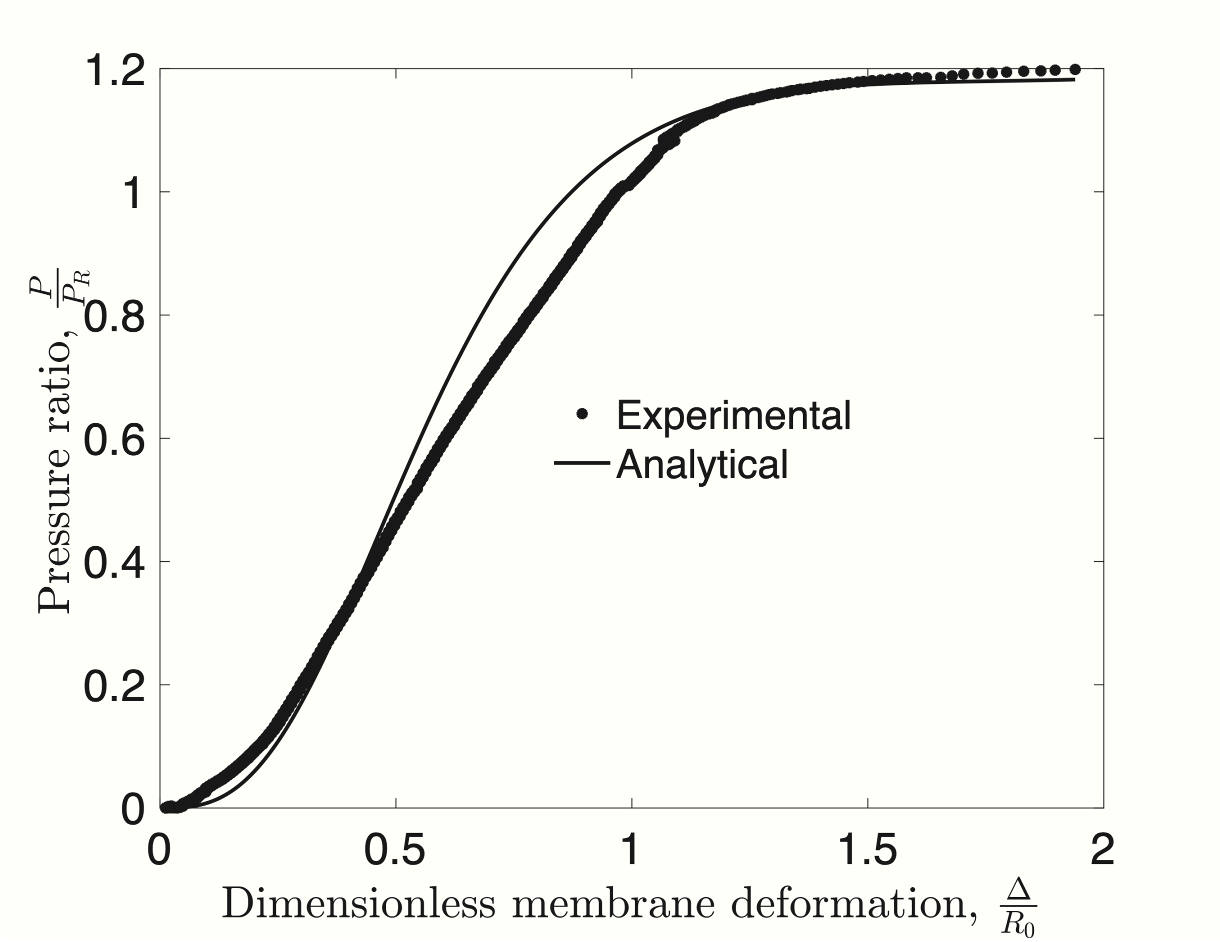

**Figure A.5**: Dimensionless inflation pressure $P/P_R$ plotted with respect to the dimensionless deformation of the membrane, $\Delta/R_0$ for Sorta-Clear™ with the analytically obtained best fit. $\alpha = 0.06$, $R^2 = 0.98$.

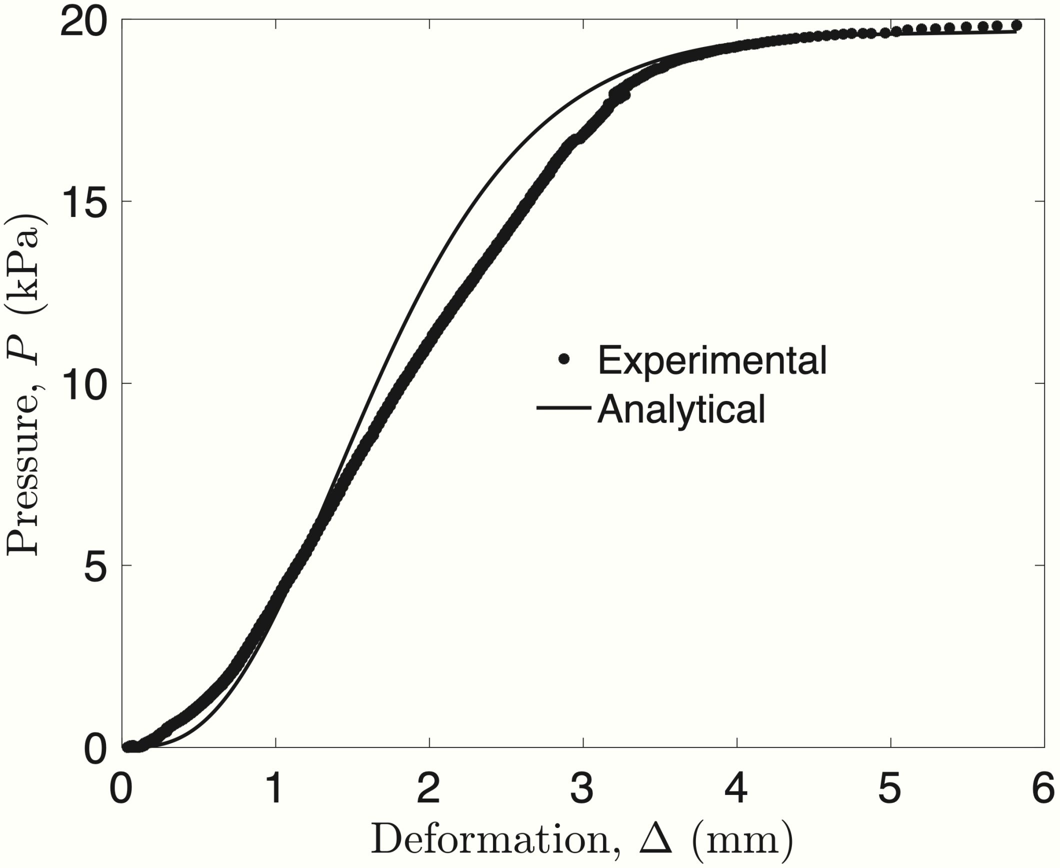

**Figure A.6**: Dimensional inflation pressure, $P$ (y-axis) as a function of the maximum deformation of the membrane, $\Delta$ (x-axis) for Sorta-Clear™ with the analytically obtained best fit. $R^2 = 0.98$.

$R^2$ values for the dimensionless and dimensional data for all five materials tested are provided in Table A.1.

**Table A.1**: $R^2$ values obtained through minimization of the least squared error comparing the analytical and experimental data.

| Material | $R^2$ Dimensionless | $R^2$ Dimensional |
|---|---|---|
| Dragon-Skin™10 | 0.94 | 0.94 |
| Ecoflex™ | 0.91 | 0.90 |
| Sorta-Clear™40 | 0.98 | 0.98 |
| Sylgard™184 (PDMS) | 0.99 | 0.99 |
| Dragon-Skin™10 + Hexane(1:1) | 0.98 | 0.98 |

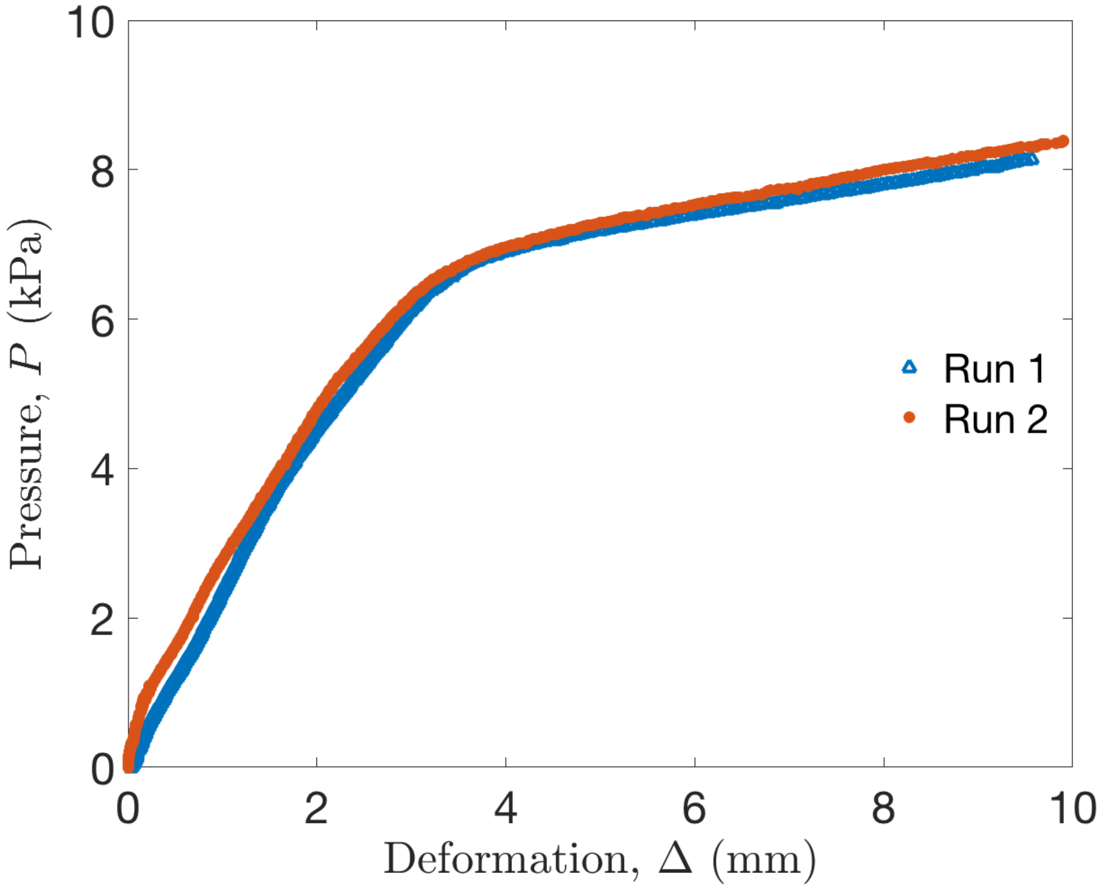

**Figure A.7**: Dimensional inflation pressure, $P$ (y-axis) as a function of the maximum deformation of the membrane, $\Delta$ (x-axis) for Dragon-Skin™ for separate experiments with the same material.

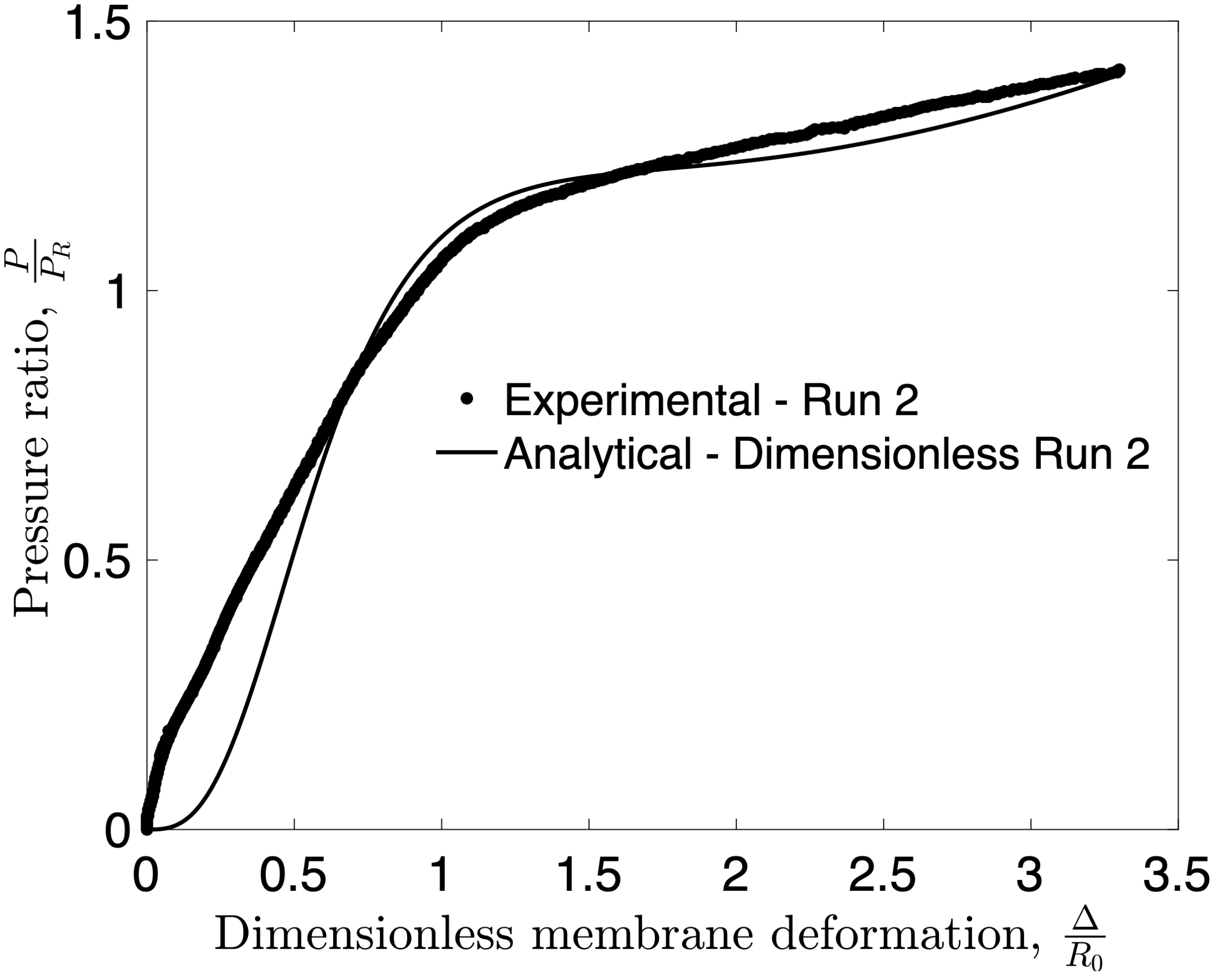

**Figure A.8**: Dimensionless inflation pressure $P/P_R$ plotted with respect to the dimensionless deformation of the membrane, $\Delta/R_0$ for Dragon-Skin™ with the analytically obtained best fit. $\alpha = 0.072$, $R^2 = 0.95$. *Repeat run*

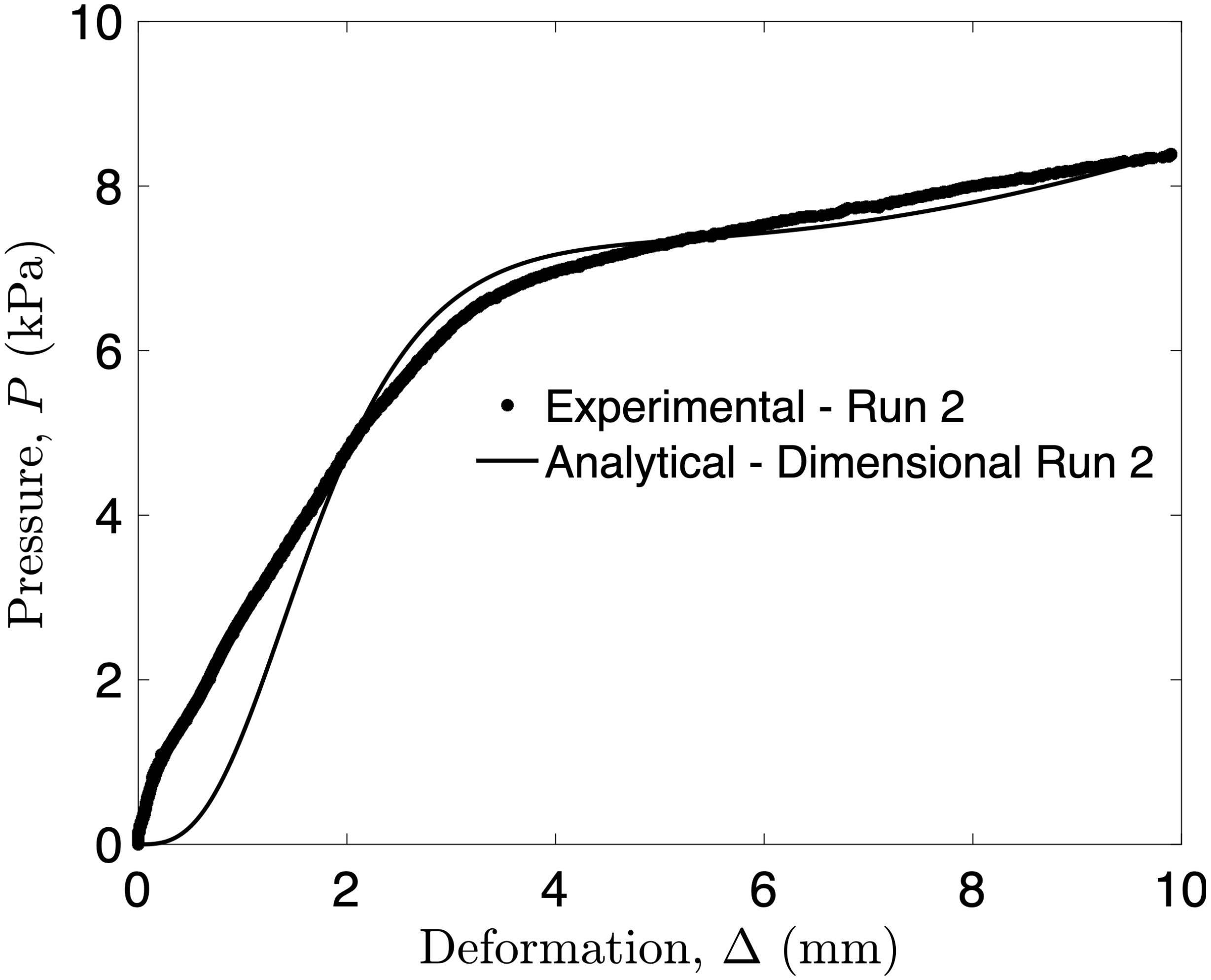

**Figure A.9**: Dimensional inflation pressure, $P$ (y-axis) as a function of the maximum deformation of the membrane, $\Delta$ (x-axis) for Dragon-Skin™ with the analytically obtained best fit. $R^2 = 0.95$. $C_1 = 177.5$ kPa, $C_2 = 12.78$ kPa *Repeat run.*

# Appendix B

# Fabrication steps for the VEIL - vacuum exhausted isolation locker

There are two versions of this enclosure. One that fits on a standard sized gurney and one that fits on a conventional hospital bed.

The only dimension that changes is the width at the base. A 1/8" thick polycarbonate sheet was pre-cut using a table router to the following shapes:

1. Gurney measures: Show side by side of flat sheet and 3D

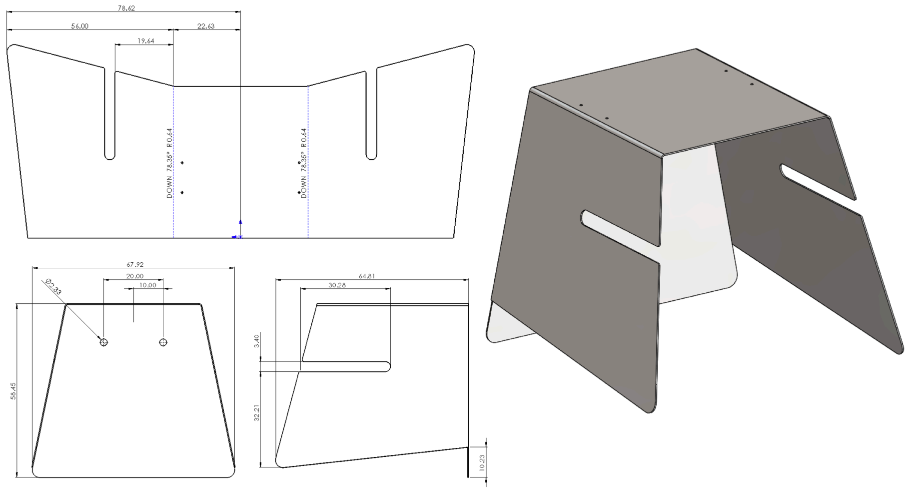

**Figure B.1**: Dimensional drawing and 3D illustration of gurney version

2. Hospital bed measures: Show side by side of flat sheet and 3D

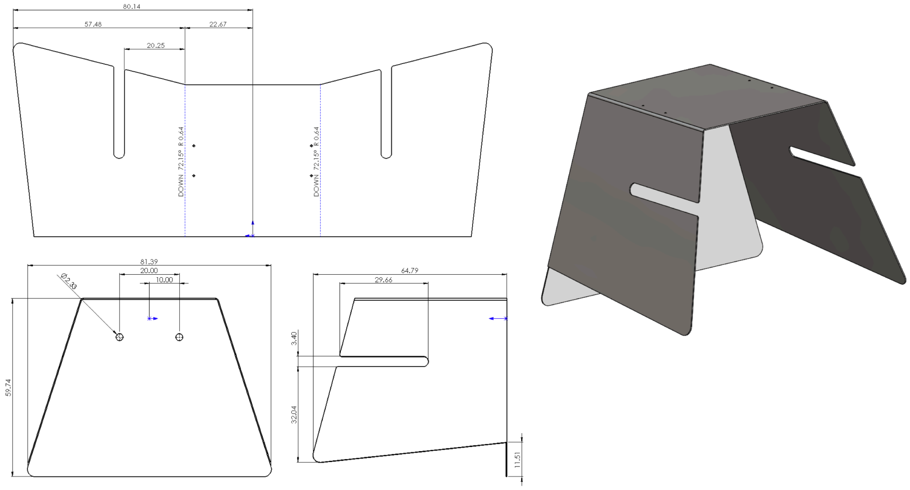

**Figure B.2**: Dimensional drawing and 3D illustration of hospital bed version

3. Using a thermo-bender, heat was precisely applied along the bend lines shown in Figure B.1 and B.2.

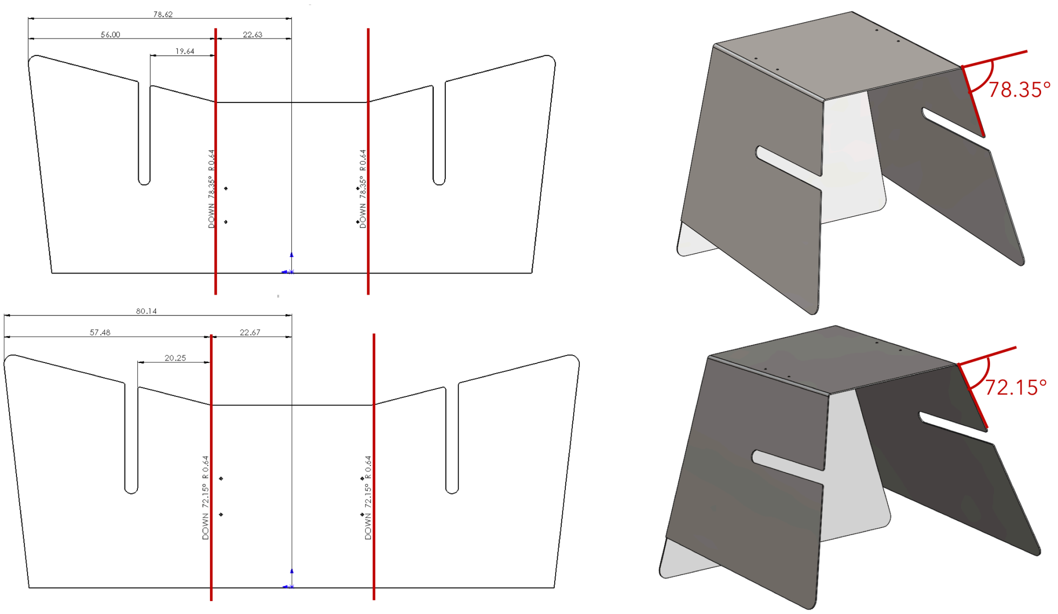

**Figure B.3**: Dimensional drawing and 3D illustration of hospital bed version

Tip: The flat pre-cut polycarbonate piece with the exhaust holes can be used as the limiting bend angle.

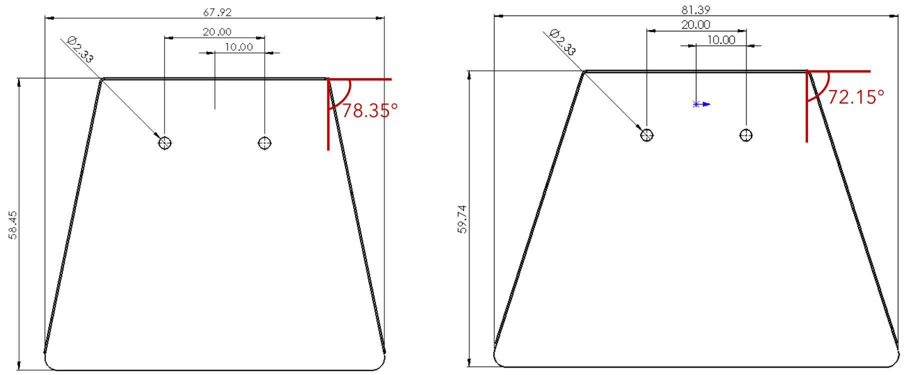

**Figure B.4**: Angle on the back piece with enhaust holes

4. The edges were sealed with clear plastic adhesive (Weld-on SC 16, Compton, CA, Mc-Master part no: 7515A11)

5. Worbla sheets (Eplastics SKU: WORBLACLR39X59) were cut into dimensions shown in Figure B.1 and B.2. The side panel pattern was traced and cut into the worbla sheet. The slit at the bottom enables access for HFNC or BiPAP tubing

**Figure B.5**: Worbla sheet side panel cutting pattern

6. The worbla side panels were attached using an instant-bond plastic adhesive Loctite 495 (McMaster part no: 7520A12) along the top and the sides of the access slot.

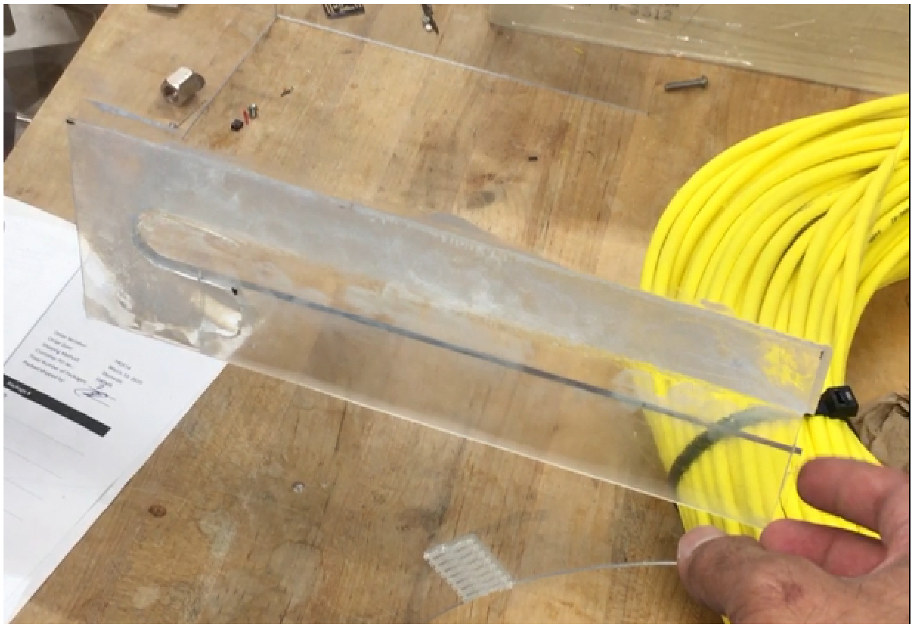

**Figure B.6**: Image of the worbla sheet side panels attached

7. DRAPE: Clear chemical resistant PVC film (0.008" thick, McMaster part no: 8562K17z)

was cut to the following dimensions

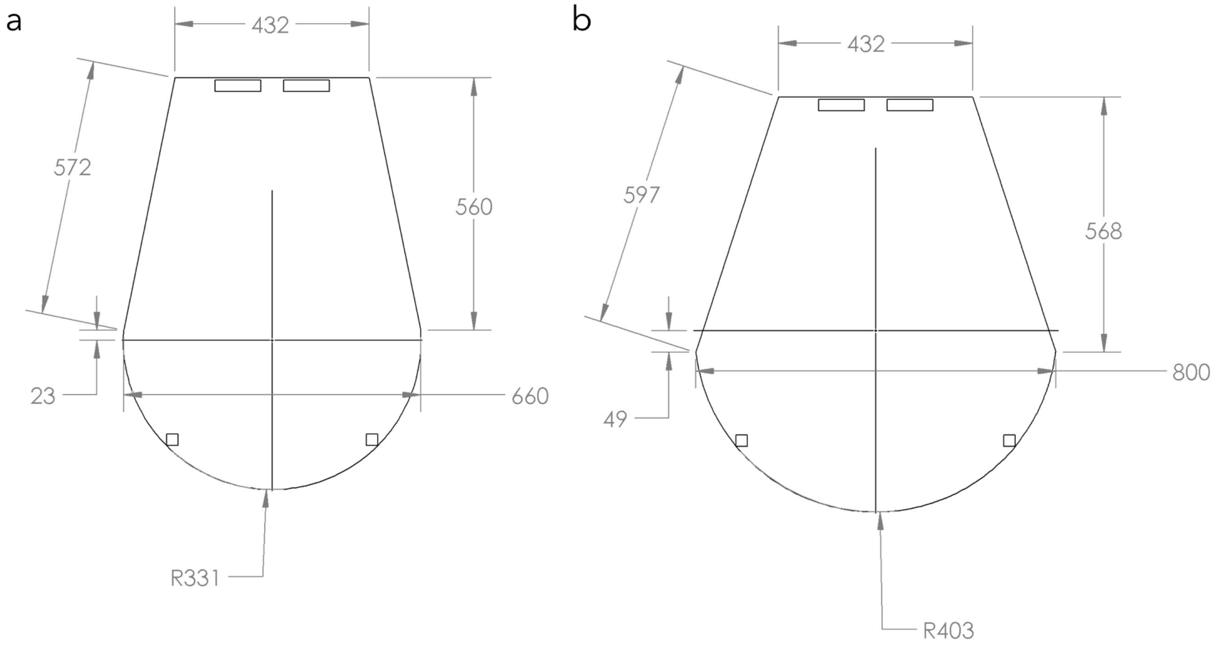

**Figure B.7**: Dimensions of the drapes. a) Gurney version, b) Hospital bed version

8. Adhesive backed snap together clear polycarbonate fastener 1" (W) (McMaster part no: 94935K17) was cut to lengths of 4". These were placed at 1" on both sides of the top mid-point of the drape. The design enables quick snap attachment and release with matching clear polycarbonate fasteners on the top of the box.
9. Side-skirts: Clear chemical resistant PVC film (0.008" thick) was cut to triangular shape with the following dimensions:

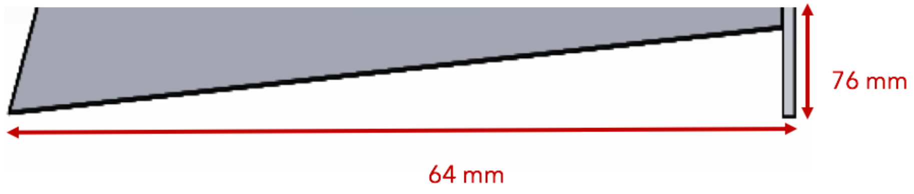

**Figure B.8**: Image of the side skirts dimensions and then final image attached on the box on the right

These were sealed to the sides of the enclosure using Loctite 495 to ensure a flexible seal while it is placed on the hospital bed.

10. Two multi adaptors 15 mm I.D. × 22 mm O.D. were placed into the exhaust holes. These enable easy plug in, plug out of the virus particle filters attached at the back.

# Bibliography

[1] M. De Volder and D. Reynaerts, “Pneumatic and hydraulic microactuators: a review,” *Journal of Micromechanics and Microengineering*, vol. 20, no. 4, p. 043001, 2010.

[2] P. Fabian, J. J. McDevitt, W. H. DeHaan, R. O. Fung, B. J. Cowling, K. H. Chan, G. M. Leung, and D. K. Milton, “Influenza virus in human exhaled breath: an observational study,” *PloS One*, vol. 3, no. 7, 2008.

[3] G. R. Johnson and L. Morawska, “The mechanism of breath aerosol formation,” *Journal of Aerosol Medicine and Pulmonary Drug Delivery*, vol. 22, no. 3, pp. 229–237, 2009.

[4] T. Gopesh and J. Friend, “Facile analytical extraction of the hyperelastic constants for the two-parameter mooney–rivlin model from experiments on soft polymers,” *Soft Robotics*, 2020.

[5] T. Gopesh, A. Camp, M. Unanian, J. Friend, and R. N. Weinreb, “Rapid and accurate pressure sensing device for direct measurement of intraocular pressure,” *Translational Vision Science & Technology*, vol. 9, no. 3, pp. 28–28, 2020.

[6] T. Gopesh, A. M. Grant, J. H. Wen, T. H. Wen, E. Criado-Hidalgo, W. J. Connacher, J. R. Friend, and T. A. Morris, “Vacuum exhausted isolation locker (veil) to reduce inpatient droplet/aerosol transmission during covid-19 pandemic,” *Infection Control & Hospital Epidemiology*, pp. 1–10.

[7] A. I. Qureshi, V. Janardhan, R. A. Hanel, and G. Lanzino, “Comparison of endovascular and surgical treatments for intracranial aneurysms: an evidence-based review,” *The Lancet Neurology*, vol. 6, no. 9, pp. 816–825, 2007.

[8] G. J. Rinkel, M. Djibuti, A. Algra, and J. Van Gijn, “Prevalence and risk of rupture of intracranial aneurysms a systematic review,” *Stroke*, vol. 29, no. 1, pp. 251–256, 1998.

[9] M. H. Vlak, A. Algra, R. Brandenburg, and G. J. Rinkel, “Prevalence of unruptured intracranial aneurysms, with emphasis on sex, age, comorbidity, country, and time period: a systematic review and meta-analysis,” *The Lancet Neurology*, vol. 10, no. 7, pp. 626–636, 2011.

[10] Brain Aneurysm Foundation, "Brain aneurysm statistics." `https://bafound.org/about-brain-aneurysms/brain-aneurysm-basics/brain-aneurysm-statistics-and-facts/`, 2020.

[11] R. J. Singer, C. S. Ogilvy, and G. Rordorf, "Etiology, clinical manifestations, and diagnosis of aneurysmal subarachnoid hemorrhage," *UpToDate. Waltham, MA*, 2012.

[12] R. D. Brown and J. P. Broderick, "Unruptured intracranial aneurysms: epidemiology, natural history, management options, and familial screening," *The Lancet Neurology*, vol. 13, no. 4, pp. 393–404, 2014.

[13] Y. J. Zhang, V. Desai, O. Diaz, R. Klucznik, and G. Britz, "Brain aneurysms," in *Emergency Approaches to Neurosurgical Conditions*, p. 89—101, Springer, 2015.

[14] D. O. Wiebers, J. C. Torner, and I. Meissner, "Impact of unruptured intracranial aneurysms on public health in the united states.," *Stroke*, vol. 23, no. 10, pp. 1416–1419, 1992.

[15] S. Juvela, M. Porras, and O. Heiskanen, "Natural history of unruptured intracranial aneurysms: a long-term follow-up study," *Journal of Neurosurgery*, vol. 79, no. 2, pp. 174–182, 1993.

[16] S. Juvela, K. Poussa, H. Lehto, and M. Porras, "Natural history of unruptured intracranial aneurysms: a long-term follow-up study," *Stroke*, vol. 44, no. 9, pp. 2414–2421, 2013.

[17] R. Bonita and S. Thomson, "Subarachnoid hemorrhage: epidemiology, diagnosis, management, and outcome.," *Stroke*, vol. 16, no. 4, pp. 591–594, 1985.

[18] J. W. Hop, G. J. Rinkel, A. Algra, and J. van Gijn, "Case-fatality rates and functional outcome after subarachnoid hemorrhage a systematic review," *Stroke*, vol. 28, no. 3, pp. 660–664, 1997.

[19] G. Guglielmi, F. Viñuela, J. Dion, and G. Duckwiler, "Electrothrombosis of saccular aneurysms via endovascular approach: part 2: preliminary clinical experience," *Journal of Neurosurgery*, vol. 75, no. 1, pp. 8–14, 1991.

[20] G. Guglielmi, F. Viñuela, G. Duckwiler, J. Dion, P. Lylyk, A. Berenstein, C. Strother, V. Graves, V. Halbach, D. Nichols, *et al.*, "Endovascular treatment of posterior circulation aneurysms by electrothrombosis using electrically detachable coils," *Journal of Neurosurgery*, vol. 77, no. 4, pp. 515–524, 1992.

[21] G. Guglielmi, "History of endovascular endosaccular occlusion of brain aneurysms: 1965–1990," *Interventional Neuroradiology*, vol. 13, no. 3, pp. 217–224, 2007.

[22] B. G. Thompson, R. D. Brown, S. Amin-Hanjani, J. P. Broderick, K. M. Cockroft, E. S. Connolly, G. R. Duckwiler, C. C. Harris, V. J. Howard, S. C. C. Johnston, *et al.*, "Guidelines for the management of patients with unruptured intracranial aneurysms," *Stroke*, vol. 46, no. 8, pp. 2368–2400, 2015.

[23] A. J. Molyneux, R. S. Kerr, J. Birks, N. Ramzi, J. Yarnold, M. Sneade, J. Rischmiller, I. collaborators, *et al.*, "Risk of recurrent subarachnoid haemorrhage, death, or dependence and standardised mortality ratios after clipping or coiling of an intracranial aneurysm in the international subarachnoid aneurysm trial (isat): long-term follow-up," *The Lancet Neurology*, vol. 8, no. 5, pp. 427–433, 2009.

[24] A. J. Molyneux, J. Birks, A. Clarke, M. Sneade, and R. S. Kerr, "The durability of endovascular coiling versus neurosurgical clipping of ruptured cerebral aneurysms: 18 year follow-up of the uk cohort of the international subarachnoid aneurysm trial (isat)," *The Lancet*, vol. 385, no. 9969, pp. 691–697, 2015.

[25] O. Diaz and L. Rangel-Castilla, "Endovascular treatment of intracranial aneurysms," in *Handbook of Clinical Neurology*, vol. 136, pp. 1303–1309, Elsevier, 2016.

[26] M. A. Secretariat, "Coil embolization for intracranial aneurysms: an evidence-based analysis," *Ontario Health Technology Assessment Series*, vol. 6, no. 1, p. 1, 2006.

[27] L. Pierot and A. K. Wakhloo, "Endovascular treatment of intracranial aneurysms: current status," *Stroke*, vol. 44, no. 7, pp. 2046–2054, 2013.

[28] R. Khatri, S. A. Chaudhry, G. J. Rodriguez, M. F. K. Suri, S. M. Cordina, and A. I. Qureshi, "Frequency and factors associated with unsuccessful lead (first) coil placement in patients undergoing coil embolization of intracranial aneurysms," *Neurosurgery*, vol. 72, no. 3, pp. 452–458, 2013.

[29] L. Elijovich, R. T. Higashida, M. T. Lawton, G. Duckwiler, S. Giannotta, and S. C. Johnston, "Predictors and outcomes of intraprocedural rupture in patients treated for ruptured intracranial aneurysms: the carat study," *Stroke*, vol. 39, no. 5, pp. 1501–1506, 2008.

[30] D. Kocur, N. Przybyłko, P. Bażowski, and J. Baron, "Rupture during coiling of intracranial aneurysms: predictors and clinical outcome," *Clinical Neurology and Neurosurgery*, vol. 165, pp. 81–87, 2018.

[31] L. Peeling and D. Fiorella, "Balloon-assisted guide catheter positioning to overcome extreme cervical carotid tortuosity: technique and case experience," *Journal of Neurointerventional Surgery*, vol. 6, no. 2, pp. 129–133, 2014.

[32] R. Blanc, M. Piotin, C. Mounayer, L. Spelle, and J. Moret, "Direct cervical arterial access for intracranial endovascular treatment," *Neuroradiology*, vol. 48, no. 12, pp. 925–929, 2006.

[33] D. Orbach, C. Stamoulis, K. Strauss, J. Manchester, E. Smith, R. Scott, and N. Lin, "Neurointerventions in children: radiation exposure and its import," *American Journal of Neuroradiology*, vol. 35, no. 4, pp. 650–656, 2014.

[34] E. N. Kahn, J. J. Gemmete, N. Chaudhary, B. G. Thompson, K. Chen, E. G. Christodoulou, and A. S. Pandey, "Radiation dose reduction during neurointerventional procedures by modification of default settings on biplane angiography equipment," *Journal of NeuroInterventional Surgery*, pp. neurintsurg–2015, 2015.

[35] M. S. Pearl, C. Torok, J. Wang, E. Wyse, M. Mahesh, and P. Gailloud, "Practical techniques for reducing radiation exposure during cerebral angiography procedures," *Journal of Neurointerventional Surgery*, vol. 7, no. 2, pp. 141–145, 2015.

[36] L. Regli, A. Uske, and N. de Tribolet, "Endovascular coil placement compared with surgical clipping for the treatment of unruptured middle cerebral artery aneurysms: a consecutive series," *Journal of Neurosurgery*, vol. 90, no. 6, pp. 1025–1030, 1999.

[37] C. Raftopoulos, P. Mathurin, D. Boscherini, R. F. Billa, M. V. Boven, and P. Hantson, "Prospective analysis of aneurysm treatment in a series of 103 consecutive patients when endovascular embolization is considered the first option," *Journal of Neurosurgery*, vol. 93, no. 2, pp. 175–182, 2000.

[38] E. Levy, C. J. Koebbe, M. B. Horowitz, C. A. Jungreis, G. L. Pride, K. Dutton, A. Kassam, and P. D. Purdy, "Rupture of intracranial aneurysms during endovascular coiling: management and outcomes," *Neurosurgery*, vol. 49, no. 4, pp. 807–813, 2001.

[39] M. Sluzewski, J. A. Bosch, W. J. van Rooij, P. C. Nijssen, and D. Wijnalda, "Rupture of intracranial aneurysms during treatment with guglielmi detachable coils: incidence, outcome, and risk factors," *Journal of Neurosurgery*, vol. 94, no. 2, pp. 238–240, 2001.

[40] W. Kim, R. T. Gandhi, C. S. Peña, R. E. Tartaglione, M. L. Taubman, and B. T. Katzen, "Robotic system-assisted endovascular treatment of a dissection-related pseudoaneurysm of the celiac axis secondary to fibromuscular dysplasia," *Journal of Vascular Surgery Cases and Innovative Techniques*, vol. 2, no. 3, pp. 145–148, 2016.

[41] J. Bismuth, C. Duran, M. Stankovic, B. Gersak, and A. B. Lumsden, "A first-in-man study of the role of flexible robotics in overcoming navigation challenges in the iliofemoral arteries," *Journal of Vascular Surgery*, vol. 57, no. 2, pp. 14S–19S, 2013.

[42] C. V. Riga, N. J. Cheshire, M. S. Hamady, and C. D. Bicknell, "The role of robotic endovascular catheters in fenestrated stent grafting," *Journal of Vascular Surgery*, vol. 51, no. 4, pp. 810–820, 2010.

[43] L. P. Broadbent, C. J. Moran, A. Nehra, D. T. Cross, and C. P. Derdeyn, “Transfer of a self-expanding stent to a braided microcatheter with the aid of transcatheter illumination: Technical report and illustrative case,” *American Journal of Neuroradiology*, vol. 24, no. 8, pp. 1517–1519, 2003.

[44] H. Tillander, “Magnetic guidance of a catheter with articulated steel tip,” *Acta Radiologica*, vol. 35, no. 1, pp. 62–64, 1951.

[45] W. S. Trimmer, “Microrobots and micromechanical systems,” *Sensors and Actuators*, vol. 19, no. 3, pp. 267–287, 1989.

[46] S. Spearing, “Micro devices and micro systems, materials for,” in *Encyclopedia of Materials: Science and Technology* (K. J. Buschow, R. W. Cahn, M. C. Flemings, B. Ilschner, E. J. Kramer, S. Mahajan, and P. Veyssière, eds.), pp. 5580 – 5587, Oxford: Elsevier, 2001.

[47] M. S. Choi, Y.-S. Oh, S. W. Jang, J. H. Kim, W. S. Shin, H.-J. Youn, W. S. Jung, M. Y. Lee, and K. B. Seong, “Comparison of magnetic navigation system and conventional method in catheter ablation of atrial fibrillation: is magnetic navigation system is more effective and safer than conventional method?,” *Korean Circulation Journal*, vol. 41, no. 5, pp. 248–252, 2011.

[48] N. Gudino, J. Heilman, J. Derakhshan, J. Sunshine, J. Duerk, and M. Griswold, “Control of intravascular catheters using an array of active steering coils,” *Medical Physics*, vol. 38, no. 7, pp. 4215–4224, 2011.

[49] R. Rioux and T. V. Casey, “Magnetically steerable catheter assembly,” Mar. 12 2013. US Patent 8,394,091.

[50] S. W. Hetts, M. Saeed, A. Martin, P. Lillaney, A. Losey, E. J. Yee, R. Sincic, L. Do, L. Evans, V. Malba, *et al.*, “Magnetically-assisted remote controlled microcatheter tip deflection under magnetic resonance imaging,” *JoVE (Journal of Visualized Experiments)*, no. 74, pp. e50299–e50299, 2013.

[51] T. Liu and M. C. Çavuşoğlu, “Three dimensional modeling of an mri actuated steerable catheter system,” in *2014 IEEE International Conference on Robotics and Automation (ICRA)*, pp. 4393–4398, IEEE, 2014.

[52] T. Liu, N. L. Poirot, D. Franson, N. Seiberlich, M. A. Griswold, and M. C. Çavuşoğlu, “Modeling and validation of the three-dimensional deflection of an mri-compatible magnetically actuated steerable catheter,” *IEEE Transactions on Biomedical Engineering*, vol. 63, no. 10, pp. 2142–2154, 2015.

[53] J. Edelmann, A. J. Petruska, and B. J. Nelson, “Magnetic control of continuum devices,” *The International Journal of Robotics Research*, vol. 36, no. 1, pp. 68–85, 2017.

[54] X.-Z. Chen, M. Hoop, F. Mushtaq, E. Siringil, C. Hu, B. J. Nelson, and S. Pane, "Recent developments in magnetically driven micro-and nanorobots," *Applied Materials Today*, vol. 9, pp. 37–48, 2017.

[55] C. Chautems, A. Tonazzini, Q. Boehler, S. H. Jeong, D. Floreano, and B. J. Nelson, "Magnetic continuum device with variable stiffness for minimally invasive surgery," *Advanced Intelligent Systems*, p. 1900086, 2019.

[56] H.-W. Huang, M. S. Sakar, A. J. Petruska, S. Pané, and B. J. Nelson, "Soft micromachines with programmable motility and morphology," *Nature Communications*, vol. 7, p. 12263, 2016.

[57] Y. Zhu, D. S. Antao, R. Xiao, and E. N. Wang, "Real-time manipulation with magnetically tunable structures," *Advanced Materials*, vol. 26, no. 37, pp. 6442–6446, 2014.

[58] Y. Kim, G. A. Parada, S. Liu, and X. Zhao, "Ferromagnetic soft continuum robots," *Science Robotics*, vol. 4, no. 33, p. eaax7329, 2019.

[59] L. Di Biase, T. S. Fahmy, D. Patel, R. Bai, K. Civello, O. M. Wazni, M. Kanj, C. S. Elayi, C. K. Ching, M. Khan, *et al.*, "Remote magnetic navigation: human experience in pulmonary vein ablation," *Journal of the American College of Cardiology*, vol. 50, no. 9, pp. 868–874, 2007.

[60] A. Arya, G. Hindricks, P. Sommer, Y. Huo, A. Bollmann, T. Gaspar, K. Bode, D. Husser, H. Kottkamp, and C. Piorkowski, "Long-term results and the predictors of outcome of catheter ablation of atrial fibrillation using steerable sheath catheter navigation after single procedure in 674 patients," *Europace*, vol. 12, no. 2, pp. 173–180, 2009.

[61] D. Filgueiras-Rama, A. Estrada, J. Shachar, S. Castrejón, D. Doiny, M. Ortega, E. Gang, and J. L. Merino, "Remote magnetic navigation for accurate, real-time catheter positioning and ablation in cardiac electrophysiology procedures," *JoVE (Journal of Visualized Experiments)*, no. 74, p. e3658, 2013.

[62] H. Rafii-Tari, C. J. Payne, and G.-Z. Yang, "Current and emerging robot-assisted endovascular catheterization technologies: a review," *Annals of Biomedical Engineering*, vol. 42, no. 4, pp. 697–715, 2014.

[63] W. F. Muller, "Spring guide manipulator," July 1 1969. US Patent 3,452,740.

[64] J. G. Hammerslag and G. R. Hammerslag, "Steerable angioplasty device," May 1 1990. US Patent 4,921,482.

[65] B. Avitall, "Catheter deflection control," Aug. 15 1995. US Patent 5,441,483.

[66] D. Stevens-Wright, M. Russo, P. Nielsen, and P. Bertram, "Actuator for use with steerable catheter," Oct. 31 1995. US Patent 5,462,527.

[67] W. Feng, C. Chi, H. Wang, K. Wang, S. Guo, *et al.*, "Highly precise catheter driving mechanism for intravascular neurosurgery," in *Proceedings of the 2006 IEEE International Conference on Mechatronics and Automation*, pp. 990–995, IEEE, 2006.

[68] X. Guo, T. T. Tegg, and R. E. Stehr, "Deflectable catheter with distal deflectable segment," July 26 2011. US Patent 7,985,215.

[69] J. R. Watson, "Asymmetric dual directional steerable catheter sheath," Aug. 6 2013. US Patent 8,500,733.

[70] M. Konings, T. Van Leeuwen, W. T. M. Mali, and M. Viergever, "Torsion measurement of catheters using polarized light in a single glass fibre," *Physics in Medicine & Biology*, vol. 43, no. 5, p. 1049, 1998.

[71] I. M. Kelly and C. S. Boyd, "Buckling of the tethering catheter causes migration of a temporary caval filter to the right atrium," *Clinical Radiology*, vol. 54, no. 6, pp. 398–401, 1999.

[72] P. Bloss, W. Rothe, P. Wünsche, C. Werner, A. Rothe, G. D. Kneissl, W. Burger, and E. Rehberg, "Investigations of the pushability behavior of cardiovascular angiographic catheters," *Bio-Medical Materials and Engineering*, vol. 13, no. 4, pp. 327–343, 2003.

[73] M. D. Olson, N. Phreaner, J. L. Schuller, D. T. Nguyen, D. F. Katz, R. G. Aleong, W. S. Tzou, R. Sung, P. D. Varosy, and W. H. Sauer, "Effect of catheter movement and contact during application of radiofrequency energy on ablation lesion characteristics," *Journal of Interventional Cardiac Electrophysiology*, vol. 38, no. 2, pp. 123–129, 2013.

[74] R. A. Caldwell, J. E. Woodell, S. P. Ho, S. W. Shalaby, T. Boland, E. M. Langan, and M. Laberge, "In vitro evaluation of phosphonylated low-density polyethylene for vascular applications," *Journal of Biomedical Materials Research: An Official Journal of The Society for Biomaterials, The Japanese Society for Biomaterials, and The Australian Society for Biomaterials and the Korean Society for Biomaterials*, vol. 62, no. 4, pp. 514–524, 2002.

[75] J. Bismuth, E. Kashef, N. Cheshire, and A. B. Lumsden, "Feasibility and safety of remote endovascular catheter navigation in a porcine model," *Journal of Endovascular Therapy*, vol. 18, no. 2, pp. 243–249, 2011.

[76] P. Généreux, J. G. Webb, L. G. Svensson, S. K. Kodali, L. F. Satler, W. F. Fearon, C. J. Davidson, A. C. Eisenhauer, R. R. Makkar, G. W. Bergman, *et al.*, "Vascular complications after transcatheter aortic valve replacement: insights from the partner (placement of aortic transcatheter valve) trial," *Journal of the American College of Cardiology*, vol. 60, no. 12, pp. 1043–1052, 2012.

[77] R. West, G. Ellis, and N. Brooks, "Complications of diagnostic cardiac catheterisation: results from a confidential inquiry into cardiac catheter complications," *Heart*, vol. 92, no. 6, pp. 810–814, 2006.

[78] C.-H. Yun, L. Y. Yeo, J. R. Friend, and B. Yan, "Multi-degree-of-freedom ultrasonic micromotor for guidewire and catheter navigation: The neuroglide actuator," *Applied Physics Letters*, vol. 100, no. 16, p. 164101, 2012.

[79] X.-Z. Chen, J.-H. Liu, M. Dong, L. Müller, G. Chatzipirpiridis, C. Hu, A. Terzopoulou, H. Torlakcik, X. Wang, F. Mushtaq, *et al.*, "Magnetically driven piezoelectric soft microswimmers for neuron-like cell delivery and neuronal differentiation," *Materials Horizons*, vol. 6, no. 7, pp. 1512–1516, 2019.

[80] D. Trivedi, C. D. Rahn, W. M. Kier, and I. D. Walker, "Soft robotics: Biological inspiration, state of the art, and future research," *Applied Bionics and Biomechanics*, vol. 5, no. 3, pp. 99–117, 2008.

[81] D. Rus and M. T. Tolley, "Design, fabrication and control of soft robots," *Nature*, vol. 521, no. 7553, p. 467, 2015.

[82] C. Laschi, B. Mazzolai, and M. Cianchetti, "Soft robotics: Technologies and systems pushing the boundaries of robot abilities," *Science Robotics*, vol. 1, no. 1, p. eaah3690, 2016.

[83] P. Polygerinos, N. Correll, S. A. Morin, B. Mosadegh, C. D. Onal, K. Petersen, M. Cianchetti, M. T. Tolley, and R. F. Shepherd, "Soft robotics: Review of fluid-driven intrinsically soft devices; manufacturing, sensing, control, and applications in human-robot interaction," *Advanced Engineering Materials*, vol. 19, no. 12, p. 1700016, 2017.

[84] G. M. Whitesides, "Soft robotics," *Angewandte Chemie International Edition*, vol. 57, no. 16, pp. 4258–4273, 2018.

[85] G. Dogangil, B. Davies, and F. Rodriguez y Baena, "A review of medical robotics for minimally invasive soft tissue surgery," *Proceedings of the Institution of Mechanical Engineers, Part H: Journal of Engineering in Medicine*, vol. 224, no. 5, pp. 653–679, 2010.

[86] V. Vitiello, S.-L. Lee, T. P. Cundy, and G.-Z. Yang, "Emerging robotic platforms for minimally invasive surgery," *Biomedical Engineering, IEEE Reviews in*, vol. 6, pp. 111–126, 2013.

[87] M. Cianchetti, T. Ranzani, G. Gerboni, T. Nanayakkara, K. Althoefer, P. Dasgupta, and A. Menciassi, "Soft robotics technologies to address shortcomings in today's minimally invasive surgery: the stiff-flop approach," *Soft Robotics*, vol. 1, no. 2, pp. 122–131, 2014.

[88] C. Bergeles and G.-Z. Yang, "From passive tool holders to microsurgeons: safer, smaller, smarter surgical robots," *IEEE Transactions on Biomedical Engineering*, vol. 61, no. 5, pp. 1565–1576, 2014.

[89] S. Fusco, M. S. Sakar, S. Kennedy, C. Peters, R. Bottani, F. Starsich, A. Mao, G. A. Sotiriou, S. Pané, S. E. Pratsinis, *et al.*, "An integrated microrobotic platform for on-demand, targeted therapeutic interventions," *Advanced Materials*, vol. 26, no. 6, pp. 952–957, 2014.

[90] O. C. Jeong, S. Kusuda, T. Sakakibara, S. Konishi, and M. Nokata, "Pneumatic micro finger as endeffecter of robot," in *Micro-NanoMechatronics and Human Science, 2005 IEEE International Symposium on*, pp. 145–148, IEEE, 2005.

[91] O. C. Jeong and S. Konishi, "All pdms pneumatic microfinger with bidirectional motion and its application," *Journal of Microelectromechanical Systems*, vol. 15, no. 4, pp. 896–903, 2006.

[92] F. Ilievski, A. D. Mazzeo, R. F. Shepherd, X. Chen, and G. M. Whitesides, "Soft robotics for chemists," *Angewandte Chemie*, vol. 123, no. 8, pp. 1930–1935, 2011.

[93] R. V. Martinez, J. L. Branch, C. R. Fish, L. Jin, R. F. Shepherd, R. Nunes, Z. Suo, and G. M. Whitesides, "Robotic tentacles with three-dimensional mobility based on flexible elastomers," *Advanced Materials*, vol. 25, no. 2, pp. 205–212, 2013.

[94] R. F. Shepherd, F. Ilievski, W. Choi, S. A. Morin, A. A. Stokes, A. D. Mazzeo, X. Chen, M. Wang, and G. M. Whitesides, "Multigait soft robot," *Proceedings of the National Academy of Sciences*, vol. 108, no. 51, pp. 20400–20403, 2011.

[95] M. T. Tolley, R. F. Shepherd, B. Mosadegh, K. C. Galloway, M. Wehner, M. Karpelson, R. J. Wood, and G. M. Whitesides, "A resilient, untethered soft robot," *Soft Robotics*, vol. 1, no. 3, pp. 213–223, 2014.

[96] M. Wehner, R. L. Truby, D. J. Fitzgerald, B. Mosadegh, G. M. Whitesides, J. A. Lewis, and R. J. Wood, "An integrated design and fabrication strategy for entirely soft, autonomous robots," *Nature*, vol. 536, no. 7617, pp. 451–455, 2016.

[97] D. Parry and R. Brown, "The hydraulic mechanism of the spider leg," *Journal of Experimental Biology*, vol. 36, no. 2, pp. 423–433, 1959.

[98] M. Schwörer, M. Kohl, and W. Menz, "Fluidic microjoints based on spider legs," in *Conf. on New Actuators (Bremen)*, 1998.

[99] K. Suzumori, S. Iikura, and H. Tanaka, "Flexible microactuator for miniature robots," in *Micro Electro Mechanical Systems, 1991, MEMS'91, Proceedings. An Investigation of Micro Structures, Sensors, Actuators, Machines and Robots. IEEE*, pp. 204–209, IEEE, 1991.

[100] K. Suzumori, S. Iikura, and H. Tanaka, "Applying a flexible microactuator to robotic mechanisms," *Control Systems, IEEE*, vol. 12, no. 1, pp. 21–27, 1992.

[101] K. Suzumori, A. Koga, and H. Riyoko, "Microfabrication of integrated fmas using stereo lithography," in *Micro Electro Mechanical Systems, 1994, MEMS'94, Proceedings, IEEE Workshop on*, pp. 136–141, IEEE, 1994.

[102] K. Suzumori, A. Koga, F. Kondo, and R. Haneda, "Integrated flexible microactuator systems," *Robotica*, vol. 14, no. 05, pp. 493–498, 1996.

[103] S. Konishi, F. Kawai, and P. Cusin, "Thin flexible end-effector using pneumatic balloon actuator," *Sensors and Actuators A: Physical*, vol. 89, no. 1, pp. 28–35, 2001.

[104] N. Simaan, R. Taylor, and P. Flint, "A dexterous system for laryngeal surgery," in *Robotics and Automation, 2004. Proceedings. ICRA'04. 2004 IEEE International Conference on*, vol. 1, pp. 351–357, IEEE, 2004.

[105] W. Wei, K. Xu, and N. Simaan, "A compact two-armed slave manipulator for minimally invasive surgery of the throat," in *The First IEEE/RAS-EMBS International Conference on Biomedical Robotics and Biomechatronics, 2006. BioRob 2006.*, pp. 769–774, IEEE, 2006.

[106] D.-H. Kim, N. Lu, R. Ghaffari, Y.-S. Kim, S. P. Lee, L. Xu, J. Wu, R.-H. Kim, J. Song, Z. Liu, J. Viventi, B. de Graff, S.-M. Won, Y. Huang, B. Litt, and A. J. Rogers, "Materials for multifunctional balloon catheters with capabilities in cardiac electrophysiological mapping and ablation therapy," *Nature Materials*, vol. 10, no. 4, pp. 316–323, 2011.

[107] A. Ruzzu, K. Bade, J. Fahrenberg, and D. Maas, "Positioning system for catheter tips based on an active microvalve system," *Journal of Micromechanics and Microengineering*, vol. 8, no. 2, p. 161, 1998.

[108] H. Okayasu, J. Okamoto, M. G. Fujie, M. Umezu, and H. Iseki, "Development of a hydraulic-driven flexible manipulator for neurosurgery," in *International Congress Series*, vol. 1256, pp. 607–612, Elsevier, 2003.

[109] Y. Watanabe, M. Maeda, N. Yaji, R. Nakamura, H. Iseki, M. Yamato, T. Okano, S. Hori, and S. Konishi, "Small, soft, and safe microactuator for retinal pigment epithelium transplantation," in *Micro Electro Mechanical Systems, 2007. MEMS. IEEE 20th International Conference on*, pp. 659–662, IEEE, 2007.

[110] C. Pang, Y.-C. Tai, J. W. Burdick, and R. A. Andersen, "Electrolysis-based parylene balloon actuators for movable neural probes," in *Nano/Micro Engineered and Molecular Systems, 2007. NEMS'07. 2nd IEEE International Conference on*, pp. 913–916, IEEE, 2007.

[111] Y.-W. Lu and C.-J. C. Kim, "Microhand for biological applications," *Applied Physics Letters*, vol. 89, no. 16, p. 164101, 2006.

[112] J. Paek, I. Cho, and J. Kim, “Microrobotic tentacles with spiral bending capability based on shape-engineered elastomeric microtubes,” *Scientific Reports*, vol. 5, 2015.

[113] Y. Matsumura, A. E. Kovalev, and S. N. Gorb, “Penetration mechanics of a beetle intromittent organ with bending stiffness gradient and a soft tip,” *Science Advances*, vol. 3, no. 12, p. eaao5469, 2017.

[114] M. Madou and J. Florkey, “From batch to continuous manufacturing of microbiomedical devices,” *Chemical Reviews*, vol. 100, no. 7, pp. 2679–2692, 2000.

[115] M. J. Madou, *Fundamentals of Microfabrication and Nanotechnology*. CRC Press, 2011.

[116] M. J. Madou, *Fundamentals of Microfabrication: the Science of Miniaturization*. CRC press, 2018.

[117] Y. Fu, H. Liu, W. Huang, S. Wang, and Z. Liang, “Steerable catheters in minimally invasive vascular surgery,” *The International Journal of Medical Robotics and Computer Assisted Surgery*, vol. 5, no. 4, pp. 381–391, 2009.

[118] G.-Z. Yang, J. Bellingham, P. E. Dupont, P. Fischer, L. Floridi, R. Full, N. Jacobstein, V. Kumar, M. McNutt, R. Merrifield, *et al.*, “The grand challenges of science robotics,” *Science Robotics*, vol. 3, no. 14, p. eaar7650, 2018.

[119] A. Ali, A. Sakes, E. A. Arkenbout, P. Henselmans, R. van Starkenburg, T. Szili-Torok, and P. Breedveld, “Catheter steering in interventional cardiology: Mechanical analysis and novel solution,” *Proceedings of the Institution of Mechanical Engineers, Part H: Journal of Engineering in Medicine*, vol. 233, no. 12, pp. 1207–1218, 2019.

[120] C. Piorkowski, C. Eitel, S. Rolf, K. Bode, P. Sommer, T. Gaspar, S. Kircher, U. Wetzel, A. S. Parwani, L.-H. Boldt, *et al.*, “Steerable versus nonsteerable sheath technology in atrial fibrillation ablation: a prospective, randomized study,” *Circulation: Arrhythmia and Electrophysiology*, vol. 4, no. 2, pp. 157–165, 2011.

[121] J. M. Tobis and I. Abudayyeh, “New devices and technology in interventional cardiology,” *Journal of Cardiology*, vol. 65, no. 1, pp. 5–16, 2015.

[122] S. Hascoet, A. Fraisse, and M. Elbaz, “Successful percutaneous transcatheter patent foramen ovale closure through the right internal jugular vein using a steerable catheter,” *Catheterization and Cardiovascular Interventions*, vol. 82, no. 4, pp. E598–E602, 2013.

[123] F. Maisano, H. Vanermen, J. Seeburger, M. Mack, V. Falk, P. Denti, M. Taramasso, and O. Alfieri, “Direct access transcatheter mitral annuloplasty with a sutureless and adjustable device: preclinical experience,” *European Journal of Cardio-Thoracic Surgery*, vol. 42, no. 3, pp. 524–529, 2012.

[124] M. Nounou, A. Harrison, and M. Kern, “A novel technique using a steerable guide catheter to successfully deliver an amplatzer septal occluder to close an atrial septal defect,” *Catheterization and Cardiovascular Interventions*, vol. 72, no. 7, pp. 994–997, 2008.

[125] K. Tiroch, M. Vorpahl, and M. Seyfarth, “Novel mitral clipping technique overcoming extreme atrial dilatation,” *Catheterization and Cardiovascular Interventions*, vol. 84, no. 4, pp. 606–609, 2014.

[126] A. Ali, D. H. Plettenburg, and P. Breedveld, “Steerable catheters in cardiology: Classifying steerability and assessing future challenges,” *IEEE Transactions on Biomedical Engineering*, vol. 63, no. 4, pp. 679–693, 2016.

[127] S. J. Schreiber, S. Gottschalk, M. Weih, A. Villringer, and J. M. Valdueza, “Assessment of blood flow velocity and diameter of the middle cerebral artery during the acetazolamide provocation test by use of transcranial doppler sonography and mr imaging,” *American Journal of Neuroradiology*, vol. 21, no. 7, pp. 1207–1211, 2000.

[128] P. Huber and J. Handa, “Effect of contrast material, hypercapnia, hyperventilation, hypertonic glucose and papaverine on the diameter of the cerebral arteries: angiographic determination in man,” *Investigative Radiology*, vol. 2, no. 1, pp. 17–32, 1967.

[129] D. W. Muller and R. Spina, “Guiding catheters and wires,” *Cardiovascular Catheterization and Intervention: A Textbook of Coronary, Peripheral, and Structural Heart Disease*, p. 404, 2010.

[130] M. S. Noone, A. H. Dunfee, and M. S. Poole, “Multiple segment catheter and method of fabrication,” July 15 2003. US Patent 6,591,472.

[131] F. K. Hui, A. J. Schuette, A. M. Spiotta, J. Yim, N. Obuchowski, P. A. Rasmussen, M. S. Hussain, C. M. Cawley, J. E. Dion, and F. C. Tong, “Flexible tip guides and intermediate catheters: two center experience and a proposed taxonomy,” *Journal of Neurointerventional Surgery*, vol. 6, no. 8, pp. 618–623, 2014.

[132] G. P. Colby, L.-M. Lin, R. Xu, N. Beaty, M. T. Bender, B. Jiang, J. Huang, R. J. Tamargo, and A. L. Coon, “Utilization of a novel, multi-durometer intracranial distal access catheter: nuances and experience in 110 consecutive cases of aneurysm flow diversion,” *Interventional Neurology*, vol. 6, no. 1-2, pp. 90–104, 2017.

[133] C. Chautems, A. Tonazzini, D. Floreano, and B. J. Nelson, “A variable stiffness catheter controlled with an external magnetic field,” in *2017 IEEE/RSJ International Conference on Intelligent Robots and Systems (IROS)*, pp. 181–186, IEEE, 2017.

[134] G. Kampa and N. Geiger, “Method of making a tubular body for a catheter, sheath or lead,” Nov. 2 2010. US Patent 7,824,517.

[135] J. Burgner-Kahrs, D. C. Rucker, and H. Choset, "Continuum robots for medical applications: A survey," *IEEE Transactions on Robotics*, vol. 31, no. 6, pp. 1261–1280, 2015.

[136] L. A. Taber, *Nonlinear theory of elasticity: applications in biomechanics*. World Scientific, 2004.

[137] R. Hooke, "1678," *De Potentia restitutiva*, 1931.

[138] M. Mooney, "A theory of large elastic deformation," *Journal of Applied Physics*, vol. 11, no. 9, pp. 582–592, 1940.

[139] R. S. Rivlin and D. Saunders, "Large elastic deformations of isotropic materials vii. experiments on the deformation of rubber," *Philosophical Transactions of the Royal Society of London. Series A, Mathematical and Physical Sciences*, vol. 243, no. 865, pp. 251–288, 1951.

[140] R. W. Ogden, *Non-linear elastic deformations*. Courier Corporation, 1997.

[141] O. H. Yeoh, "Some forms of the strain energy function for rubber," *Rubber Chemistry and Technology*, vol. 66, no. 5, pp. 754–771, 1993.

[142] P. J. Blatz and W. L. Ko, "Application of finite elastic theory to the deformation of rubbery materials," *Transactions of the Society of Rheology*, vol. 6, no. 1, pp. 223–252, 1962.

[143] E. M. Arruda and M. C. Boyce, "A three-dimensional constitutive model for the large stretch behavior of rubber elastic materials," *Journal of the Mechanics and Physics of Solids*, vol. 41, no. 2, pp. 389–412, 1993.

[144] A. N. Gent and A. Thomas, "Forms for the stored (strain) energy function for vulcanized rubber," *Journal of Polymer Science*, vol. 28, no. 118, pp. 625–628, 1958.

[145] M. Sasso, G. Palmieri, G. Chiappini, and D. Amodio, "Characterization of hyperelastic rubber-like materials by biaxial and uniaxial stretching tests based on optical methods," *Polymer Testing*, vol. 27, no. 8, pp. 995–1004, 2008.

[146] E. K. Dimitriadis, F. Horkay, J. Maresca, B. Kachar, and R. S. Chadwick, "Determination of elastic moduli of thin layers of soft material using the atomic force microscope," *Biophysical Journal*, vol. 82, no. 5, pp. 2798–2810, 2002.

[147] A. Mata, A. J. Fleischman, and S. Roy, "Characterization of polydimethylsiloxane (pdms) properties for biomedical micro/nanosystems," *Biomedical Microdevices*, vol. 7, no. 4, pp. 281–293, 2005.

[148] D. C. Lin, E. K. Dimitriadis, and F. Horkay, "Elasticity models for the spherical indentation of gels and soft biological tissues," *MRS Online Proceedings Library Archive*, vol. 1060, 2007.

[149] A. C. Chang and B. H. Liu, “Modified flat-punch model for hyperelastic polymeric and biological materials in nanoindentation,” *Mechanics of Materials*, vol. 118, pp. 17–21, 2018.

[150] L.-H. Cai, T. E. Kodger, R. E. Guerra, A. F. Pegoraro, M. Rubinstein, and D. A. Weitz, “Soft poly (dimethylsiloxane) elastomers from architecture-driven entanglement free design,” *Advanced Materials*, vol. 27, no. 35, pp. 5132–5140, 2015.

[151] I. Johnston, D. McCluskey, C. Tan, and M. Tracey, “Mechanical characterization of bulk sylgard 184 for microfluidics and microengineering,” *Journal of Micromechanics and Microengineering*, vol. 24, no. 3, p. 035017, 2014.

[152] I. M. Ward and D. W. Hadley, *An introduction to the mechanical properties of solid polymers.* 1993.

[153] F. Mujika, N. Carbajal, A. Arrese, and I. Mondragon, “Determination of tensile and compressive moduli by flexural tests,” *Polymer Testing*, vol. 25, no. 6, pp. 766–771, 2006.

[154] T. Kawamura, K. Urayama, and S. Kohjiya, “Multiaxial deformations of end-linked poly (dimethylsiloxane) networks 5. revisit to mooney-rivlin approach to strain energy density function,” *Nihon Reoroji Gakkaishi*, vol. 31, no. 4, pp. 213–217, 2003.

[155] A. Selvadurai, “Deflections of a rubber membrane,” *Journal of the Mechanics and Physics of Solids*, vol. 54, no. 6, pp. 1093–1119, 2006.

[156] S.-H. Yoon, V. Reyes-Ortiz, K.-H. Kim, Y. H. Seo, and M. R. Mofrad, “Analysis of circular pdms microballoons with ultralarge deflection for mems design,” *Journal of Microelectromechanical Systems*, vol. 19, no. 4, pp. 854–864, 2010.

[157] V. Cârlescu, M. A. Rusu, G. Prisăcaru, and D. N. Olaru, “experimental characterization and fem simulation on uniaxial tensile and compression of dielectric elastomers,”

[158] R. Christensen and W. Feng, “Nonlinear analysis of the inflation of an initially flat, circular, elastic disk,” *Journal of Rheology*, vol. 30, no. 1, pp. 157–165, 1986.

[159] R. Rivlin, “Large elastic deformations of isotropic materials iv. further developments of the general theory,” *Philosophical Transactions of the Royal Society of London. Series A, Mathematical and Physical Sciences*, vol. 241, no. 835, pp. 379–397, 1948.

[160] A. Selvadurai and M. Shi, “Fluid pressure loading of a hyperelastic membrane,” *International Journal of non-Linear Mechanics*, vol. 47, no. 2, pp. 228–239, 2012.

[161] A. Gent, “Elastic instabilities in rubber,” *International Journal of non-Linear Mechanics*, vol. 40, no. 2-3, pp. 165–175, 2005.

[162] G. R. Bhashyam, "Ansys mechanicala powerful nonlinear simulation tool," *Ansys, Inc*, vol. 1, p. 39, 2002.

[163] H. Henkes, E. Miloslavski, S. Lowens, J. Reinartz, T. Liebig, and D. Kühne, "Treatment of intracranial atherosclerotic stenoses with balloon dilatation and self-expanding stent deployment (wingspan)," *Neuroradiology*, vol. 47, no. 3, pp. 222–228, 2005.

[164] K. Nakamura, M. Kurosawa, H. Kurebayashi, and S. Ueha, "An estimation of load characteristics of an ultrasonic motor by measuring transient responses," *IEEE Transactions on Ultrasonics, Ferroelectrics, and Frequency Control*, vol. 38, no. 5, pp. 481–485, 1991.

[165] A. S. Miranpuri, C. M. Nickele, E. Akture, K. Royalty, and D. B. Niemann, "Neuroangiography simulation using a silicone model in the angiography suite improves trainee skills," *Journal of Neurointerventional Surgery*, vol. 6, no. 7, pp. 561–564, 2014.

[166] P. Narra, J. Kuban, L. E. Grandpre, J. Singh, J. Barrero, and A. Norbash, "Videoscopic phantom-based angiographic simulation: effect of brief angiographic simulator practice on vessel cannulation times," *Journal of Vascular and Interventional Radiology*, vol. 20, no. 9, pp. 1215–1223, 2009.

[167] S. Konakondla, R. Fong, and C. M. Schirmer, "Simulation training in neurosurgery: advances in education and practice," *Advances in Medical Education and Practice*, vol. 8, p. 465, 2017.

[168] R. Kikinis, S. D. Pieper, and K. G. Vosburgh, "3d slicer: a platform for subject-specific image analysis, visualization, and clinical support," in *Intraoperative imaging and image-guided therapy*, pp. 277–289, Springer, 2014.

[169] S. Beucher *et al.*, "The watershed transformation applied to image segmentation," *Scanning microscopy supplement*, pp. 299–299, 1992.

[170] L. Zarrinkoob, K. Ambarki, A. Wåhlin, R. Birgander, A. Eklund, and J. Malm, "Blood flow distribution in cerebral arteries," *Journal of Cerebral Blood Flow & Metabolism*, vol. 35, no. 4, pp. 648–654, 2015.

[171] S.-N. H. Khan and A. J. Ringer, *Handbook of Neuroendovascular Techniques*. Springer, 2017.

[172] S. Seldinger, "A new technique: catheter replacement of the needle in percutaneous arteriography," *Acta Radiologica*, vol. 39, pp. 368–376, 1953.

[173] J. Joseph, K. CK Wong, M. R Ginks, Y. Bashir, T. R Betts, and K. Rajappan, "Steerable sheath technology in the ablation of atrial fibrillation," *Recent Patents on Cardiovascular Drug Discovery*, vol. 8, no. 3, pp. 171–177, 2013.

[174] J. Moret, C. Cognard, A. Weill, L. Castaings, and A. Rey, “Reconstruction technic in the treatment of wide-neck intracranial aneurysms. long-term angiographic and clinical results. apropos of 56 cases,” *Journal of Neuroradiology*, vol. 24, no. 1, pp. 30–44, 1997.

[175] M. A. Kass, “Standardizing the measurement of intraocular pressure for clinical research: guidelines from the eye care technology forum,” *Ophthalmology*, vol. 103, no. 1, pp. 183–185, 1996.

[176] M. M. Whitacre and R. Stein, “Sources of error with use of goldmann-type tonometers,” *Survey of Ophthalmology*, vol. 38, no. 1, pp. 1–30, 1993.

[177] B. A. Francis, A. Hsieh, M.-Y. Lai, V. Chopra, F. Pena, S. Azen, R. Varma, L. A. L. E. S. Group, *et al.*, “Effects of corneal thickness, corneal curvature, and intraocular pressure level on goldmann applanation tonometry and dynamic contour tonometry,” *Ophthalmology*, vol. 114, no. 1, pp. 20–26, 2007.

[178] F. A. Medeiros and R. N. Weinreb, “Evaluation of the influence of corneal biomechanical properties on intraocular pressure measurements using the ocular response analyzer,” *Journal of Glaucoma*, vol. 15, no. 5, pp. 364–370, 2006.

[179] J. M. Risma, S. Tehrani, K. Wang, J. H. Fingert, W. L. Alward, and Y. H. Kwon, “The utility of diaton tonometer measurements in patients with ocular hypertension, glaucoma, and glaucoma tube shunts: a preliminary study for its potential use in keratoprosthesis patients,” *Journal of Glaucoma*, vol. 25, no. 8, pp. 643–647, 2016.

[180] I. E. Araci, B. Su, S. R. Quake, and Y. Mandel, “An implantable microfluidic device for self-monitoring of intraocular pressure,” *Nature Medicine*, vol. 20, no. 9, p. 1074, 2014.

[181] E. I. Paschalis, F. Cade, S. Melki, L. R. Pasquale, C. H. Dohlman, and J. B. Ciolino, “Reliable intraocular pressure measurement using automated radio-wave telemetry,” *Clinical Ophthalmology (Auckland, NZ)*, vol. 8, p. 177, 2014.

[182] G. Williams, “Ivt injections: health policy implications,” *Rev Ophthalmol*, vol. 21, no. 6, pp. 62–64, 2014.

[183] K. Xu, E. K. Chin, S. R. Bennett, D. F. Williams, E. H. Ryan, S. Dev, R. A. Mittra, P. A. Quiram, J. B. Davies, D. W. Parke III, *et al.*, “Endophthalmitis after intravitreal injection of vascular endothelial growth factor inhibitors: Management and visual outcomes,” *Ophthalmology*, 2018.

[184] D. Trivedi, A. K. Denniston, and P. I. Murray, “Safety profile of anterior chamber paracentesis performed at the slit lamp,” *Clinical & Experimental Ophthalmology*, vol. 39, no. 8, pp. 725–728, 2011.

[185] B. V. Bui, B. Edmunds, G. A. Cioffi, and B. Fortune, "The gradient of retinal functional changes during acute intraocular pressure elevation," *Investigative ophthalmology & visual science*, vol. 46, no. 1, pp. 202–213, 2005.

[186] T. I. Tsai, B. V. Bui, and A. J. Vingrys, "Effect of acute intraocular pressure challenge on rat retinal and cortical function," *Investigative Ophthalmology & Visual Science*, vol. 55, no. 2, pp. 1067–1077, 2014.

[187] J. G. Crowston, Y. X. G. Kong, I. A. Trounce, T. M. Dang, E. T. Fahy, B. V. Bui, J. C. Morrison, and V. Chrysostomou, "An acute intraocular pressure challenge to assess retinal ganglion cell injury and recovery in the mouse," *Experimental Eye Research*, vol. 141, pp. 3–8, 2015.

[188] J. C. Morrison, W. O. Cepurna, S. Tehrani, T. E. Choe, H. Jayaram, D. C. Lozano, B. Fortune, and E. C. Johnson, "A period of controlled elevation of iop (cei) produces the specific gene expression responses and focal injury pattern of experimental rat glaucoma," *Investigative ophthalmology & visual science*, vol. 57, no. 15, pp. 6700–6711, 2016.

[189] J. A. Last, S. J. Liliensiek, P. F. Nealey, and C. J. Murphy, "Determining the mechanical properties of human corneal basement membranes with atomic force microscopy," *Journal of Structural Biology*, vol. 167, no. 1, pp. 19–24, 2009.

[190] K. S. Lim, S. S. Wickremasinghe, M. F. Cordeiro, C. Bunce, and P. T. Khaw, "Accuracy of intraocular pressure measurements in new zealand white rabbits," *Investigative Ophthalmology & Visual Science*, vol. 46, no. 7, pp. 2419–2423, 2005.

[191] M. Löbler, A. Rehmer, R. Guthoff, H. Martin, K. Sternberg, and O. Stachs, "Suitability and calibration of a rebound tonometer to measure iop in rabbit and pig eyes," *Veterinary Ophthalmology*, vol. 14, no. 1, pp. 66–68, 2011.

[192] P. Gunvant, R. D. Newcomb, E. M. Kirstein, V. E. Malinovsky, R. J. Madonna, and R. E. Meetz, "Measuring accurate iops: Does correction factor help or hurt?," *Clinical Ophthalmology (Auckland, NZ)*, vol. 4, p. 611, 2010.

[193] P. Gunvant, D. J. O'leary, M. Baskaran, D. C. Broadway, R. J. Watkins, and L. Vijaya, "Evaluation of tonometric correction factors," *Journal of Glaucoma*, vol. 14, no. 5, pp. 337–343, 2005.

[194] G. J. Orssengo and D. C. Pye, "Determination of the true intraocular pressure and modulus of elasticity of the human cornea in vivo," *Bulletin of Mathematical Biology*, vol. 61, no. 3, pp. 551–572, 1999.

[195] D. H. Chang and R. D. Stulting, "Change in intraocular pressure measurements after lasik: the effect of the refractive correction and the lamellar flap," *Ophthalmology*, vol. 112, no. 6, pp. 1009–1016, 2005.

[196] J. S. Hardin, C. I. Lee, L. F. Lane, C. C. Hester, and R. G. Morshedi, "Corneal hysteresis in post-radial keratotomy primary open-angle glaucoma," *Graefe's Archive for Clinical and Experimental Ophthalmology*, vol. 256, no. 10, pp. 1971–1976, 2018.

[197] P.-J. Shih, I.-J. Wang, W.-F. Cai, and J.-Y. Yen, "Biomechanical simulation of stress concentration and intraocular pressure in corneas subjected to myopic refractive surgical procedures," *Scientific Reports*, vol. 7, no. 1, p. 13906, 2017.

[198] A. K. Jain, J. S. Saini, R. Gupta, *et al.*, "Tonometry in normal and scarred corneas, and in postkeratoplasty eyes: A comparative study of the goldmann, the proton and the schiotz tonometers.," *Indian Journal of Ophthalmology*, vol. 48, no. 1, p. 25, 2000.

[199] J. L. Hernández-Verdejo, M. A. Teus, and G. Bolivar, "Simultaneous measurement of intraocular pressure in the anterior chamber and the vitreous cavity," *Acta Ophthalmologica*, vol. 88, no. 7, pp. e265–e268, 2010.

[200] P. A. Netland, H. Terada, and C. H. Dohlman, "Glaucoma associated with keratoprosthesis1," *Ophthalmology*, vol. 105, no. 4, pp. 751–757, 1998.

[201] R. Lee, Z. Khoueir, E. Tsikata, J. Chodosh, C. H. Dohlman, and T. C. Chen, "Long-term visual outcomes and complications of boston keratoprosthesis type ii implantation," *Ophthalmology*, vol. 124, no. 1, pp. 27–35, 2017.

[202] A. Gibbons, E. H. Leung, L. J. Haddock, C. A. Medina, V. Fernandez, J.-M. A. Parel, H. A. Durkee, G. Amescua, E. C. Alfonso, and V. L. Perez, "Long-term outcomes of the aphakic snap-on boston type i keratoprosthesis at the bascom palmer eye institute," *Clinical Ophthalmology (Auckland, NZ)*, vol. 12, p. 331, 2018.

[203] P. Enders, J. Hall, M. Bornhauser, K. Mansouri, L. Altay, S. Schrader, T. S. Dietlein, B. O. Bachmann, T. Neuhann, and C. Cursiefen, "Telemetric intraocular pressure monitoring after boston keratoprosthesis surgery.," *Ophthalmology*, vol. 126, no. 2, p. 322, 2019.

[204] J. O. Lee, H. Park, J. Du, A. Balakrishna, O. Chen, D. Sretavan, and H. Choo, "A microscale optical implant for continuous in vivo monitoring of intraocular pressure," *Microsystems & Nanoengineering*, vol. 3, p. 17057, 2017.

[205] J. J. Kang, N. Allemann, J. De La Cruz, and M. S. Cortina, "Serial analysis of anterior chamber depth and angle status using anterior segment optical coherence tomography after boston keratoprosthesis," *Cornea*, vol. 32, no. 10, pp. 1369–1374, 2013.

[206] J. C. Downs, C. F. Burgoyne, W. P. Seigfreid, J. F. Reynaud, N. G. Strouthidis, and V. Sallee, "24-hour iop telemetry in the nonhuman primate: implant system performance and initial characterization of iop at multiple timescales," *Investigative ophthalmology & visual science*, vol. 52, no. 10, pp. 7365–7375, 2011.

[207] L. Yu, B. Kim, and E. Meng, “Chronically implanted pressure sensors: challenges and state of the field,” *Sensors*, vol. 14, no. 11, pp. 20620–20644, 2014.

[208] P. F. Duggan, “Time to abolish gold standard,” *BMJ: British Medical Journal*, vol. 304, no. 6841, p. 1568, 1992.

[209] D. S. Jones and S. H. Podolsky, “The history and fate of the gold standard,” *The Lancet*, vol. 385, no. 9977, pp. 1502–1503, 2015.

[210] J. A. Peterson, J. A. Kiland, M. A. Croft, and P. L. Kaufman, “Intraocular pressure measurement in cynomolgus monkeys. tono-pen versus manometry.,” *Investigative ophthalmology & visual science*, vol. 37, no. 6, pp. 1197–1199, 1996.

[211] C. A. Morris, J. G. Crowston, J. D. Lindsey, J. Danias, and R. N. Weinreb, “Comparison of invasive and non-invasive tonometry in the mouse,” *Experimental Eye Research*, vol. 82, no. 6, pp. 1094–1099, 2006.

[212] S. Ong, Y. Tan, P. Chia, and S. E. Air, “Personal protective equipment contamination by severe acute respiratory syndrome coronavirus 2 (SARS-CoV-2) from a symptomatic patient,” *Journal of the American Medical Association*, vol. 4, 2020.

[213] J. A. Lednicky, M. Lauzardo, Z. H. Fan, A. S. Jutla, T. B. Tilly, M. Gangwar, M. Usmani, S. N. Shankar, K. Mohamed, A. Eiguren-Fernandez, C. J. Stephenson, M. M. Alam, M. A. Elbadry, J. C. Loeb, K. Subramaniam, T. B. Waltzek, K. Cherabuddi, J. G. Morris, and C.-Y. Wu, “Viable sars-cov-2 in the air of a hospital room with covid-19 patients,” *medRxiv*, 2020.

[214] N. van Doremalen, T. Bushmaker, D. H. Morris, M. G. Holbrook, A. Gamble, B. N. Williamson, A. Tamin, J. L. Harcourt, N. J. Thornburg, S. I. Gerber, *et al.*, “Aerosol and surface stability of SARS-CoV-2 as compared with SARS-CoV-1,” *New England Journal of Medicine*, 2020.

[215] J. Raboud, A. Shigayeva, A. McGeer, E. Bontovics, M. Chapman, D. Gravel, B. Henry, S. Lapinsky, M. Loeb, L. C. McDonald, *et al.*, “Risk factors for SARS transmission from patients requiring intubation: a multicentre investigation in toronto, canada,” *PLoS One*, vol. 5, no. 5, 2010.

[216] R. A. Fowler, C. B. Guest, S. E. Lapinsky, W. J. Sibbald, M. Louie, P. Tang, A. E. Simor, and T. E. Stewart, “Transmission of severe acute respiratory syndrome during intubation and mechanical ventilation,” *American Journal of Respiratory and Critical Care Medicine*, vol. 169, no. 11, pp. 1198–1202, 2004.

[217] K. Tran, K. Cimon, M. Severn, C. L. Pessoa-Silva, and J. Conly, “Aerosol generating procedures and risk of transmission of acute respiratory infections to healthcare workers: a systematic review,” *PloS One*, vol. 7, no. 4, 2012.

[218] J.-P. Frat, A. W. Thille, A. Mercat, C. Girault, S. Ragot, S. Perbet, G. Prat, T. Boulain, E. Morawiec, A. Cottereau, *et al.*, "High-flow oxygen through nasal cannula in acute hypoxemic respiratory failure," *New England Journal of Medicine*, vol. 372, no. 23, pp. 2185–2196, 2015.

[219] Y.-N. Ni, J. Luo, H. Yu, D. Liu, B.-M. Liang, and Z.-A. Liang, "The effect of high-flow nasal cannula in reducing the mortality and the rate of endotracheal intubation when used before mechanical ventilation compared with conventional oxygen therapy and noninvasive positive pressure ventilation. a systematic review and meta-analysis," *The American Journal of Emergency Medicine*, vol. 36, no. 2, pp. 226–233, 2018.

[220] M. Dres and A. Demoule, "What every intensivist should know about using high-flow nasal oxygen for critically ill patients," *Revista Brasileira de Terapia Intensiva*, vol. 29, no. 4, p. 399, 2017.

[221] R. L. R. Bocchile, D. C. Cazati, K. T. Timenetsky, and A. S. Neto, "The effects of high-flow nasal cannula on intubation and re-intubation in critically ill patients: a systematic review, meta-analysis and trial sequential analysis," *Revista Brasileira de Terapia Intensiva*, vol. 30, no. 4, p. 487, 2018.

[222] S. Sanche, Y. Lin, C. Xu, E. Romero-Severson, N. Hengartner, and R. Ke, "High contagiousness and rapid spread of severe acute respiratory syndrome coronavirus 2.," *Emerging Infectious Diseases*, vol. 26, no. 7, 2020.

[223] J. C.-H. Cheung, L. T. Ho, J. V. Cheng, E. Y. K. Cham, and K. N. Lam, "Staff safety during emergency airway management for COVID-19 in hong kong," *The Lancet. Respiratory Medicine*, vol. 8, no. 4, p. e19, 2020.

[224] D. S. Hui, B. K. Chow, T. Lo, O. T. Tsang, F. W. Ko, S. S. Ng, T. Gin, and M. T. Chan, "Exhaled air dispersion during high-flow nasal cannula therapy versus CPAP via different masks," *European Respiratory Journal*, vol. 53, no. 4, p. 1802339, 2019.

[225] R. Canelli, C. W. Connor, M. Gonzalez, A. Nozari, and R. Ortega, "Barrier enclosure during endotracheal intubation," *New England Journal of Medicine*, 2020.

[226] A. M. Girgis, M. N. Aziz, T. C. Gopesh, J. Friend, A. M. Grant, J. A. Sandubrae, and D. A. Banks, "Novel coronavirus disease 2019 (covid-19) aerosolization box: Design modifications for patient safety," *Journal of Cardiothoracic and Vascular Anesthesia*, 2020.

[227] T. D. Fansler and S. E. Parrish, "Spray measurement technology: a review," *Measurement Science and Technology*, vol. 26, no. 1, p. 012002, 2014.

[228] N. F. P. Association *et al.*, "NFPA 99: Health care facilities code," *Quincy, MA: NFPA*, 2015.

[229] I. Telias and N. D. Ferguson, “Added benefit of noninvasive ventilation to high-flow nasal oxygen to prevent reintubation in higher-risk patients,” *Journal of the American Medical Association*, vol. 322, no. 15, pp. 1455–1457, 2019.

[230] D. Thurston and J. Carnahan, “Fuzzy ratings and utility analysis in preliminary design evaluation of multiple attributes,” *Journal of Mechanical Design*, vol. 114, pp. 648–658, 12 1992.

[231] R. Cappato, H. Calkins, S.-A. Chen, W. Davies, Y. Iesaka, J. Kalman, Y.-H. Kim, G. Klein, A. Natale, D. Packer, *et al.*, “Updated worldwide survey on the methods, efficacy, and safety of catheter ablation for human atrial fibrillation,” *Circulation: Arrhythmia and Electrophysiology*, vol. 3, no. 1, pp. 32–38, 2010.

[232] M. Padala, J. H. Jimenez, A. P. Yoganathan, A. Chin, and V. H. Thourani, “Transapical beating heart cardioscopy technique for off-pump visualization of heart valves,” *The Journal of thoracic and cardiovascular surgery*, vol. 144, no. 1, pp. 231–234, 2012.

[233] S. R. Atmakuri, E. I. Lev, C. Alviar, E. Ibarra, A. E. Raizner, S. L. Solomon, and N. S. Kleiman, “Initial experience with a magnetic navigation system for percutaneous coronary intervention in complex coronary artery lesions,” *Journal of the American College of Cardiology*, vol. 47, no. 3, pp. 515–521, 2006.

[234] S. Jeon, A. K. Hoshiar, K. Kim, S. Lee, E. Kim, S. Lee, J.-y. Kim, B. J. Nelson, H.-J. Cha, B.-J. Yi, *et al.*, “A magnetically controlled soft microrobot steering a guidewire in a three-dimensional phantom vascular network,” *Soft Robotics*, vol. 6, no. 1, pp. 54–68, 2019.

[235] D. E. Ost, A. Ernst, X. Lei, K. L. Kovitz, S. Benzaquen, J. Diaz-Mendoza, S. Greenhill, J. Toth, D. Feller-Kopman, J. Puchalski, *et al.*, “Diagnostic yield and complications of bronchoscopy for peripheral lung lesions. results of the aquire registry,” *American journal of respiratory and critical care medicine*, vol. 193, no. 1, pp. 68–77, 2016.

[236] A. C. Chen and C. T. Gillespie, “Robotic endoscopic airway challenge: Reach assessment,” *The Annals of thoracic surgery*, vol. 106, no. 1, pp. 293–297, 2018.

[237] S. I. Odronic, T. R. Gildea, and D. J. Chute, “Electromagnetic navigation bronchoscopy-guided fine needle aspiration for the diagnosis of lung lesions,” *Diagnostic cytopathology*, vol. 42, no. 12, pp. 1045–1050, 2014.